ASSOCIATIE EURATOM-FOM

FOM-INSTITUUT VOOR PLASMAFYSICA

RIJNHUIZEN – NIEUWEGEIN – NEDERLAND

RIJNHUIZEN REPORT 86-171

STUDY OF PROFILE CONTROL AND SUPRA-THERMAL ELECTRON PRODUCTION WITH ELECTRON CYCLOTRON WAVES

Article 14 Contract No. JJ5/9007

RR 86-171

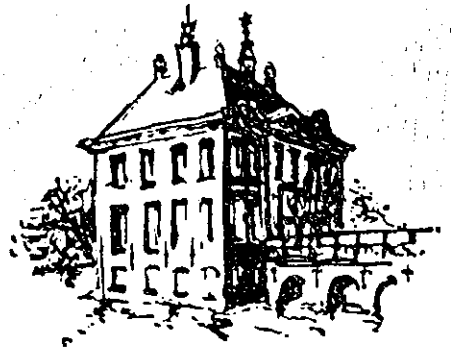

TABLE OF CONTENTS

I. Introduction

STUDY OF PROFILE CONTROL AND SUPRA-THERMAL ELECTRON PRODUCTION WITH ELECTRON CYCLOTRON WAVES

I. INTRODUCTION

The development of high frequency, high power wave sources in the past ten years has provided thermonuclear plasma physics with an important tool to deposit RF power in the electron component of a magnetized plasma. The first experimental results on electron cyclotron resonance heating (ECRH) were reported in 1976 (TM3). Since then, an increasing number of experiments were devoted to many aspects of ECRH. Reviews of the experimental results are given in Refs. [1-3]. Parallel to this experimental effort, a firm theoretical basis for EC wave propagation and absorption in inhomogeneous plasmas has been developed (see e.g. Refs. [3-5]). The bulk of this theory is based upon the validity of a WKB description.

Electron cyclotron waves propagate in two modes that are distinguished by their polarization. In the case of propagation perpendicular to the equilibrium magnetic field the ordinary (O-)mode is polarized with its electric field parallel to the equilibrium magnetic field, while the extraordinary (X-)mode is elliptically polarized with its electric field vector perpendicular to $\underline{B}$. In sufficiently hot and large plasmas, the power is absorbed in a single pass and the deposition is very localized, resulting in high power densities. The spatial position of this deposition is easily controlled by adjustment of either the toroidal magnetic field or the direction in which the power is injected.

Injection from the low-field side of the cold resonance ($\omega = n\omega_c$) in either the fundamental O-mode or the second harmonic X-mode, tend to deposit the RF energy in the low energy range of resonant particles and, thus, will primarily lead to bulk heating. In the case of injection from the high-field side of the cold resonance layer, the waves will first encounter the high energetic resonant particles and will tend to deposit the power in the tail of the electron distribution function. This method is suitable for current drive and supra-thermal generation objectives. Because of the smooth transition from propaga-

tion in free space to propagation inside the plasma, EC waves are insensitive to the edge conditions and the power can propagate to the plasma centre without effecting the boundary plasma. The localization and flexibility of the power deposition make ECRH suitable for specific physics goals like temperature and current profile tailoring, MHD mode stabilization, and measurement of local transport coefficients by heat pulse propagation.

Up to now the emphasis in ECRH applications to tokamaks has been on bulk heating. Energy confinement under conditions of strong additional heating has been studied in a number of devices, in particular in the large tokamaks Doublet III and T-10. The energy confinement time τ_E^{EC} in DIII divertor discharges was found to be independent of the density and to be proportional to the plasma current. This scaling is similar to the one found for neutral beam heated plasmas [6,7]. On the other hand, in T-10 the increment ΔW in stored energy was found to be independent of the current and to be linearly proportional to the density [8]. The energy confinement in T-10 is found to be better than Kaye-Goldston L-mode scaling and to agree with T-11 scaling. The latter scaling is also found for ECR-heated plasmas in TFR [9]. The differences between the experimental results indicate that general conclusions are difficult to draw.
In both D-III and T-10 it is found that ΔW and τ_E^{EC} do not change when, by changing the toroidal field, the resonance zone is moved outside the q=1 surface over the range $r/a \lesssim 0.5$. (However, the T-10 results seem to refer to peak values rather than to steady state conditions [10]). This implies that the energy confinement does not depend on the precise location of the heating zone. The same conclusion follows from D-III results at high densities where τ_E^{EC} remains constant although the deposition profile becomes broad due to increased wave diffraction. These results would support the idea that the gross energy confinement time is alike for all heating methods and does not depend on their details as long as the power is deposited within the q = 2 surface.

Effects on sawtooth oscillations have been observed in a number of experiments. In T-10, sawteeth have been stabilized by ECR-heating outside the q=1 surface [11]. In TFR no effect has been observed for heating either outside or inside the q=1 surface [9]. Instead, heating on the q=1 surface shows a decrease in the growth of the m=1 mode.

With full power a saturated state of the m=1 mode could be reached. Stabilization of the m=2 tearing mode has also been demonstrated in both experiments. In T-10 this stabilization depends on the resonance position; the stabilizing effect being largest for heating just outside the q=2 surface as expected for local temperature profile modifications.

The interaction of EC power with highly energetic electrons has been studied in PLT by top launch of the X-mode at down shifted frequencies [12]. Complete single pass absorption could be obtained in discharges with relatively low density. The production of supra-thermal particles is a sensitive function of the magnetic field: at low field strengths bulk heating occurs and at high field the absorption decreases because too few resonant particles are present. In the experiments the DC electric field played a fundamental role by accelerating the high electrons, created by the EC power, to very high energies.

The combination of Lower Hybrid Current Drive and EC power has been studied with injection of unpolarized waves in two relatively small machines [13,14]. In both VERSATOR and WT-2 the injection of EC power stabilizes the relaxation oscillations observed on the LH driven current leading to an increase in the LH driven current. These oscillations are ascribed to the Parail-Pogutse instability which occurs when the distribution function becomes highly anisotropic ($T_\perp << T_\parallel$). The effect of the EC power is to increase $T_\perp$ and thus to stabilize the instability. On WT-2 the injection of EC power has also been studied for Lower Hybrid current sustained plasmas [15]. The Lower Hybrid current drive efficiency improves when the resonance is on the low-field side. When the resonance is on the high-field side instead, the driven current decreases. Analogous results are obtained in the JFT-2M with the combination LHCD and second harmonic X-mode EC power [16].

One of the objectives of EC power injection into JET would be the stabilization of sawtooth oscillations either by the creation of supra-thermal electrons or by driving a non-inductive current. Stabilization of sawteeth has been accomplished in several LH experiments. These experiments show that the amount of non-inductive current required for stabilization is 30-50% of the total current. In ASDEX [17], q(o) is raised from just below to just above one, when the sawteeth disappear. No stabilization is found when the LH power is

applied in the heating mode, even though this yields a larger amount of supra-thermal electrons than in the case of the current driven mode.
In PLT [18] and PETULA [19] a regime has been observed where sawteeth are no longer present but still a stable m=1, n=1 oscillation occurs. Thus the effect of a supra-thermal population on mode stabilization is as yet unclear.

In this report, current drive and supra-thermal generation in JET plasmas is discussed. The specific form of EC power injection from the high-field side into JET that we consider, is launching through a top-port (or bottom-port). Top launch leads to long trajectories of the injected rays in regions where resonance with highly energetic particles occurs. Although the local power absorption may be quite small, these extended lengths can result in total absorption of the wave power. This optimizes power deposition in the far tail of the distribution function. The cold resonance may be at the edge of the plasma or even outside the vacuum vessel. For JET this means that existing wave sources at 60 or 70 GHz may be used.

The physics aspects of EC current drive and supra-thermal generation in JET are treated in Parts II and III. The transmission lines for power transfer from the gyrotrons to the vacuum vessel are discussed in Part IV. In Part V the possibility of optical transmission is investigated. Finally, in Part VI the technical aspects (power supply, control, data acquisition etc.) are discussed for a system of 12 gyrotrons (200 kW, 70 GHz, 10 ms). A layout is given and cost estimates are presented.

This work was performed as part of the research programme of the association agreement of Euratom and the "Stichting voor Fundamenteel Onderzoek der Materie" (FOM) with financial support from the "Nederlandse Organisatie voor Zuiver-Wetenschappelijk Onderzoek" (ZWO) and Euratom.

REFERENCES

[1] R. Prater et al., Course and Workshop on Applications of RF Waves to Tokamak Plasmas, Varenna, 1985, Int. School of Plasma Phys., to be published (Milano).

[2 A.C. Riviere, Plasma Phys. and Contr. Fusion 28 (1986) 1263.

[3] M. Bornatici et al., Nucl. Fusion 23 (1983) 1153.

[4] M. Bornatici, U. Ruffina, E. Westerhof, Comments on Plasma Phys. and Contr. Fusion IX (1985) 63.

[5] I. Fidone, G. Granata, R.L. Meyer, Phys. Fluids 25 (1982) 2249.

[6] K.H. Burell et al., Plasma Phys. and Contr. Nucl. Fus. Res. (IAEA, London, 1985), Proc. in Vol. I, Nucl. Fusion Suppl. 1985, p. 131.

[7] S. Ejima et al., 12th Eur. Conf. on Contr. Fus. and Plasma Physics (Budapest, 1985), Vol. II, p. 40.

[8] V.V. Alikaev et al., Plasma Phys. and Contr. Nuc. Fus. Res. (IAEA, London, 1985), Proc. in Vol. I, Nucl. Fusion Suppl. 1985, p. 419.

[9] TFR Group and FOM ECRH Team, 13th Eur. Conf. on Contr. Fus. and Plasma Heating (Schliersee, 1986), Vol. II, p. 207.

[10] B.B. Kadomtsev, Plasma Phys. and Contr. Fusion 28 (1986) 125.

[11] R.M.J. Sillen et al., Nucl. Fusion 26 (1986) 303.

[12] E. Mazzucato et al., PPPL-2328 (1986).

[13] M. Porkolab et al., Plasma Phys. and Contr. Nucl. Fus. Res. (IAEA, Baltimore, 1983), Proc. in Vol. I, Nucl. Fus. Suppl. 1983, p. 227.

[14] T. Maekawa et al., Nucl. Fusion 23 (1983) 242.

[15] A. Ando et al., Nucl. Fusion 26 (1986) 107.

[16] K. Hoshino et al., 12th Eur. Conf. on Contr. Fus. and Plasma Physics (Budapest, 1985) Vol. II, p. 184.

[17] F.X. Söldner et al., JET Article 14 Contract JJ5/9009 and references cited therein.

[18] C. Gormezano et al., JET Article 14 Contract JJ5/9008 and references cited therein.

[19] T.K. Chu et al., Nucl. Fusion 26 (1986) 666.

II. ELectron Cyclotron Current Drive and Supra-Thermal Generation in JET, I.R. 86/021.

FOM-Instituut voor
Plasmafysica
Rijnhuizen
Nieuwegein

I.R. 86/021

ELECTRON CYCLOTRON CURRENT DRIVE AND SUPRA-THERMAL GENERATION IN JET

R.W. Polman, T.J. Schep, E. Westerhof, L. Klieb*

Association Euratom-FOM, FOM-Instituut voor Plasmafysica
"Rijnhuizen" Nieuwegein, The Netherlands

ABSTRACT

Top launch of electron cyclotron (EC) wave energy into the JET device is considered with the aim to investigate the possibility of a spatially localized power deposition in the far tail of the electron distribution function. Such an injection scheme is favourable from the point of view of current drive and generation of a supra-thermal electron population. Oblique injection of the extra-ordinary mode at a wave frequency around 70 GHz is most suitable to this purpose.
A ray tracing code has been used to calculate the power deposition along rays that are injected under a variety of angles from several radial positions into D-shaped JET equilibria. Medium (n_o = $5 \cdot 10^{19}$ m^{-3}) and high (n_o = 10^{20} m^{-3}) density plasmas with central temperatures of 5 and 10 keV are investigated. The power deposition profile, the current drive efficiency, and the generation of supra-thermal electrons are discussed.

1. INTRODUCTION

Recent experiments with strong additional heating on the large tokamaks JET [1] and TFTR [2] are characterized by the following major features.

1. In the confinement zone, where a large pressure gradient is maintained, the radial profile and the volume averaged value of the electron temperature are almost independent of the level and the localization of the heating power. This phenomenon is known as "profile consistency" [3]. The related degradation of confinement is observed under ICRF [1] as well as NBI [2] heating conditions.
   The global confinement time τ_E can be represented as

*) present address: Hoogovens, Afd. TD BCD 42E 2 F 13, IJmuiden, The Netherlands.

$$\tau_E = (c + d/P)\ f\ (I_p) \qquad (1)$$

where P is the total heating power and I_p the plasma current.

2. The ratio of the volume averaged to central electron temperature is inversely proportional to the value of the safety factor at the limiter, i.e. $\langle T \rangle / T_o$ (:) q_a^{-1} [2].

3. In the core of the plasma, giant sawtooth oscillations develop which limit the central temperature. The boundary of this region is believed to be the q=1 surface and is approximately determined by the safety factor at the limiter, $r_{q=1}$ (:) a/q_a [2]. During the rise time of a sawtooth, the confinement of the core is much better than the global confinement. Although the core plays a limited role in the overall energy balance (it is the more important the less q_a is), the central temperature that can be reached is essential to future ignition experiments.

These experimental results give evidence to the existence of a strong correlation between the current and temperature profiles in tokamak discharges. The decoupling of these profiles could clear the way to increase the energy content of the plasma and to improve its confinement. The extent to which this decoupling has to be achieved is, as yet, unknown. In Ref. 4 it is suggested that, although there is an intrinsic difference between the transient phase and the steady state, only a modest change in the current distribution occurs between the non-sawteething regime just after current ramp-up and the regime where sawteeth oscillations occur.

The decoupling of current and temperature could be accomplished by driving part of the current non-inductively or by carrying the current by a supra-thermal electron population which is collisionally decoupled from the bulk of the plasma. In this context it should be noted that current drive, supra-thermal generation, and bulk heating are intrinsically related and not easily separable.

The required amount of non-inductive current can be provided by neutral beam injection and by various RF methods. The spatial distribution of this current, however, might well be the important factor which determines eventually the efficiency in terms of plasma energy content and confinement time, of the non-inductive current generation. Recently, it has been conjectured [5] that, in tokamak plasmas, some

mechanism exists that enforces the current profile to be stable against resistive kink modes. The stability against tearing modes with all mode numbers imposes fairly narrow constraints on the shape of the current profile. This would imply that the shape of the non-inductive current should be such that the profile of the total current remains consistent with Δ'-stability.
The favourable feature of electron cyclotron power deposition and current drive is its localized character. This could provide the means for this necessary tailoring of the current profile, even with modest EC-driven currents.

In this paper, current drive and generation of supra-thermal electrons by electron cyclotron waves are discussed for JET plasmas. The construction of JET limits the injection of EC power to either a top-port or a horizontal port at the low-field side, thus imposing strong restrictions on the possible injection positions. However, top launch seems to be most favourable in view of supra-thermal generation, current drive, and current profile tailoring potentialities. Injection of EC waves in either the ordinary mode or in the second harmonic extraordinary mode, from the low-field side when the resonance is inside the plasma, will give an excellent localization of the power deposition. Although this method is suitable for heating purposes or for m=2 mode stabilization, it is less so for current drive and supra-thermal generation.
The RF power is injected in the extraordinary mode with a frequency below the local cyclotron frequency so that the absorption occurs via the tail of the electron distribution function [6]. A practical advantage of this down-shifted frequency is that existing wave sources of 70 GHz can be used in JET at B_T = 34 KG. The second harmonic extraordinary mode at 140 GHz is less favourable than the fundamental mode since it has a lower cut-off density. Therefore, the centre of the plasma is less accessible for this mode and the localization of the power deposition is degraded.
In the next Section, some concepts related with the propagation and absorption of electron cyclotron wave power are discussed. The emphasis is on those elements that are needed for the interpretation of the ray tracing calculations. In Section 3, the ray tracing code TORAY is briefly presented, and the data are given of the D-shaped JET equilibria that are investigated. The results of the numerical calcula-

tions are presented in Sect. 4. The localization of the power deposition in real and momentum space, and its parametric dependence on density and temperature are investigated. The efficiency of non-inductive current drive by EC power deposition is addressed in Section 5. In Section 6, the conditions for the onset of the generation of suprathermal electrons, and the power level at which runaway will occur are discussed. Finally, the conclusions are presented in Section 7.

2. ELECTRON CYCLOTRON RESONANCE

The relativistic electron cyclotron resonance condition is

$$\gamma - \frac{\omega_c}{\omega} - N_{\parallel} \, p_{\parallel}/mc = 0, \tag{2a}$$

where

$$\gamma = [1 + p_{\perp}^2/m^2c^2 + p_{\parallel}^2/m^2c^2]^{1/2} \tag{2b}$$

is the relativistic mass factor, $p_{\perp,\parallel}$ are the components of the relativistic momentum perpendicular and parallel to the equilibrium magnetic field, respectively, m is the rest mass, ω_c the local cyclotron frequency, ω the wave frequency, and $N_{\parallel}$ is the parallel refractive index.

For fixed $p_{\perp}/mc$, the curves $\gamma^2 - p_{\parallel}^2/m^2c^2 = 1 + p_{\perp}^2/m^2c^2$ form a set of hyperbolas all having the same asymptote for $p_{\parallel} \to \infty$. The curve for $p_{\perp} = 0$ has been represented in Fig. 1. The resonance condition is represented by the straight line section $\gamma - 1 = \Delta + N_{\parallel} p_{\parallel}/mc$, where $\Delta = \omega_c/\omega - 1$, inside the hyperbola $p_{\perp} = 0$. The angle between the straight line and the $p_{\parallel}$-axis is determined by $N_{\parallel}$. The ranges of energies $E = mc^2(\gamma - 1)$ and parallel momenta of the resonant particles are determined by the intersection points with the curve $p_{\perp} = 0$,

$$\frac{E^{\pm}}{mc^2} = \frac{1}{1 - N_{\parallel}^2} \left[\frac{\omega_c}{\omega} - 1 + N_{\parallel}^2 \right] \pm \frac{|N_{\parallel}|}{1 - N_{\parallel}^2} \left(\frac{\omega_c^2}{\omega^2} - 1 + N_{\parallel}^2 \right)^{1/2}, \tag{3a}$$

and

$$\frac{p_{\parallel}^{\pm}}{mc} = \frac{N_{\parallel} \, \omega_c/\omega}{1 - N_{\parallel}^2} \pm \frac{\operatorname{sgn} N_{\parallel}}{1 - N_{\parallel}^2} \left[\frac{\omega_c^2}{\omega^2} - 1 + N_{\parallel}^2 \right]^{1/2}. \tag{3b}$$

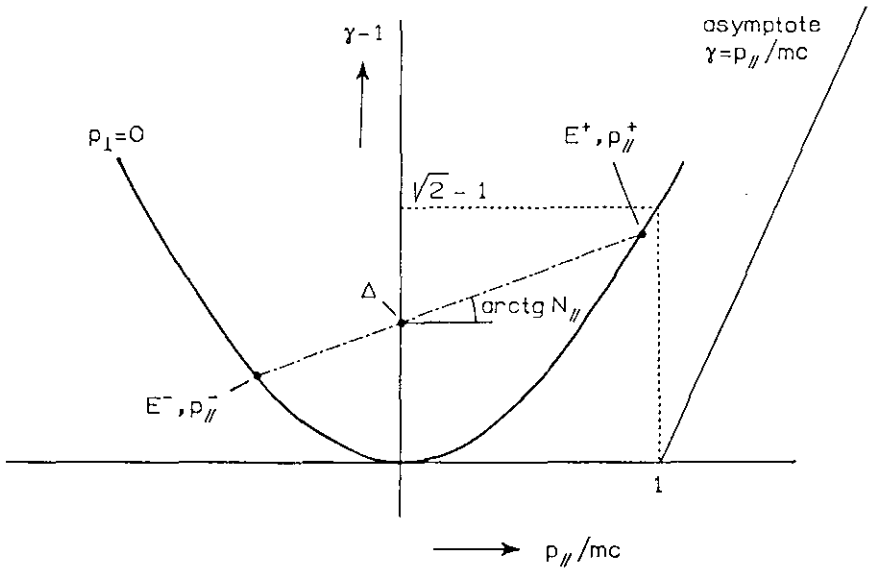

Fig. 1. The relativistic resonance condition (2) is satisfied on the straight line, $\gamma - 1 = \Delta + N_{\|}\ p_{\|}/m$, where $\Delta = \omega_c/\omega - 1$, within the hyperbola $p_{\perp} = 0$.

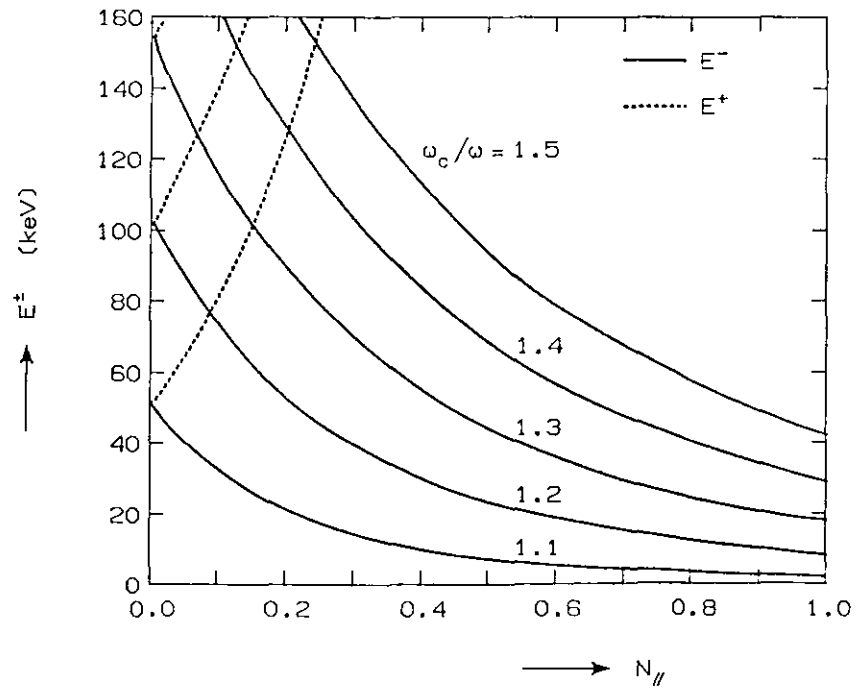

Fig. 2. The maximum and minimum resonant energies $E^{\pm}$ as a function of the parallel index of refraction $N_{\|}$.

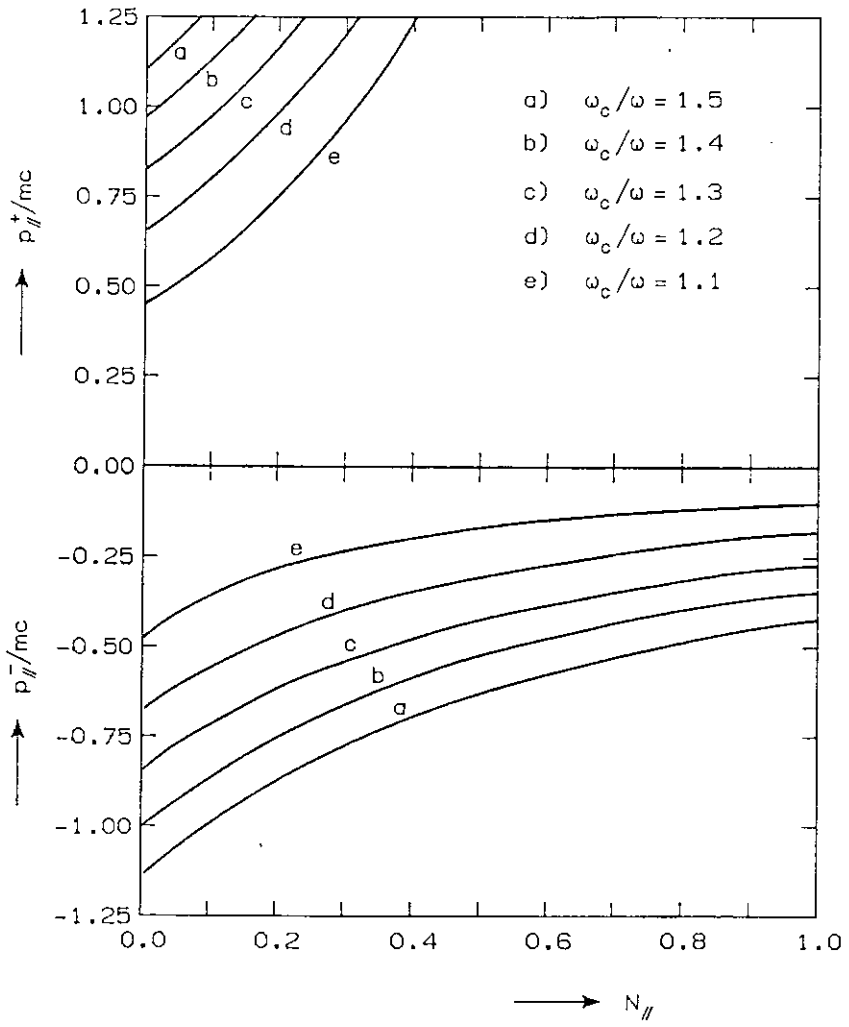

Fig. 3. The maximum, and minimum values $p_{||}^{\pm}$ of the resonant parallel momentum as a function of $N_{||}$.

In Figs. 2 and 3, E^{+}_{-} and $p^{+}_{\top}$ are plotted as functions of $N_{||}$ with ω_c/ω as a parameter. These figures show that the resonance condition implies that electrons with rather large energies can be resonant if waves with down-shifted frequencies ($\omega < \omega_c$) are injected [7, 8]. Under the realistic assumption that the electron distribution function is a decreasing function of energy, most of the RF energy will be deposited near the lower limit of the energy range. It is clear that large values of ω_c/ω and small values of $N_{||}$ are favourable from the point of view of current drive and supra-thermal generation.

For current drive, however, $N_{\|}$ should not be too small in order to retain an asymmetrical deposition of energy. On the other hand, the power deposition decreases with increasing values of ω_c/ω, because, in general, fewer and fewer particles will be resonant.

The smallness of the wavelength as compared with the characteristic scale lengths of the medium, allows for a quasi-optical description of the propagation of electron cyclotron wave energy in an inhomogeneous tokamak plasma.

In the range of plasma temperatures under consideration, the propagation of the extraordinary mode and, thus, the wave trajectories may be calculated from the cold plasma dispersion relation [9]

$$N_{\perp}^2 = 1 - N_{\|}^2 - \frac{\omega_p^2}{\omega^2} - \frac{1}{2}\frac{\omega_p^2\omega_c^2/\omega^4}{1 - \omega_p^2/\omega^2 - \omega_c^2/\omega^2}\left\{\left[(1 - N_{\|}^2)^2 + 4N_{\|}^2\,\frac{\omega^2}{\omega_c^2}\left(1 - \frac{\omega_p^2}{\omega^2}\right)\right]^{1/2} + (1 + N_{\|}^2)\right\}, \qquad (4)$$

where ω_p is the plasma frequency.

When the wave energy is launched from the high-field side of the device, the frequency must be in the range $\omega_- < \omega < \omega_{UH}$, where ω_{UH} is the upper hybrid frequency and ω_- is the high density cutoff

$$\omega_- = -\frac{1}{2}\omega_c + \frac{1}{2}\omega_c\left[1 + 4\,\frac{\omega_p^2/\omega_c^2}{1 - N_{\|}^2}\right]^{1/2}. \qquad (5)$$

For relativly large values of ω_p^2/ω_c^2 and $N_{\|}^2$ the energy cannot penetrate into the centre of the plasma due to strong diffraction effects. For example, at $B_T = 3.4$ T we have $\omega_p^2/\omega_c^2 = 0.9\ n_{20}$ (density in 10^{20} m^{-3}) yielding $f_- \approx 60$ GHz for $n_{20} = 1$ en $N_{\|}^2 = 0.1$. Hence, at this high density, 60 GHz waves cannot reach the centre of JET. The corresponding cut-off density for 70 GHz waves is $n_{20} \approx 1.3$.

Along the rays calculated from (4), the power deposition is calculated employing the relativistic expressions for the dielectric tensor [10,11]. The relative power in the ray is

$$P_r(s) = \exp -\int_0^s \alpha\, ds' \qquad (6)$$

so that the power absorbed by the plasma is $P_{p\ell} = P_0(1 - P_r)$, where the integral is along the ray and α is the absorption coefficient

$$\alpha = \frac{\underline{E}^{*} \cdot \underline{\underline{\varepsilon}}_a \cdot \underline{E}}{|\underline{S}|} \quad . \tag{7}$$

Here, $\underline{E}$ is the wave electric field, the star denotes the complex conjugate and $\underline{S}$ is the Poynting flux. The small flux of sloshing energy has been neglected. The anti-hermitian part $\underline{\underline{\varepsilon}}_a$ of the dielectric tensor and the polarization of the wave are calculated with the full relativistic cyclotron resonance condition.

The dielectric tensor contains a contribution arising from the Maxwellian bulk electrons and a contribution due to a supra-thermal electron population. The supra-thermal population has been modelled by a low density, high energy distribution function which is Maxwellian in a frame moving along the equilibrium magnetic field [12].

The wave polarization and the absorption coefficient are plotted in Fig. 4 as a function of ω_c/ω. Curves for $N_{\parallel} = 0.3$, 0.4 and 0.5 and for $\omega_p^2/\omega^2 = 0.5$, 1 are shown. The temperature of the bulk electrons is taken to be 5 keV.

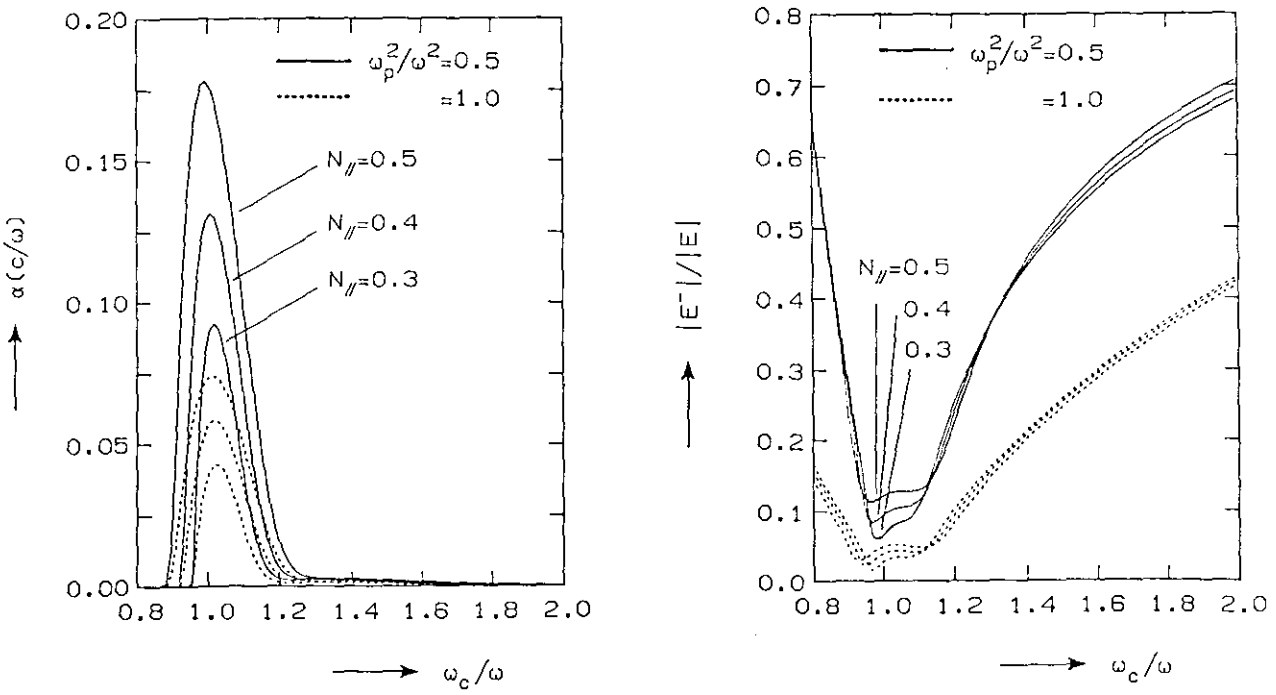

Fig. 4. The absorption coefficient (a) and the right-handed component of the wave polarization (b) as a function of ω_c/ω for $N_{\parallel} = 0.3$, 0.4, 0.5, and for central densities $n_o = 0.5$ and $1.0 \cdot 10^{20}$ m^{-3}. The electron temperature is 5 keV. A suprathermal population is simulated by a Maxwellian distribution with $n_s = 10^{-2}\, n_o$ and $T_s = 50$ keV.

The figure shows that the absorption coefficient falls rather sharply for larger values of ω_c/ω. Further, it increases with $N_{\parallel}$ and decreases with density. The latter effect is due to the tendency of the extra-ordinary mode to acquire the wrong polarization with respect to the orbital motion of the electrons. The tails of the absorption curves arise from a small Maxwellian population of the supra-thermal electrons with density $n_s = 10^{-2}\, n_o$ and temperature $T_s = 50$ keV. Although these tails are very small, they can have a rather large effect on the power deposition as pointed out in the next Section.

3. RAY TRACING IN D-SHAPED JET EQUILIBRIA

The pattern of the ray trajectories and the power absorption of electron cyclotron waves injected from a top-port into the JET device are investigated numerically with the ray tracing code TORAY [13]. This code, which is based on the code RAYS [14], is tailored to study EC heating and current drive in toroidal geometry. It solves the Hamiltonian form of the geometrical optics equations and contains a full graphics package for displaying the behaviour of the rays.
The ray trajectories are calculated from the cold dispersion relation (4), and the power deposition along the ray is obtained with the aid of the relativistic absorption coefficient (7). The code has been adapted to calculate ray paths in D-shaped JET equilibria, and to determine the power deposition along a ray in the case of a Maxwellian plasma containing a small population of supra-thermal electrons.

The JET equilibrium configuration has been modelled as follows. The poloidal cross-section of a D-shaped magnetic surface is given by the distance $r(\bar{\psi},\nu)$ with respect to the magnetic axis [15],

$$r(\bar{\psi},\nu) = \sum_{k,i} b_{ik}\, \bar{\psi}^{k} \cos(i-1)\,\nu\,, \quad k=1\ldots N, \quad i=1\ldots M, \qquad (8)$$

where $\bar{\psi}^2 = (\psi - \psi_o)/|\psi_L - \psi_o|$, ψ being the poloidal flux function and $\psi_{L,o}$ its value at the limiter and on the magnetic axis, respectively, and ν is the angle with respect to the major radius R. The magnetic axis is shifted by r_s with respect to the geometrical centre. The free parameters b_{ik} are given by JET equilibrium codes and determine, together with r_s, the poloidal field structure of a particular discharge.
The toroidal magnetic field is

$$B_T = B_{oT} \frac{R_o}{R} D(\bar{\psi}), \tag{9}$$

where B_{oT} is the vacuum field on the magnetic axis and the function $D(\bar{\psi})$ is a measure for diamagnetic effects:

$$D(\bar{\psi}) = \left\{ \left[\frac{F^2_{max}}{(R_o B_{To})^2} - 1 \right] \left(1 - \bar{\psi}^2\right)^{Q+1} + 1 \right\}^{\frac{1}{2}}. \tag{10}$$

F^2_{max} and the value of the peaking factor Q are additional input parameters provided by JET codes.

The electron density and temperature profiles are given as functions of $\bar{\psi}$

$$\begin{aligned} n_e(\bar{\psi}) &= (n_o - n_L)\left[1 - (a_n \bar{\psi})^{b_n} \right]^{c_n} + n_L, \\ T_e(\bar{\psi}) &= (T_o - T_L)\left[1 - (a_T \bar{\psi})^{b_T} \right]^{c_T} + T_L, \end{aligned} \tag{11}$$

where $n_{o,L}$ and $T_{o,L}$ are the density and temperature at the magnetic axis and at the limiter, respectively.

In the ray tracing calculations to be presented in the next Section, various magnetic configurations that correspond to JET discharges are investigated. In these configurations the density and temperature profiles are chosen freely. The parameters which describe these equilibria are listed in Table 1.

The first column does not represent a particular JET discharge but is a case in which the plasma fills almost completely the available space in the vacuum vessel. The peaking factor Q, F^2_{max}, and the density and temperature profiles are chosen freely. The parameters given in column IIa correspond to discharge 3901. Column IIb applies to the same magnetic equilibrium but with parabolic profiles and freely chosen peak values of density and temperature. Column IIIa corresponds to the low-q discharge 7774, rescaled to a toroidal field of 3.43 T on the geometrical axis. In contrast to the preceding case, this equilibrium is paramagnetic. For comparison with cases I and IIb, this equilibrium is also investigated with parabolic profiles of density and temperature (column IIIb).

The numerical results to be presented are obtained for waves with frequencies of 60 and 70 GHz, launched from 3 positions of the top-port:

	I	IIa	IIb	IIIa	IIIb
r_s	0.14 m	0.16 m		0.16 m	
B_{oT}	3.25 T	3.25 T		3.25 T	
Q	0.0	1.5		0.91	
Q_{axis}		1.07		0.81	
Q_{wall}		5.14		2.15	
ellipticity		1.47		1.42	
$F^2_{max}/R^2_o B^2_{oT}$	0.88	0.803		1.215	
a_n	1	1	1	1	1
b_n	2	2	2	2	2
c_n	1	0.95	1	0.33	1
n_o	0.5, $1.0\cdot10^{20}$ m^{-3}	0.5, $1.0\cdot10^{20}$ m^{-3}	0.5, $1.0\cdot10^{20}$ m^{-3}	0.8, $1.0\cdot10^{20}$ m^{-3}	$0.5\cdot10^{20}$ m^{-3}
n_L	10^{18} m^{-3}	10^{17} m^{-3}	10^{18} m^{-3}	10^{17} m^{-3}	10^{18} m^{-3}
a_T	1	0.99	1	0.99	1
b_T	2	4.2	2	4.6	2
c_T	1	2.2	1	1.0	1
T_o	5, 10 keV	5.28 keV	5, 10 keV	3.8 keV	5, 10 keV
T_L	50 eV	30 eV	50 eV	30 eV	50 eV

Table 1. Parameters of the equilibria used in the ray tracing calculations.

the high-field side (R = 2.65 m), the centre (R = 3.0 m) and the low-field side (R = 3.35 m). For 70 GHz and B_T = 3.4 T at R = 2.96 m, the cold resonance layer is at R $\simeq$ 4.0 m, which is in the very outside layers of the plasma.

The direction of the injected rays is specified by the angles ϕ and θ, which are the spherical coordinate angles with respect to a local Cartesian system (x,y,z) at the launching position. The z-axis of this system is parallel to the (vertical) axis of symmetry, x is in the direction of the major radius and the y-axis runs in the toroidal direction (see Fig. 5). Hence, θ is the angle between the ray and the vertical direction, and ϕ is the angle between the projection of the ray on the equatorial plane and the major radius.

In the majority of cases to be presented in the next Section, the injection angles are in the range $135^0 \leq \theta \leq 175^0$ and $60^0 \leq -\phi \leq 100^0$.

The cold dispersion relation (4), which determines the ray paths,

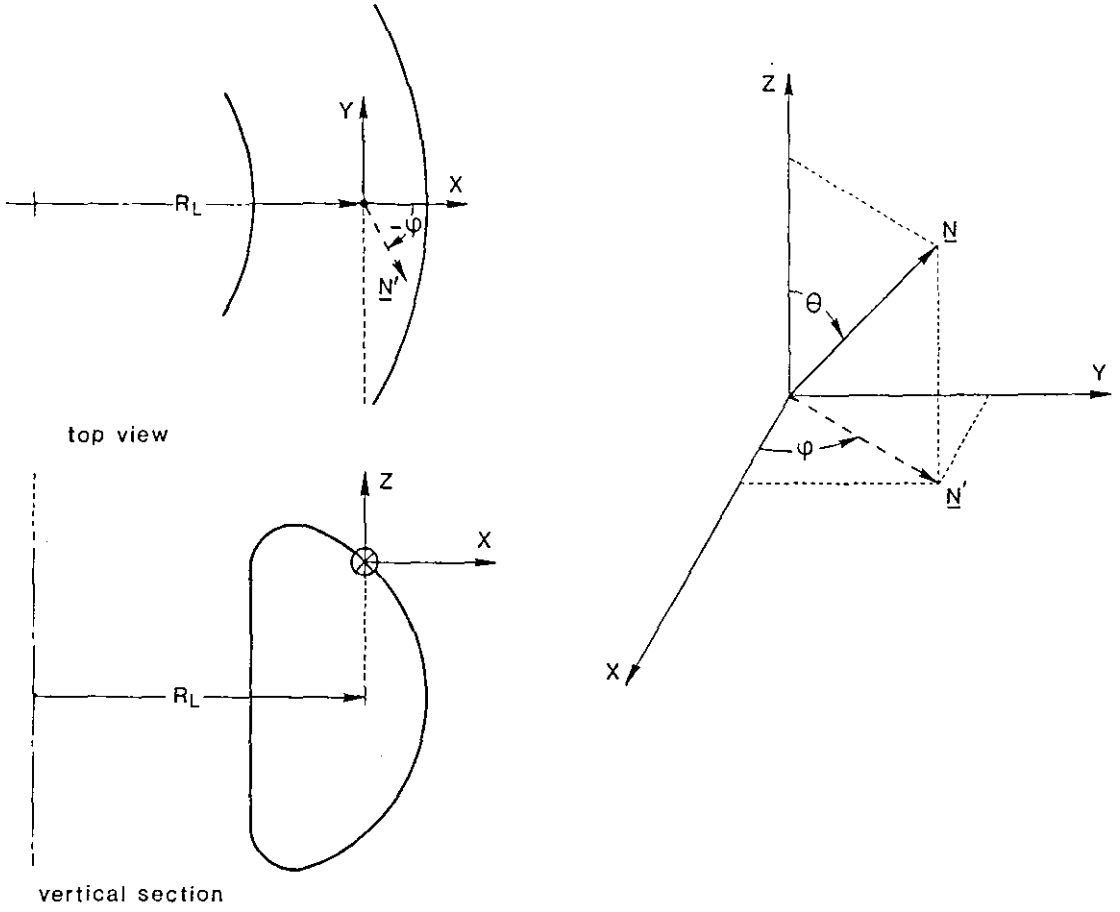

Fig.5. The coordinate system and spherical angles (θ,ϕ) - used in TORAY) - at the launching position.

depends on the parallel index of refraction $N_{||} = (B_T/B)N_T + (B_\nu/B)N_\nu$, where B_T is the toroidal and B_ν the poloidal component of the equilibrium magnetic field. Because of toroidal symmetry, the contribution $N_T = \sin\theta \sin\phi$ is conserved along a ray. For the range of ϕ-values under consideration, $N_{||}$ is mainly determined by the angle θ. Larger values of θ correspond to lower values of $|N_{||}|$.

4. POWER DEPOSITION IN REAL AND IN MOMENTUM SPACE

The dependence of the ray trajectories and of the power deposition on the injection angles is analyzed by scanning in ϕ at fixed θ and vice versa. In this Section we limit the discussion to Maxwellian plasmas without supra-thermal particles.

Figures 6 and 7 show the results of a θ-scan at $\phi = -80°$. The parameters of the corresponding equilibrium are given in column IIb of Table 1. The central density n_o is $5 \cdot 10^{19}$ m^{-3} and 10^{20} m^{-3}, respectively, and the central temperature is $T_o = 5$ keV. The projections of the ray paths on the poloidal plane are depicted in Figs. (6a, 7a), the projections on the equatorial plane in Figs. (6b, 7b), while in Figs. (6c, 7c) the relative power in the ray is represented as a function of $\bar{\psi}$, which is defined below Eq. (8).

For a broad range of injection angles complete absorption of the wave power occurs at medium as well as at high plasma densities. The power deposition along a ray takes place in a rather narrow band in $\bar{\psi}$. For increasing values of θ, the rays penetrate deeper into the plasma and the power deposition shifts to lower values of $\bar{\psi}$. Due to the lower value of $N_{||}$, and the higher values of ω_c/ω and density along these rays, the local power deposition decreases which leads to longer ray paths for complete absorption. This, however, does not necessarily imply a broader deposition profile in terms of $\bar{\psi}$. Figures (6c) and (7c) show clearly that a localized power deposition is possible over a rather wide $N_{||}$ spectrum.

The difference in ray patterns at $n_o = 5 \cdot 10^{19}$ m^{-3} and at $n_o = 10^{20}$ m^{-3} reflects the stronger diffraction effects and the reduced accessibility of the wave power to the centre at higher densities. However, a comparison of Figs. (6c) and (7c) shows that in spite of the differences in ray trajectories, a wide range in θ exists in which the density has only a weak influence on the position where the wave power is absorbed. For these values of θ the rays are diffracted more towards the outside of the torus when the density increases. Due to this increased diffraction, the rays travel along a magnetic surface over a longer distance. Together with the reduced absorption, this causes the localization of the power deposition to remain unchanged.

When the ray is diffracted towards the plasma periphery it enters a region where the temperature is lower. As a consequence, the wave power will be absorbed at a lower value of the magnetic field and at

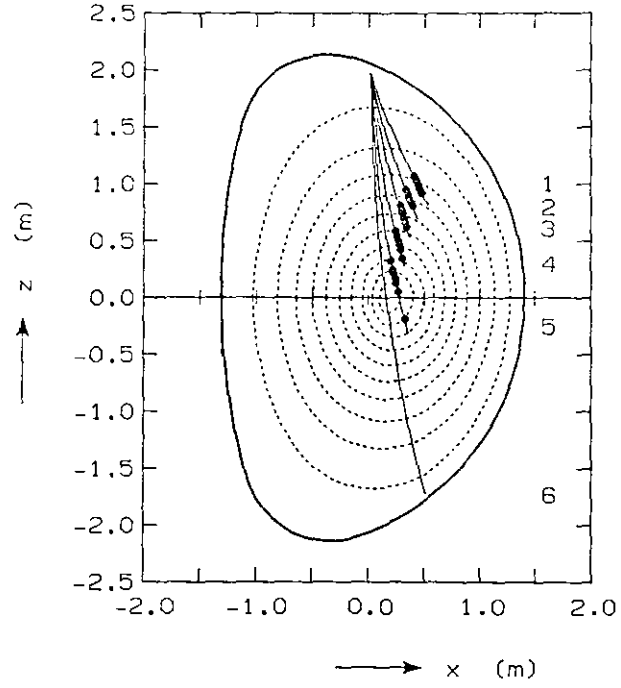
z (m)
x (m)
1
2
3
4
5
6

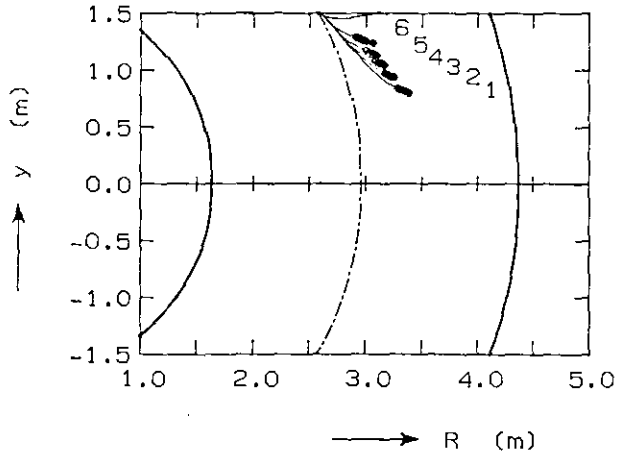
y (m)
R (m)
6
5
4
3
2
1

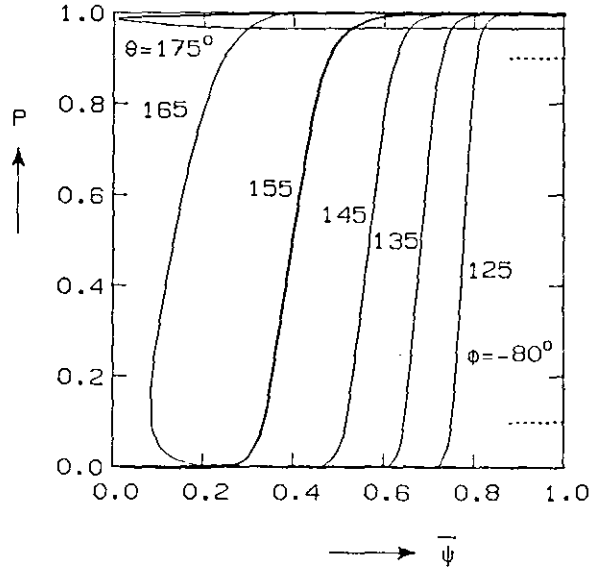
P
θ=175°
165
155
145
135
125
φ=-80°
$\bar{\psi}$

Fig. 6.

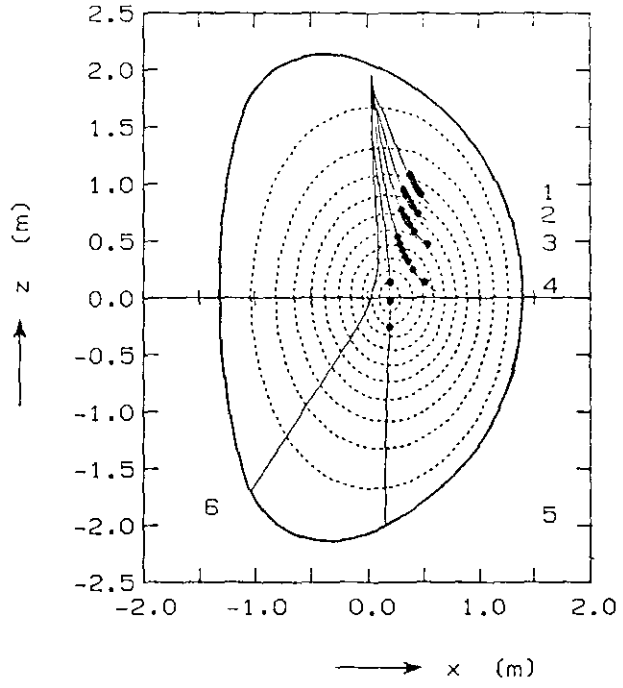
a
z (m)
x (m)
1
2
3
4
5
6

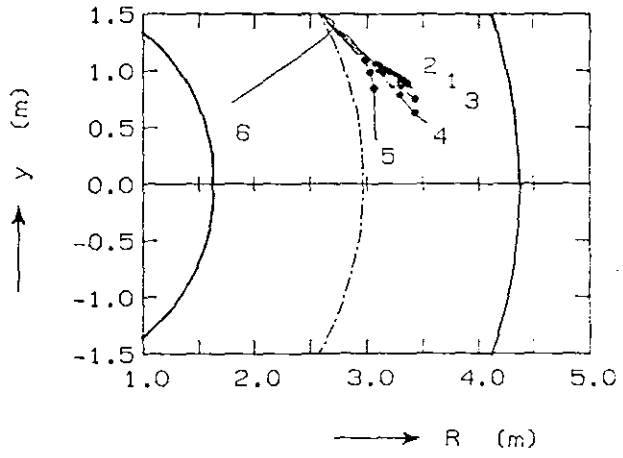
b
y (m)
R (m)
1
2
3
4
5
6

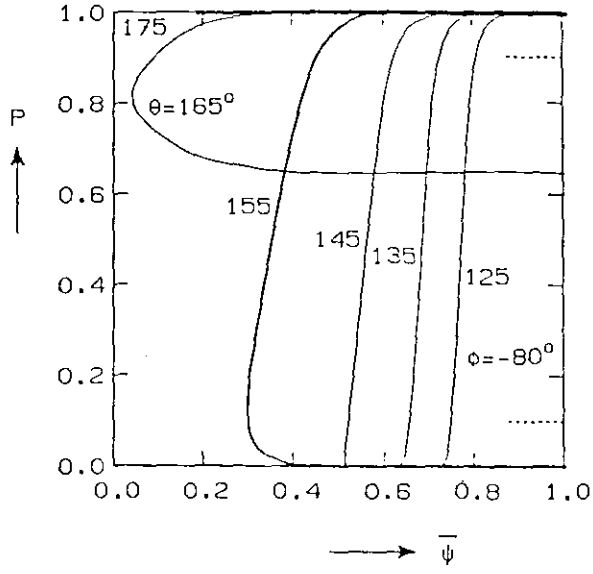
c
P
175
θ=165°
155
145
135
125
φ=-80°
$\bar{\psi}$

Fig. 7.

lower particle energies.

The discussion is summarized in Figs. 8 and 9, where the localization of the power deposition together with the particle energies at which this power is absorbed, are shown as a function of the injection angle θ for $\varphi = -80°$. The central density is $n_o = 0.5 \cdot 10^{20}$ m^{-2} in Fig. 8 and $1.0 \cdot 10^{20}$ m^{-3} in Fig. 9. The energies are the minimum values $\bar{E}$ calculated from (3a). The widths in the bands of $\bar{\psi}$ and $\bar{E}$ are the intervals in space and energy where the power in the ray falls from 90% to 10% of its initial value. An actual launching system will have a spread in injection angles due to the differences in orientation of the individual launchers and to the angular divergence of the antenna patterns. An estimate for the localization of the power deposition with such a launching system can be inferred from these figures.

For steeper injection, i.e., for larger values of θ, the power penetrates more into the centre of the discharge and is absorbed at higher particle energies. For too steep an injection, the ray still penetrates into the centre but the absorption along the ray falls abruptly. This is due to the fact that at the assumed plasma temperature of 5 keV, there are too few particles in the required energy range for good absorption. At higher plasma temperatures or in the presence of a small supra-thermal population in the appropriate energy range, the absorption along these rays will increase substantially. In this context it should be noted that when the rays are directed towards the low-field side of the torus, which is the case in the examples shown, the wave will first encounter the high energy range of the tail of the distribution function. This means that, at higher temperatures, the absorption tends to increase first at the upper boundary of the energy regions depicted in Figs. 8 and 9.

Fig. 6. Results of ray tracing in JET-3901 with $n_o = 0.5 \cdot 10^{20}$ m^{-3} and $T_o = 5$ keV. Centre top-launch (R = 3 m) at $\phi = -80°$ and $\theta = 125°$, 135°, 145°, 155°, 165°. a) Projections of the rays on the poloidial plane. b) Projections of the rays on the equatorial plane. c) Power in the ray as a function of $\bar{\psi}$.

Fig. 7. As Fig. 6 for $n_o = 1.0 \cdot 10^{20}$ m^{-3}.

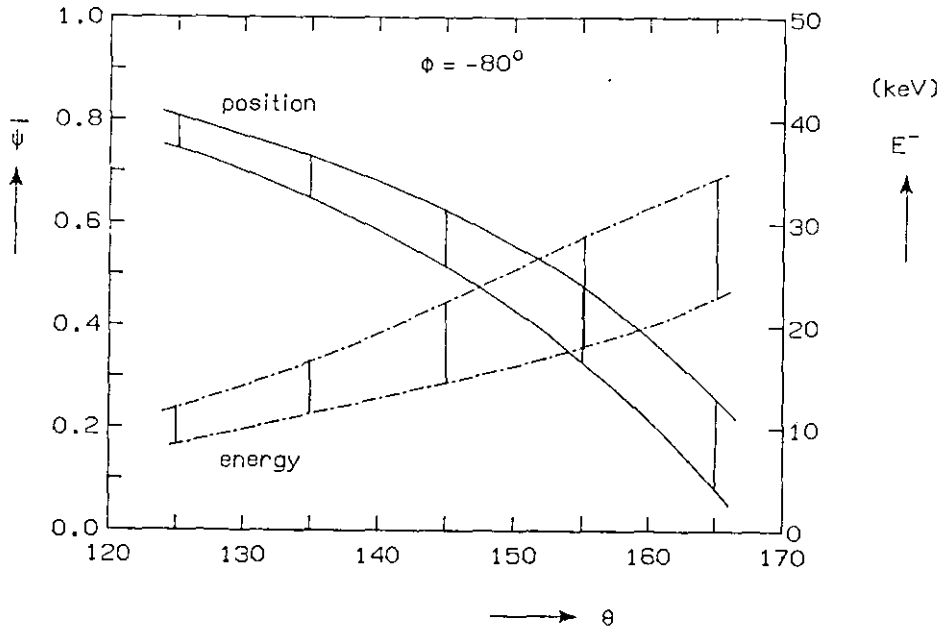

Fig. 8. The bands in $\bar{\psi}$ and in E^- within which the intensity drops from 90% to 10% of its initial value. Centre-top launch in JET-3901 with $n_o = 0.5 \cdot 10^{20}$ m^{-3} and $T_o = 5$ keV (see Fig. 6).

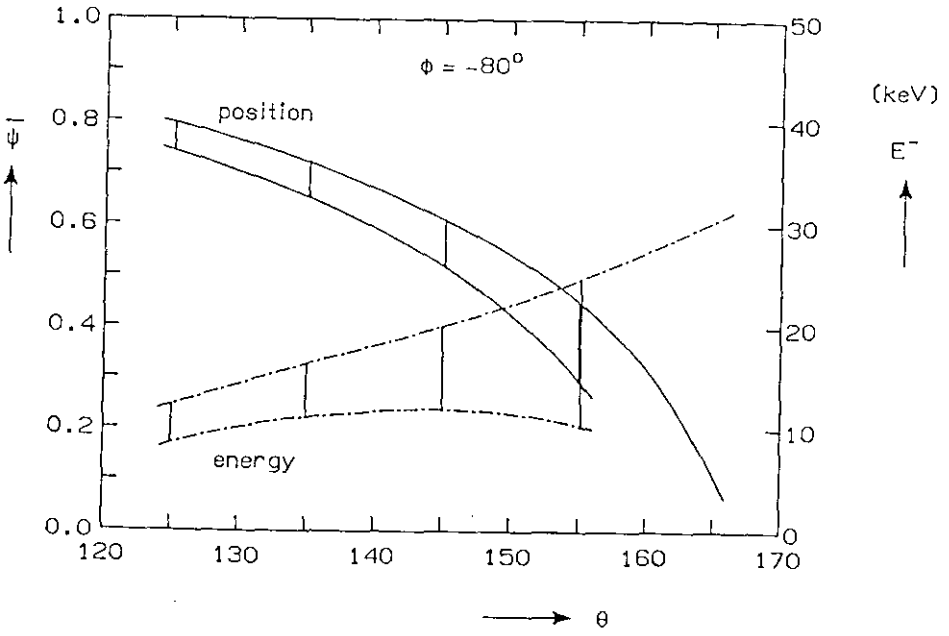

Fig. 9. The localization in space and energy for centre-top launch in JET-3901, $n_o = 1.0 \cdot 10^{20}$ m^{-3}, $T_o = 5$ keV (see Fig. 7).

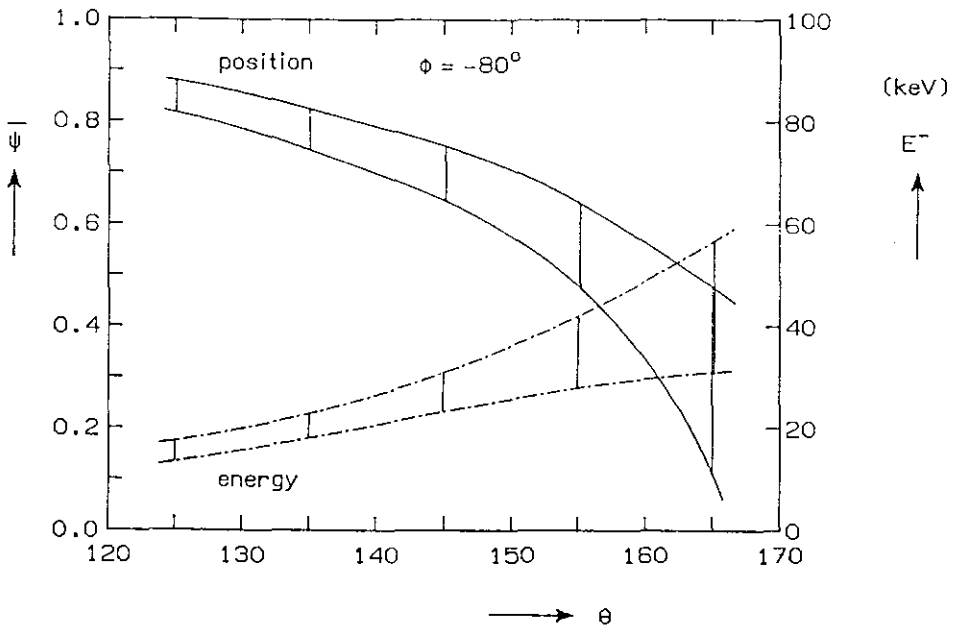

Fig. 10. The localization in space and energy for centre-top launch in JET-3901, $n_o = 1.0 \cdot 10^{20}$ m^{-3}, $T_o = 10$ keV.

Figure 10 shows the energy deposition for $T_o = 10$ keV and $n_o = 10^{20}$ m^{-3}. Upon comparing Figs. 10 and 9, we see that, for higher plasma temperatures, the absorption along a ray takes place closer to the source and therefore at higher values of $\bar{\psi}$ and higher particle energies.

Similar features as in a θ-scan can be recognized in a ϕ-scan at $\theta = 155^{\circ}$ as given in Figs. 11 and 12. In this scan $N_{||}$ has approximately the same value for all rays, so that these figures reflect the effects of the density and magnetic field profiles on the ray trajectories. Complete absorption, also at the higher density, takes place along rays that are directed towards the low-field side (i.e., $|\phi| < 90^{\circ}$). Note that for the relevant injection angles the spatial position and particle energies where the RF power is deposited depends less strongly on ϕ than on θ. The density influences only weakly the spatial position where the power is absorbed. Along rays that are injected towards the high-field side, ($|\phi| > 90^{\circ}$), the absorption is low, in particular at high density. Again, the absorption along these rays will increase at higher plasma temperatures or in the presence of a supra-thermal population. Figure 13 shows the results of a ϕ-scan for the $T_o = 10$ keV, $n_o = 10^{20}$ m^{-3} case. The corresponding θ-scan is given in Fig. 10.

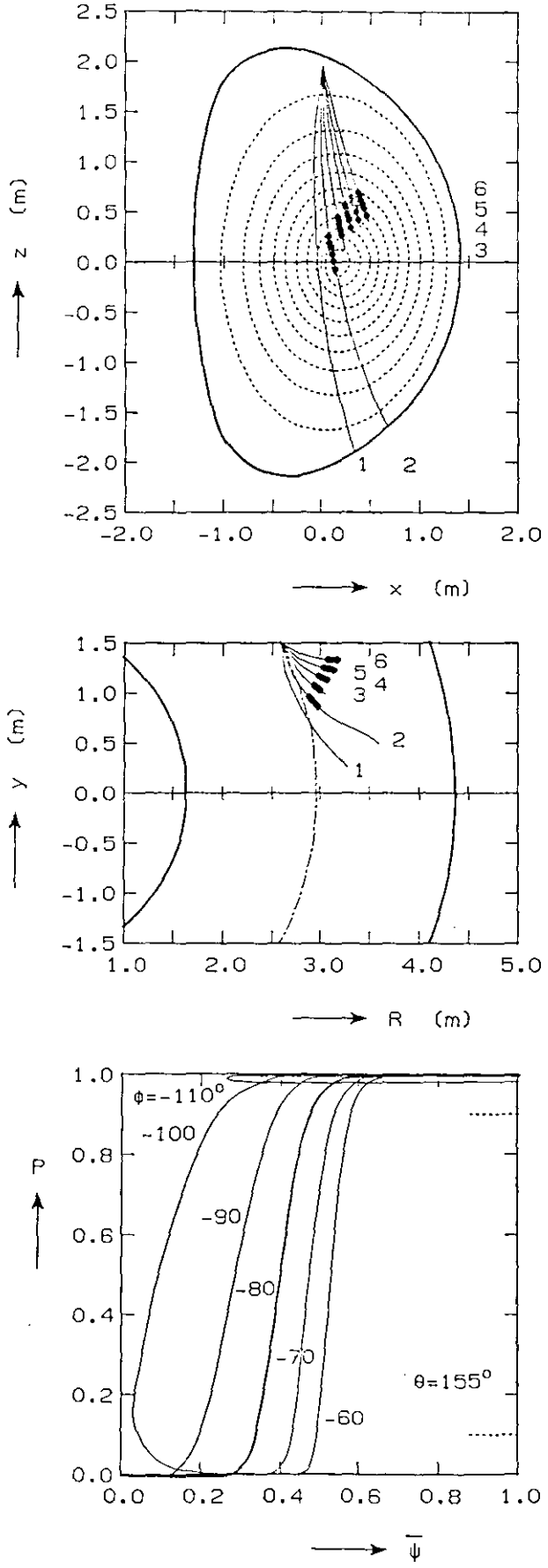
z (m)
x (m)
y (m)
R (m)
P
$\bar{\psi}$
1
2
3
4
5
6
ϕ=-110°
-100
-90
-80
-70
-60
θ=155°

Fig. 11.

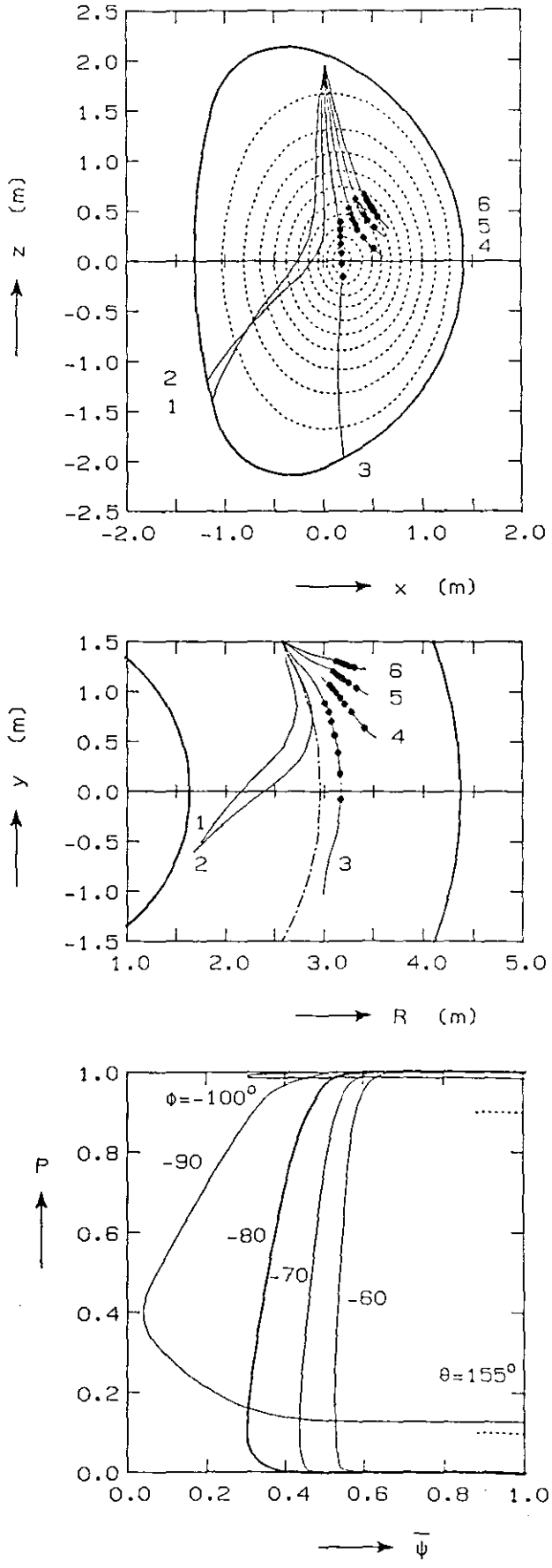
ⓐ
ⓑ
ⓒ
z (m)
x (m)
y (m)
R (m)
P
$\bar{\psi}$
1
2
3
4
5
6
ϕ=-100°
-90
-80
-70
-60
θ=155°

Fig. 12.

Fig. 11. A ϕ-scan at $\theta = 155^{\circ}$ in JET-3901 with $n_o = 0.5 \cdot 10^{20}$ m^{-3} and $T_o = 5$ keV (see also Figs. 6 and 8); $\phi = -110^{\circ}, -100^{\circ}, -90^{\circ}, -80^{\circ}, -70^{\circ}, -60^{\circ}$.

Fig. 12. A ϕ-scan as in Fig. 11 for $n_o = 1.0 \cdot 10^{20}$ m^{-3} (see also Figs. 7 and 9).

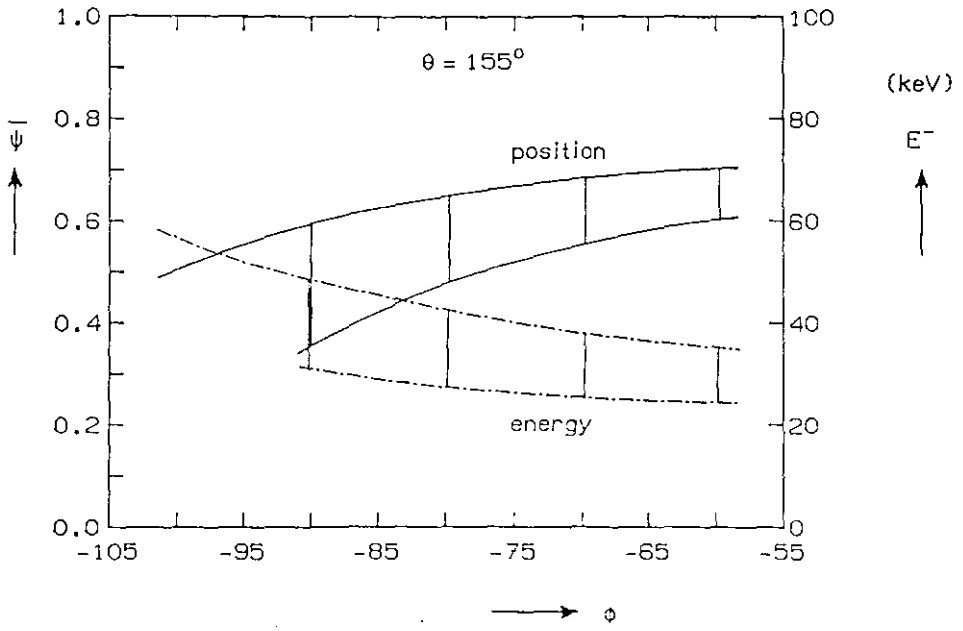

Fig. 13. The localization in space and energy for centre-top launch in JET-3901, $n_o = 1.0 \cdot 10^{20}$ m^{-3}, $T_o = 10$ keV.

Fig. 14. The results of θ-scans for injection from three launching positions into the equilibrium of column I of Table 1. Upper row: $n_o = 0.5 \cdot 10^{20}$ m^{-3}, $T_o = 5$ keV; middle row: $n_o = 1.0 \cdot 10^{20}$ m^{-3}, $T_o = 5$ keV; bottom row: $n_o = 0.5 \cdot 10^{20}$, $T_o = 10$ keV.

Fig. 15. The results of ϕ-scans at $\theta = 155^{\circ}$ corresponding to the cases of Fig. 14.

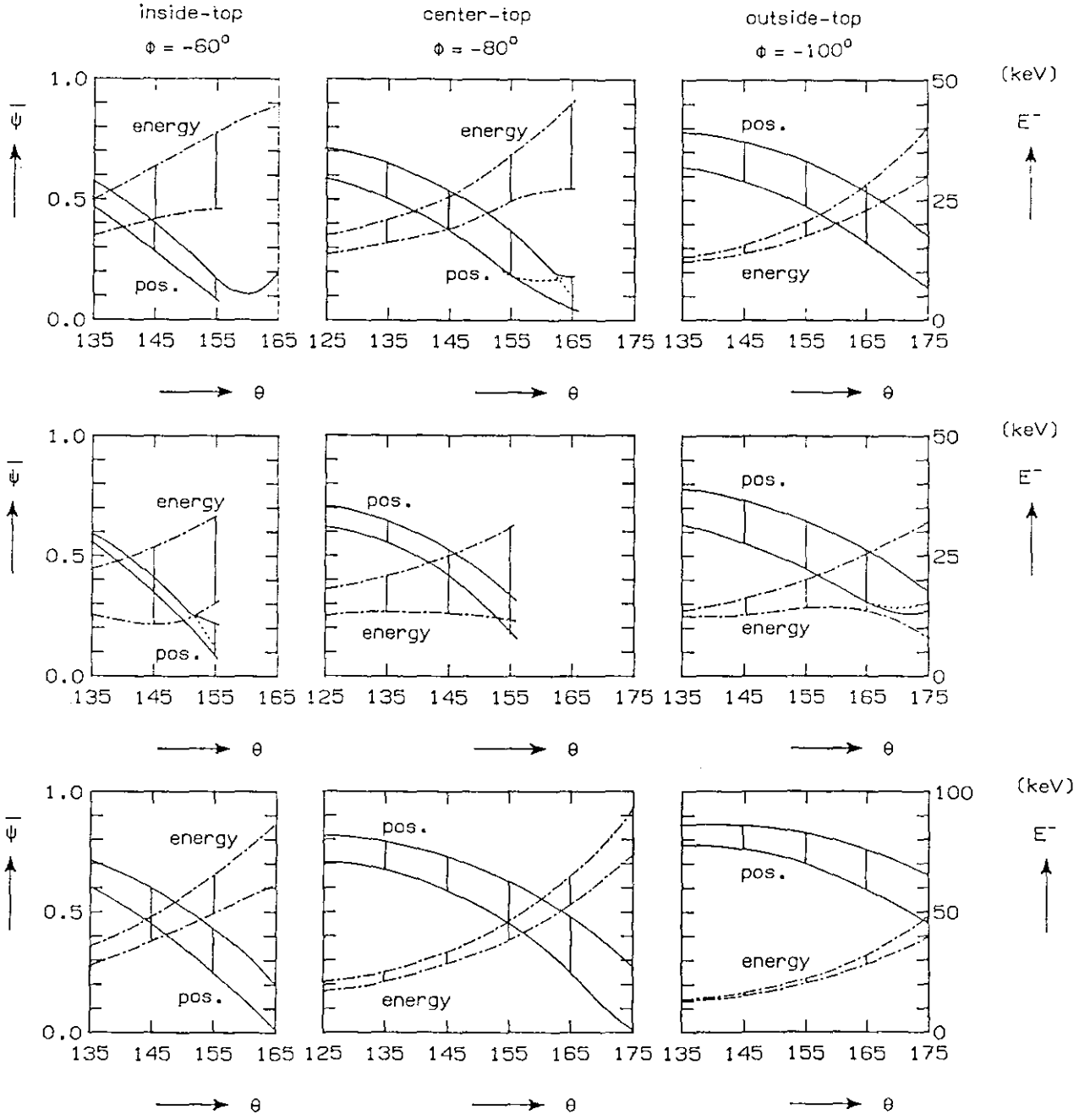
inside-top
Φ = -60°
center-top
Φ = -80°
outside-top
Φ = -100°
|ε|
1.0
0.5
0.0
energy
pos.
135 145 155 165
125 135 145 155 165 175
θ
(keV)
E⁻
50
25
0
100
50
0

Fig. 14.

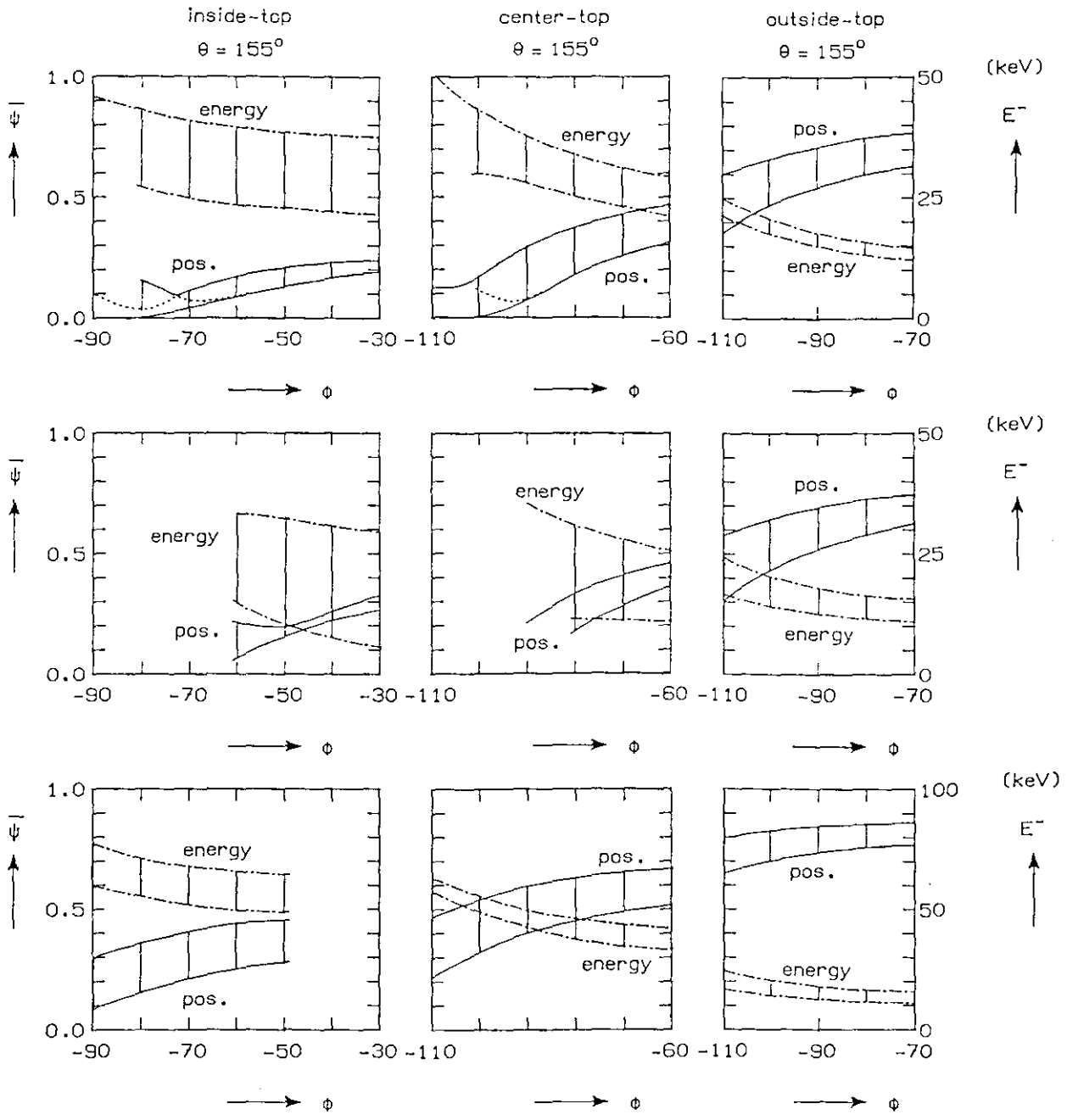
inside-top
θ = 155°
center-top
θ = 155°
outside-top
θ = 155°
(keV)
E⁻
|Ψ|
energy
pos.
1.0
0.5
0.0
50
25
0
100
-90
-70
-50
-30
-110
-60
Φ

Fig. 15.

Ray tracing results for power injection from three positions in a top-port are summarized in Figs. 14 an 15. These results apply to the equilibrium specified in column I of Table 1. Figure 14 shows θ-scans at $\phi = -60°$ for injection from the innermost high field side (R = 2.65 m) of the top port, at $\phi = -80°$ for centre-top (R = 3.0 m) launch, and at $\phi = -100°$ for injection from the outermost low-field side (R = 3.35 m) of the port. The corresponding ϕ-scans at $\theta = 155°$ are presented in Fig. 15. The figures in the top rows correspond to the plasma conditions $n_o = 0.5 \cdot 10^{20}$ m^{-3} and $T_o = 5$ keV, the middle rows to $n_o = 10^{20}$ m^{-3} and $T_o = 5$ keV, and the bottom rows to $n_o = 0.5 \cdot 10^{20}$ m^{-3} and $T_o = 10$ keV.

Upon comparing the centre launch results of Fig. 14 with those presented in Figs. 8 and 9, it is seen that, as far as the spatial localization of the power deposition and the range of particle energies are concerned, only minor differences exist between the results for the two equilibria.

In the cases represented in Figs. 14 and 15, good absorption is found for higher (θ,ϕ) values when R_{launch} is increased, i.e., the rays can be injected more steeply and more towards the high-field side when injected from positions with lower values of the magnetic field. With a proper choice of the injection angles for each launching position, the power can be deposited around the same flux surface and be absorbed by particles in the same energy range.

The variation of the magnetic field strength along a ray becomes smaller for larger values of R_{launch}. Consequently, the band ΔE^- in particle energies E^- becomes narrower when the rays are injected from positions with lower B_T-values. At higher temperatures, the power is deposited around surfaces with higher $\bar{\psi}$-values, but the particle energies remain approximately unchanged along these outer rays.

The ray trajectories are calculated from the cold dispersion relation (4). In the preceding pages the effects of the magnitude of the peak density on the ray paths and the power deposition were discussed. In Fig. 16 the influence of the profile of the density is investigated. The figure summarizes the results of a θ-scan at $\phi = -80°$ for centre top-launch into the equilibrium of column I of Table 1. The central values of the density and temperature are $n_o = 10^{20}$ m^{-3} and $T_o = 5$ keV. In Fig. 16a the parameters of the density profile (11) are $a_n = 1$, $b_n = 2$, $c_n = 2$, while in Fig. 16b they have the values $a_n = 1$, $b_n = 2$, $c_n = 3$.

These results have to be compared with the centre-top launch case of Fig. 14 (second row and second column), which holds for the same central values of density and temperature but for a parabolic density profile with $a_n = 1$, $b_n = 2$, $c_n = 1$. The calculations clearly show that, even at a density of 10^{20} m^{-3}, the profile of the density plays a minor role in the power deposition. This conclusion is generally true as long as the high-density cut-off (5) is not too close to the wave frequency.

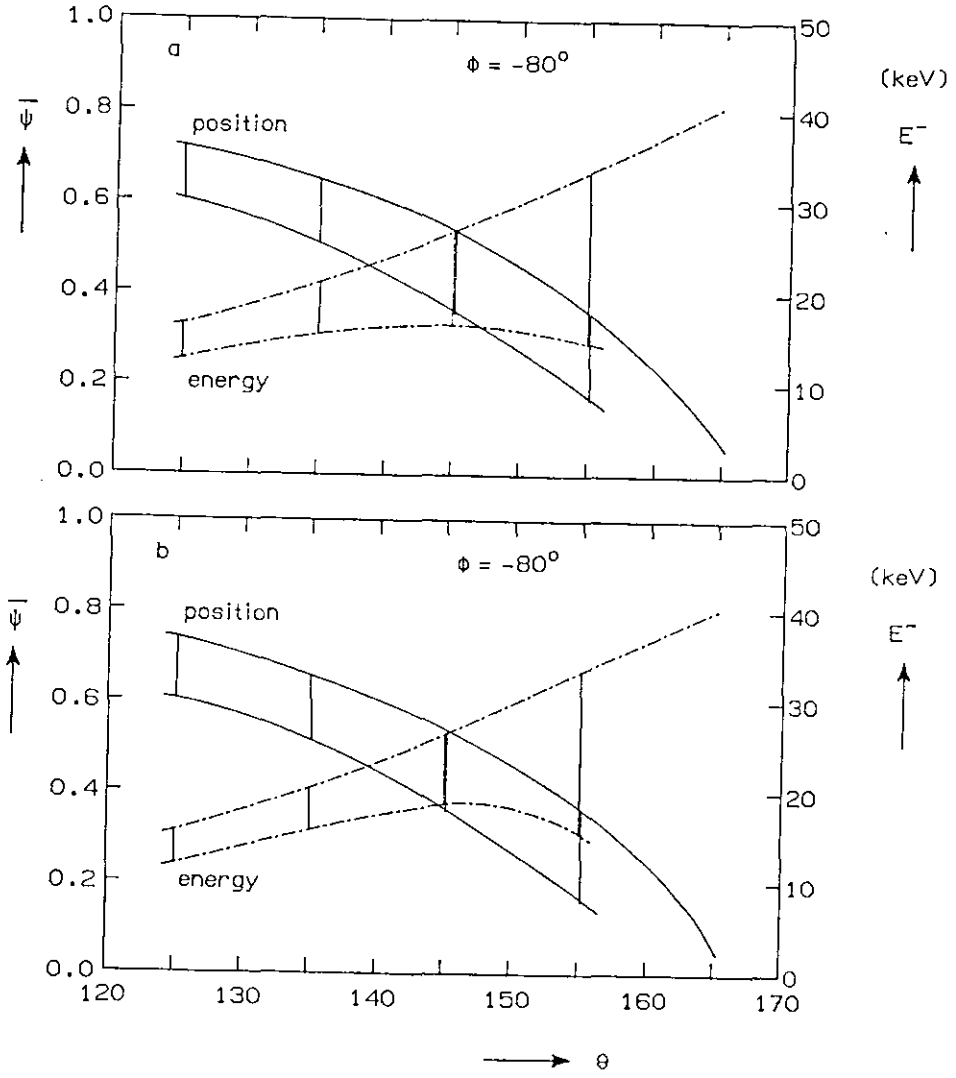

Fig. 16. A θ-scan of the equilibrium of column I of Table 1 for density profiles with different peaking factors c_n ($n_o = 10^{20}$ m^{-3}, $T_o = 5$ keV). a) $a_n = 1$, $b_n = 2$, $c_n = 2$; b) $a_n = 1$, $b_n = 2$, $c_n = 3$.

Up to now, we have investigated the equilibria described by the first two columns of Table 1. These equilibria are diamagnetic. In contrast, the low-q discharge represented in the last column is paramagnetic. The results of the ray tracing for $n_o = 0.5 \cdot 10^{20}$ m^{-3} and $T_o = 5$ keV in this case are represented in Fig. 17.

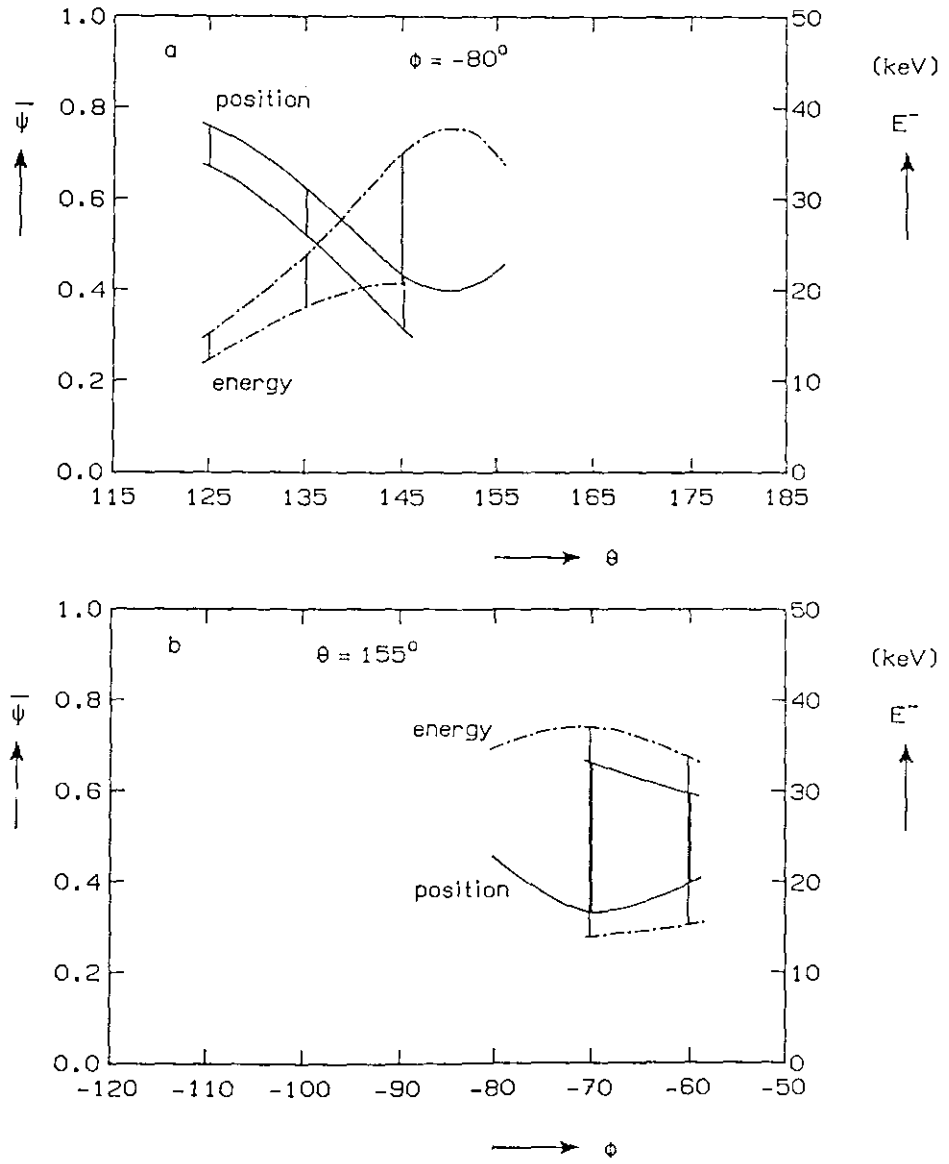

Fig. 17. A θ-scan (a) and a φ-scan (b) of the low-q shot JET-7774 with $n_o = 0.5 \cdot 10^{20}$ m^{-3} and $T_o = 5$ keV.

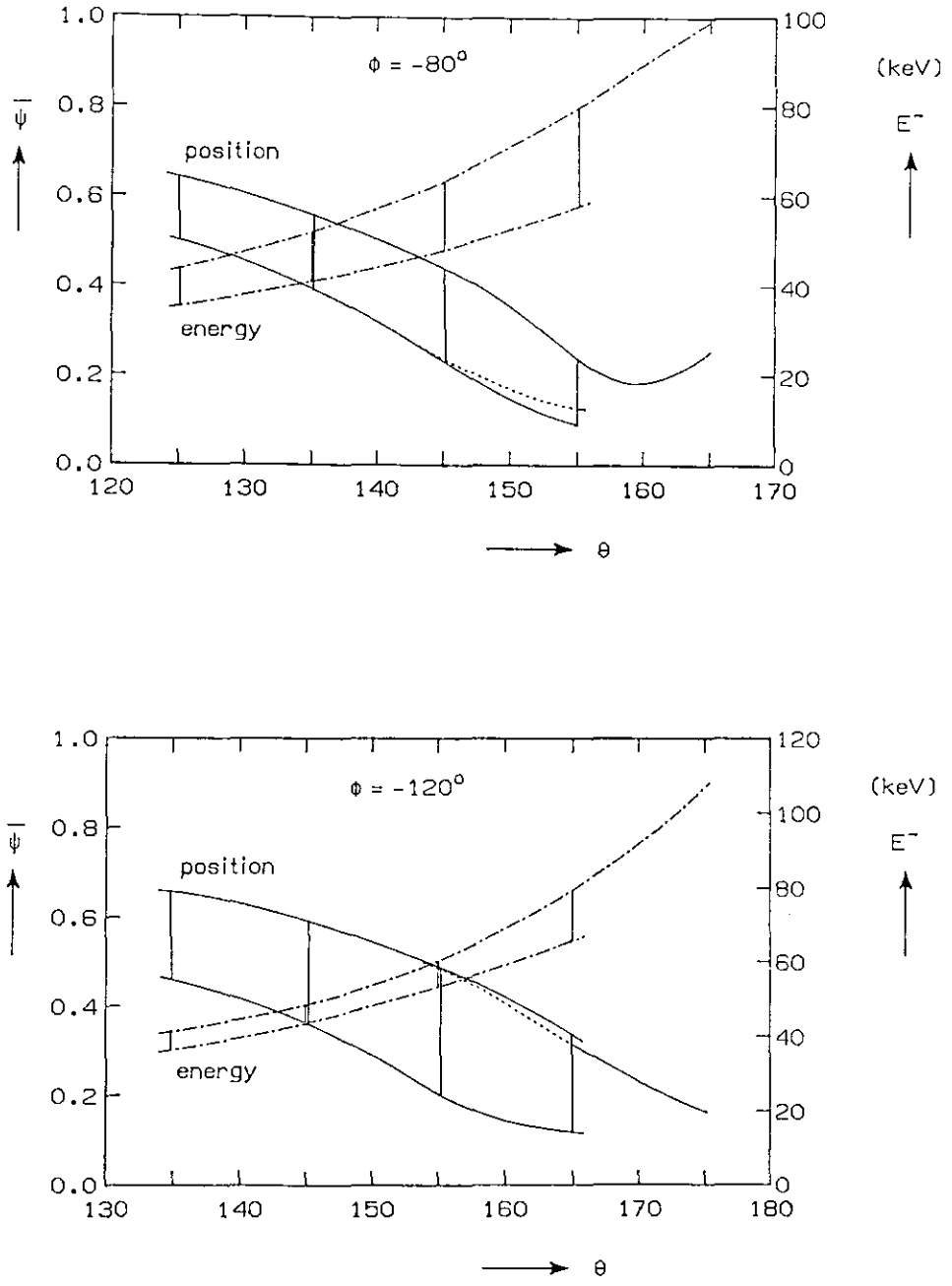

Fig. 18. A θ-scan at 60 GHz of the equilibrium of column I of Table 1 with $n_o = 0.5 \cdot 10^{20}$ m^{-3}, $T_o = 10$ keV and $B_T = 34$ kG; a) centre-top launch; b) outside top launch.

The rays are injected from the centre of the top-port. The differences between these results and those that are given in Fig. 8 and in the middle columns of Figs. 14 and 15 originate mainly from the higher values of the magnetic field in the absorption region in the paramagnetic case. Therefore, the absorption is lower (cf. Fig. 4), in particular along rays that are injected less towards the low-field side or more steeply into the plasma. This means that for 70 GHz waves, the centre is less accessible in the paramagnetic equilibrium. The absorption and the accessibility improves when the toroidal magnetic field is slightly lowered.

Finally, we consider waves with a frequency of 60 GHz. As has been pointed out already in the discussion of Eq. (5), those waves can only reach the centre of the discharge for central densities below 10^{20} m^{-3}. For the equilibrium of the first column of Table 1 with n_o = $0.5 \cdot 10^{20}$ m^{-3} and T_o = 10 keV, the results for rays injected from the centre of the top-port are shown in Fig. 18a. For lower central temperatures the absorption along the rays decreases considerably. At T_o = 5 keV, the range in injection angles where full absorption occurs becomes very small.

For the same discharge parameters, the rays do reach the centre when launched from the outside of the port, and the power is absorbed at rather high particle energies (Fig. 18b). Thus, in this specific case 60 GHz might be preferred to 70 GHz waves.

5. CURRENT DRIVE EFFICIENCY

The ray tracing calculations presented in the preceding Section lead to the conclusion that electron cyclotron wave power at 70 GHz can be completely absorbed in Maxwellian JET plasmas with central densities n_o = $0.5\text{-}1.0 \cdot 10^{20}$ m^{-3} and temperatures T_o = 5-10 keV. The RF power is transferred to electrons in the tail of the distribution function. The power deposition is spatially localized for a broad range of injection angles and positions. At the lower densities and higher temperatures, the absorption is larger. In addition, the power can be injected more steeply into the discharge. Consequently, the power can be deposited closer to the plasma centre where it is absorbed by particles with higher energies.

For several discharge conditions, the appropriate energy ranges for near-centre deposition in a Maxwellian plasma are summarized in the Table on page 27.

CENTRE-TOP LAUNCH

T_o	n_o	E^- (I)	E^- (IIb)
5 keV	$0.5 \cdot 10^{20}$ m^{-3}	30-45 keV	25-35 keV
5	10^{20}	15-35	10-25
10	$0.5 \cdot 10^{20}$	75-95	60-80
10	10^{20}	50-65	35-55

INSIDE-TOP LAUNCH

5 keV	$0.5 \cdot 10^{20}$ m^{-3}	35-40 keV
5	10^{20}	15-35
10	$0.5 \cdot 10^{20}$	65-90
10	10^{20}	40-65

Table 2. Particle energies E^- for near-centre power deposition in the equilibria specified in column I and IIb of Table 1.

The non-inductive current I that is generated by a point spectrum of electron cyclotron waves is discussed in Refs. [16] and [17]. According to this theory, the current that can be carried by relativistic particles with energy $mc^2 (\gamma - 1)$ and parallel momentum $p_{\parallel}$ is

$$\frac{I}{W} = \frac{1}{2\pi R} \frac{J}{P_d} = \frac{1{,}05}{R(m) n_{20}} \left(\frac{J}{P_d} \right)_n \quad A/W, \tag{12}$$

where R is the major radius, n_{20} the density in 10^{20} m^{-3}, W the total power in the wave and $(J/P_d)_n$ the normalized efficiency [16]:

$$\left(\frac{J}{P_d} \right)_n = N_{\parallel} G(p/mc) + \gamma \frac{p_{\parallel}/mc}{p} \frac{dG}{dp} , \tag{13a}$$

with

$$G(p/mc) = \frac{2}{p/mc} \left(\frac{\gamma + 1}{\gamma - 1} \right)^{\frac{1+Z_{eff}}{2}} \int_0^{p/mc} dx \left(\frac{x}{\gamma} \right)^3 \left(\frac{\gamma - 1}{\gamma + 1} \right)^{\frac{1+Z_{eff}}{2}} . \tag{13b}$$

These expressions are valid for $p^2 >> mT$ and plasma temperatures $T < mc^2$. For the energies under consideration we have as a good approximation

$$\frac{I}{W} = \frac{6}{5 + Z_{eff}} \left.\frac{I}{W}\right|_{Z_{eff}=1} . \qquad (14)$$

The quantity I/W is plotted in Fig. 19 as a function of particle energy for R = 3m, n_{20} = 0.5 and Z_{eff} = 1. We have taken $P_{\perp}$ = 0 so that all the energy is in the parallel motion of the particles. Thus, we assume that all the wave power is absorbed by resonant particles with the lowest energy E^- (see Eq. (3a) and Fig. 2). The spatial position and the energies E^- where the wave power is deposited, are given by the ray tracing results.

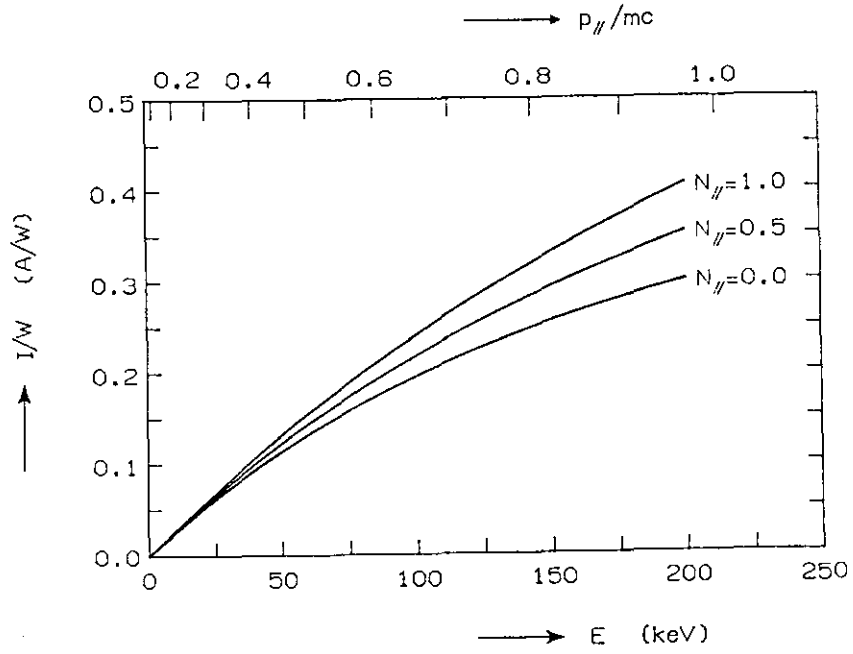

Fig. 19. The current generated in JET (R = 3 m) by RF power as a function of particle energy for Z_{eff} = 1 and n = $0.5 \cdot 10^{20}$ m^{-3}.

From the figures in Table 2 and from Fig. 19, the following rough estimate is obtained for the efficiency of current drive with central power deposition in JET plasmas,

$$\left.\frac{I}{W}\right|_{Z_{eff}=1} = \alpha \frac{T_o(10^4 \text{ eV})}{n_{20}} \text{ A/W} , \qquad (15)$$

where α = 0.1 for the temperatures and densities under consideration.

The energy values given in Table 2 are obtained for rays along which barely complete absorption occurs. Although these values are not optimized with respect to the injection angles, they are close to the maximum values that can be attained. An actual launching system will have a spread in injection angles due to the differences in orientation of the individual launchers and to the angular divergence of their antenna patterns. In order to achieve complete absorption of the total beam, the centre of the beam should not be aimed at those maximum values. This will reduce the current drive efficiency. Therefore, it would be more realistic to take $\alpha = 0.05 - 0.1$ for the coefficient in (15). Heating of the bulk of the electrons, inevitably associated with current drive, will augment the absorption and the efficiency. On the other hand, collisional scattering of high energetic particles into trapped orbits will reduce the current drive efficiency.

As an example, the profiles of power deposition and of the driven current have been calculated for an equilibrium similar to discharge 7774. With the exception of the magnetic field which has been rescaled to 3.2 T at R = 2.96 m, the parameters of this equilibrium are given in column IIIb of Table 1 with $n_o = 0.5 \cdot 10^{20}$ m^{-3} and T_o = 5 keV. This choice of the toroidal field optimizes the absorption around the q=1 surface (r ≈ 45 cm). The total power is 1 MW and is injected by two beams of 0.5 MW each from opposite sides of the centre of the top-port (R = 2.94 m and 2.96 m). Each beam is modelled with 13 rays. The geometry of the rays and the power for each ray are chosen such that the beam is approximately Gaussian with $\Delta\theta = \Delta\phi = 5°$. The injection angles of the central rays of the beams are $\theta = 150°$, $\phi = -80°$ and $\theta = 155°$, $\phi = -80°$, respectively. With these values the two beams overlap in the poloidal plane, in the region where the absorption occurs. The results of the calculations are presented in Fig. 20. In the figure, $P(r) = \Sigma \Delta P_{p\ell}/\Delta V$ and $j(r) = \Sigma (I/W)_\ell \Delta P_{p\ell}/\Delta S$ are plotted versus $r = (S/\pi)^{\frac{1}{2}}$. Here, ΔV and ΔS are the volume and the poloidal surface area enclosed by two magnetic surfaces between which a power $\Delta P_{p\ell}$ is deposited, and $(I/W)_\ell$ is the local current drive efficiency obtained from (12) for the energies E^- as in Fig. 19. The summation is over the rays in the beams. The figure shows that $j(r) \approx P(r)$ which according to (12), yields an overall efficiency $I/W \approx 0.05$ A/W, in agreement with (15).

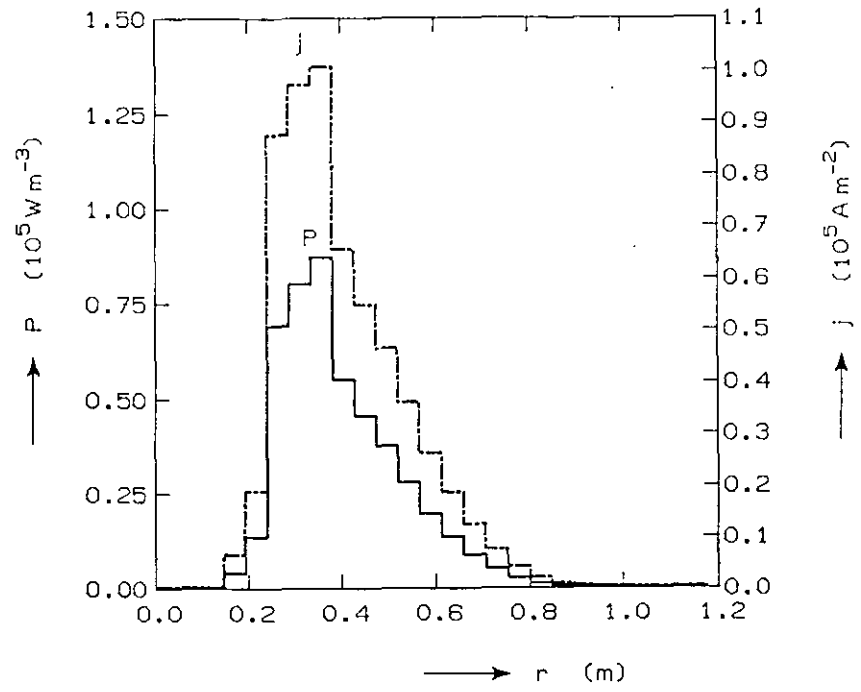

Fig. 20. Power deposition and current profile in JET 7774. Two Gaussian beams (half width 5°) of .5 MW are launched at R = 2.94 and 3.06. The injection angles of the beam centres are $\theta = 150°$, $\phi = -80°$ and $\theta = 155°$, $\phi = -80°$.

The widths of the profiles are mainly due to the angular spread of 5° of each beam and are to a lesser extend the result of the different absorption lengths along the indiviual rays. Hence, the localization of the power deposition and of the driven current depends to a large extend on the qualities of the launching system.

6. SUPRA-THERMAL ELECTRON GENERATION

The numerical results presented in the preceding Sections depend crucially on the properties of the absorption coefficient (7). This coefficient has been derived for a Maxwellian plasma. This means that the power deposition and the current drive efficiency are calculated under the assumption that the RF power is absorbed by high-energetic, resonant particles without distorting the Maxwellian character of the tail of the distribution function. A necessary condition for the validity of these results is, thus, that collisions are sufficiently frequent so that the RF power can be transferred to the bulk

of the distribution function by collisional energy loss of resonant particles. When this condition is not fulfilled, resonant particles will run away in momentum space [18] and strong non-Maxwellian effects can be expected.

The power lost per unit volume by high energetic particles with density n_s due to collisions with bulk particles is

$$P_{coll} = n_s m_e v^2 \nu_c(v)$$

$$= 6 \cdot 10^3 \alpha_s \frac{n_{20}^2}{E^{1/2}(keV)} \quad MW\ m^{-3}, \tag{16}$$

where $\nu_c = \omega_{pe}^4 \ln\Lambda / 4\pi n v^3$ is the collision frequency ($\ln\Lambda = 15$ has been taken), and α_s is the fraction of resonant particles. For a Maxwellian distribution function we have

$$\alpha_s \approx \frac{1}{\pi^{3/2}} \left(\frac{E}{T}\right)^{1/2} e^{-E/T} \frac{\Delta E^-}{2T} \Delta\Omega. \tag{17}$$

Along a resonance curve, the thermal spread in energy $(\Delta E)_T$ and solid angle $\Delta\Omega = 2\pi \Delta p_{||} / p$ are related through the resonance condition (2),

$$\Delta\Omega \approx \frac{2\pi}{N_{||}} \frac{(2T/mc^2)^{1/2}}{(E/T)^{1/2}} \left(\frac{\Delta E}{2T}\right)_T \tag{18}$$

Combining Eqs. (16) - (18) gives

$$P_{coll} \simeq 0.4 \cdot 10^3\ n_{20}^2 \frac{1}{N_{||}} \frac{e^{-E/T}}{(E/T)^{1/2}} \frac{(\Delta E)_T}{2T} \frac{\Delta E^-}{2T} \quad MW\ m^{-3}. \tag{19}$$

According to the ray tracing results, the RF power is absorbed in a volume of the order of 10 m^3 when the launching conditions are optimized for near-centre deposition. Further, Table 2 shows that, at the higher temperatures, the spread in energies E^- is of the order of the thermal spread, $\Delta E^- \approx (\Delta E)_T = 2T$. In Fig. 21, the collisional power $W_{coll} = P_{coll} V$ lost by resonant particles is plotted as a function of normalized energy E/T for $N_{||} = 0.25$ (i.e., $\theta \approx 165^\circ$), $V = 10\ m^3$, $\Delta E/2T = 1$, and for the densities $n_{20} = 0.5$ and 1.

From this figure and Table 2 it follows that, e.g., for a total RF power (W_{RF}) of 5 MW, supra-thermal effects can be expected at low densities, while for $n_o = 10^{20}\ m^{-3}$ no large supra-thermal production will

occur. However, when the launching conditions are optimized for central deposition, the power is absorbed in a smaller volume so that supra-thermal effects can be expected also at higher densities [19]. The deposition volume could be reduced further, if it is technically feasible to limit the angular spread of a beam to less than 10°.

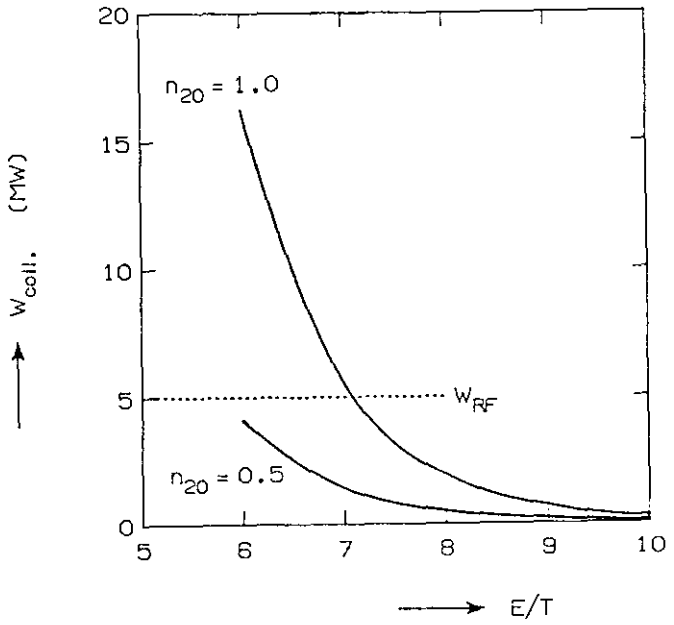

Fig. 21. Collisional power loss of resonant particles in a volume of 10 m^3 as a function of normalized energy. a) $n_{20} = 0.5$; b) $n_{20} = 1$.

In the run-away regime a depletion of the distribution function will occur unless particles are continuously supplied from the bulk at the lower energy boundary of the resonant population. Resonant particles will accumulate at the high energy boundary of the resonant region and be redistributed by pitch-angle scattering. A strongly non-Maxwellian distribution function will then be established in the resonant region. This necessitates a reconsideration of the absorption coefficient which has been used in the calculation of the power deposition and is based upon a thermal distribution. A consistent approach to the problem of power deposition and current drive in a non-Maxwellian plasma would require non-linear Fokker-Planck calculations and relevant knowledge about the confinement properties of supra-thermals. Such considerations are outside the scope of this report.

The deposition profile and the range of particle energies where the power is absorbed will change drastically when a non-Maxwellian distribution function is formed. To illustrate this point we reconsider the equilibrium of column IIIb of Table 1 with $n_o = 0.5 \cdot 10^{20}$ m^{-3} and $T_o = 10$ keV. In a Maxwellian plasma, the power in rays with $\theta \approx 155°$ (at $\phi = -80°$) and with $\phi > -90°$ (at $\theta = 155°$) is fully absorbed by particles with energies around 50 keV. We assume that the power in these rays produces a suprathermal population inside the volume enclosed by the surface $\bar{\psi} = 0.6$ This population is modelled with a distribution function which is Maxwellian in a frame moving along the magnetic field with a velocity corresponding to 50 keV, i.e., $\langle v_{||} \rangle = 0.331$ c m/sec. The supra-thermal density is $n_s = 10^{-2}\ n_o$ and the temperature is $T_s = 50$ keV. This velocity and density are clearly not realistic from the point of view of the related supra-thermal current, but here we consider power deposition. The results of (θ,ϕ)-scans are given in Fig. 22. The full and chain dotted lines represent the results with, and the dashed lines those without the supra-thermal population.

The figure shows that the absorption increases drastically and shifts to the boundary of the volume that contains the high-energetic electrons. Rays that are injected very steeply and in the direction of the high field side are fully absorbed. The power in these rays is deposited in the tail of the supra-thermal population, and particle energies up to 200 keV are reached. Consequently, the current drive efficiency will be greatly enhanced over that in a thermal plasma.

Although, in JET, the runaway velocity is close to the speed of light, cross-effects with the toroidal electric field on the high-energetic electrons may be expected.

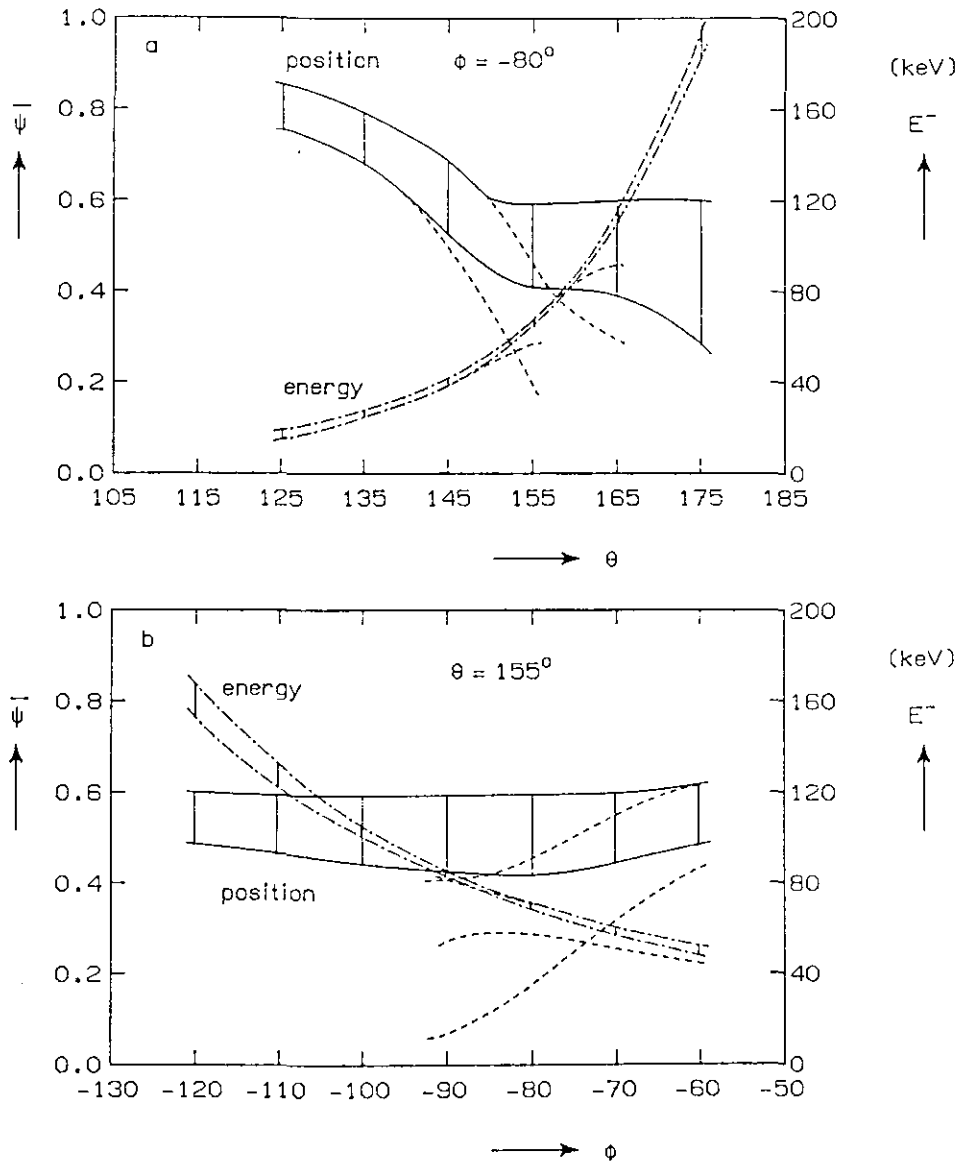

Fig. 22. Ray tracing results in the presence of a supra-thermal population. The dashed bands correspond to a purely Maxwellian plasma. a) A scan in θ at $\phi = -80^{\circ}$; b) a scan in ϕ at $\theta = 155^{\circ}$.

7. SUMMARY AND CONCLUSIONS

The power deposition by electron cyclotron waves at 70 GHz injected from a top-port into JET plasmas, has been studied by means of a ray-tracing code. Calculations have been performed for a wide range of plasma parameters, characteristic for present and future operations of JET. D-shaped plasmas with peak densities of 0.5 and $1.0 \cdot 10^{20}$ m^{-3}, and with peak temperatures of 5 and 10 keV have been investigated. The toroidal magnetic field is chosen to be at its maximum value, B_T = 34 KG.

In all cases, full absorption is shown to occur for a broad range of injection angles. The density has only a weak influence on the position where the wave power is absorbed up to densities close to the cut-off value. Only minor changes in the results are found for density profiles with strongly different peaking factors. For higher temperatures the deposition band narrows somewhat and shifts to higher values of ω_c/ω, and rays directed more towards the centre and towards the inboard side show increased absorption. Results for power injection from several positions in a top-port show that rays can be injected more steeply and more towards the high-field side when injected from positions with larger major radii.

The wide range in plasma parameters and injection angles allows a good control over the radial power deposition by properly choosing the injection geometry. The spatial localization of the power deposition is limited by the angular spread in individual wave-beams. The centre becomes less accessible at densities above 10^{20} m^3, due to the high-density cut-off of the X-mode.

Top-launch at 70 GHz does result in absorption by resonant particles in the tail of the electron distribution function. Particles with energies up to 10 times thermal absorb an appreciable fraction of the RF power in a Maxwellian plasma. At lower wave-frequencies the absorption decreases, while at higher frequencies the RF power is transferred to particles with lower energies.

The beneficial features of the absorption of the X-mode at a down-shifted frequency yield a favourable current drive efficiency. For JET, an efficiency of 0.05-0.1 A/W can be expected in a plasma with thermal electrons.

Under properly optimized launching conditions, supra-thermal effects are expected to occur for a few MW of RF power. The generation of a supra-thermal population will alter drastically the absorption and will lead to energy transfer to highly energetic particles in the tail of the supra-thermal distribution. Such a process will improve the current drive efficiency.

Our main conclusion is that EC power injection as discussed in this paper is attractive for current profile control in JET.

ACKNOWLEDGEMENTS

Fruitful discussions with Prof. Dr. F. Engelmann are gratefully acknowledged. We thank Dr. R.M.J. Sillen for supplying the module which describes the JET equilibrium. This work was performed under the Euratom-FOM association agreement with financial support from ZWO and Euratom.

REFERENCES

[1] P.H. Rebut, M. Brusati, Plasma Phys. and Contr. Fusion 28 (1986) 113.

[2] M. Murakami et al., Plasma Phys. and Contr. Fusion 28 (1986) 17.

[3] B. Coppi, Comments on Plasma Phys. and Contr. Fusion **V** (1980) 261.

[4] J. Jacquinot, Note for the JET Scientific Council Meeting no. 26.

[5] H.P. Furth, Plasma Phys. and Contr. Fusion 28 (1986) 1305.

[6] E. Mazzucato, I. Fidone, G. Giruzzi, V. Krivensky, Plasma Phys. and Contr. Fusion, 28 (1986) 1515.

[7] I. Fidone, G. Giruzzi , G. Granata and R.L. Meyer, Phys. Fluids 27 (1984) 661.

[8] I. Fidone, G. Giruzzi and E. Mazzucato, Phys. Fluids, 28 (1985) 1224.

[9] H. Weitzner, D.B. Batchelor, Phys. Fluids 23 (1980) 1359.

[10] M. Bornatici, R. Cano, O. De Barbieri and F. Engelmann, Nucl. Fusion 23 (1983) 1153.

[11] M. Bornatici, U. Ruffina, Il Nuovo Cimento 6 (1985) 231.

[12] M. Bornatici, U. Ruffina and E. Westerhof, Plasma Phys. and Contr. Fusion 28 (1986) 629.

[13] A.H. Kritz, H. Hsuan, R.C. Goldfinger, D.B. Batchelor, PPPL-1980 (1983).

[14] D.B. Batchelor, R.C. Goldfinger, ORNL/TM-6844.

[15] R.M.J. Sillen, Thesis, University of Utrecht, 1986.

[16] N.J. Fisch, Phys. Rev. A 24, 6 (1981) 3245.

[17] C.F.F. Karney and N.J. Fisch, Phys. Fluids 28 (1985) 116.

[18] L. Demeio, F. Engelmann, in Proc. Workshop on Mathematical Aspects of Fluid and Plasma Dynamics, Trieste (1984) 201.

[19] T.J. Schep, R.W. Polman, E. Westerhof, L. Klieb, 11th Int. Conf. on Plasma Phys. and Contr. Nucl. Fusion, Kyoto, Japan (1986), paper F-IV-5.

III Some Remarks on Non-Inductive Current Profiles, I.R. 86/053.

FOM-Instituut voor
Plasmafysica
Rijnhuizen
Nieuwegein

I.R. 86/053

SOME REMARKS ON NON-INDUCTIVE CURRENT PROFILES

W.J. Goedheer and T.J. Schep

Association Euratom-FOM, FOM-Instituut voor Plasmafysica
"Rijnhuizen" Nieuwegein, The Netherlands

INTRODUCTION

Within the context of recent discussions of sawtooth stabilization two modes of non-inductive current drive are considered. A reverse current is driven in the centre such that the total current density on axis drops below a critical value and the q=1 surface is suppressed. This scheme has been proposed in Ref. [1], considering NBI. Keeping the total current fixed, the Ohmic current will increase under reverse current drive and the volt-seconds consumption will be higher. In addition, due to the good confinement in the centre of the plasma, the corresponding increase in the conductivity tends to reduce the efficiency of the reverse current. The other possibility is to drive a forward current off-axis, as proposed in Ref. [2] for LHCD, such that the total Ohmic current decreases and $q > 1$ everywhere. With this method the current profile in the confinement region is modified. This could have a large effect on MHD stability.

In this report we briefly reconsider the situation of reverse and forward current drive. We look at global ways to modify the Ohmic current profile in order to obtain $q > 1$ everywhere, and also consider more local modifications of the current profile, intended to change the q-profile around the q=1 surface.

The calculations have been performed for peaked inductive current profiles as one would expect in a non-sawtoothing plasma with a current density coupled to the electron temperature.

NON-INDUCTIVE CURRENT PROFILES REQUIRED FOR q > 1 EVERYWHERE

Consider a magnetized plasma cylinder which carries a total current I_t and has the value q(a) of the safety factor at the limiter. The Ohmic current I_Ω is assumed to have the profile

$$J_\Omega(r) = J_\Omega(o)(1 - r^2/a^2)^\alpha, \quad J_\Omega(o) = \frac{\alpha + 1}{\pi a^2} I_\Omega. \tag{1}$$

In this discharge a reverse current I_R with the distribution

$$J_R(r) = J_R(o)(1 - r^2/r_o^2)^\beta, \quad J_R(o) = \frac{\beta + 1}{\pi r_o^2} I_R. \tag{2}$$

is driven in the centre.

In addition, a forward current I_F with a smooth profile is driven in the region $r_o < r < a$. The total current $I_t = I_\Omega - I_R + I_F$ is assumed to be fixed.

From Eqs. (1) and (2) we obtain an expression for the value of q on axis in terms of the reverse and forward current fractions. This expression can be written as

$$\frac{I_F}{I_t} + \frac{I_R}{I_t}\left[\frac{a^2}{r_o^2}\frac{\beta + 1}{\alpha + 1} - 1\right] = 1 - \frac{q(a)}{q(o)}\frac{1}{\alpha + 1}. \tag{3}$$

Note that $q_\Omega(o) = q(a)/(\alpha + 1)$ is the q-value on axis in the purely Ohmic case. Expression (3) shows that reverse current drive is only to be preferred when this current is sufficiently localized (small r_o/a) and peaked (large β/α) (conditions that may be difficult to meet by e.g. NBI current drive). In particular, the first term between brackets which multiplies I_R should be ≥ 2. When this quantity is smaller, a pure forward current is advantageous because it minimizes the total non-inductive current that is needed to achieve $q(o) \geq 1$. On the other hand, the ranges in β and r_o/a are limited by the requirement of a smooth q-profile with $q \geq q(o) \geq 1$. A necessary condition for this is $q''(o) \geq 0$,

$$1 - \frac{I_F}{I_t} + \left[1 - \frac{\beta(\beta + 1)}{\alpha(\alpha + 1)}\frac{a^4}{r_o^4}\right]\frac{I_R}{I_t} \geq 0. \tag{4}$$

Expressions (3) for $q(o) = 1$ and (4) for $q''(o) = 0$ are represented in the (I_R, I_F) diagram of Fig. 1a for $q(a) = 3$, $\alpha = 4.5$, $\beta = 2$ and

$r_o/a = 0.5$. The currents to be driven have to be in the shadowed region in order to have $q(o) \geq 1$ and $q''(o) \geq 0$.
At the point of intersection of the two curves we find

$$\frac{I_R}{I_t} = q(a) \quad \frac{r_o^2/a^2}{\beta + 1} \quad \frac{1}{\frac{\beta}{\alpha}\frac{a^2}{r_o^2} - 1} \tag{5a}$$

and

$$\frac{I_F}{I_T} = 1 + \frac{q(a)}{\alpha + 1} \quad \frac{\frac{r_o^2}{a^2}\frac{\alpha+1}{\beta+1}}{\frac{\beta}{\alpha}\frac{a^2}{r_o^2} - 1} \left(1 - \frac{\beta(\beta+1)}{\alpha(\alpha+1)}\frac{a^4}{r_o^4}\right). \tag{5b}$$

When $(\beta/\alpha)\, a^2/r_o^2$ is sufficiently large, the intersection of the curves lies in the quadrant shown in Fig. 1a. This means that under these circumstances, it is not sufficient to drive only a reverse current in the centre, but that also a forward current has to be driven off-axis. At the point of intersection, the total current $I_R + I_F$ to be driven has an extremum. When $(a^2/r_o^2)(\beta + 1)/(\alpha + 1) > 2$, this extremum is a minimum which can be minimized further with respect to the profile constants β and r_o/a of the reverse current. Figure (1b) shows the optimum value of β as a function of r_o^2/a^2 for $\alpha = 3$ and 4.5. This β^{opt} is independent of $q(a)$. The corresponding values of $I_F/I_t + I_R/I_t$ and the current fractions I_F/I_t and I_R/I_t are shown in Fig. 1c for $q(a) = 3$ and $\alpha = 4.5$. Smooth q-profiles are obtained for the parameters of Fig. 1c and the minimum total current to be driven non-inductively is $0.31\, I_t$.
The latter figure shows that there is only a small region in parameter space where the current has to be driven mainly in the reverse direction. This means that although Eq. (3) indicates that for $(a^2/r_o^2)(\beta + 1)/(\alpha + 1) > 2$ reverse current drive is most effective, the condition $q''(o) > 0$ requires a substantial forward current.

MODIFICATION OF THE CURRENT DENSITY PROFILE AROUND q=1

We consider a situation in which a localized non-inductive current is driven, consisting of either a reverse or a forward component, or both. For the profile shape we assume

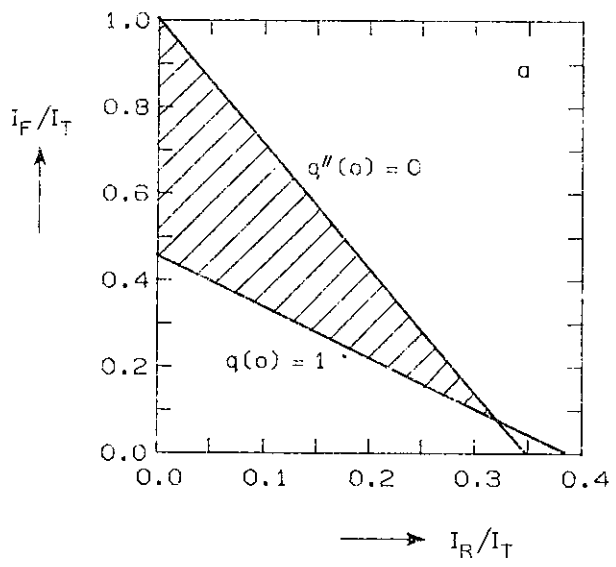

Fig. 1a:

Area in I_F/I_T, I_R/I_T where both $q(o) > 1$ and $q''(o) > 0$, for $q(a) = 3$, $\alpha = 4.5$, $\beta = 2$ and $r_o/a = 0.5$.

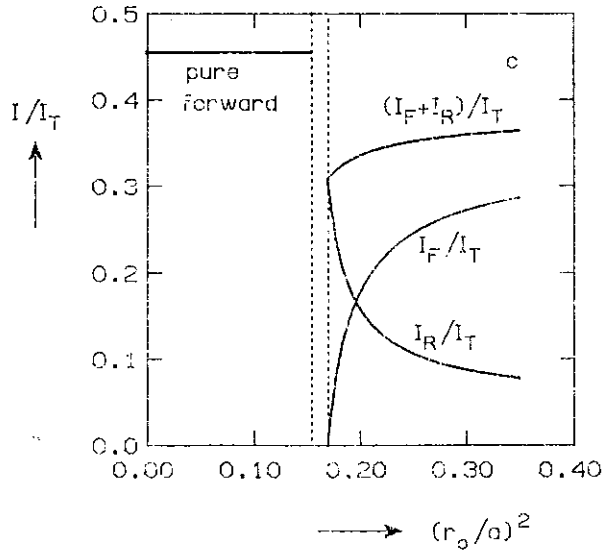

Fig. 1b:

Optimum β $(\alpha, r_o/a)$ for a combination of reverse and forward current drive.

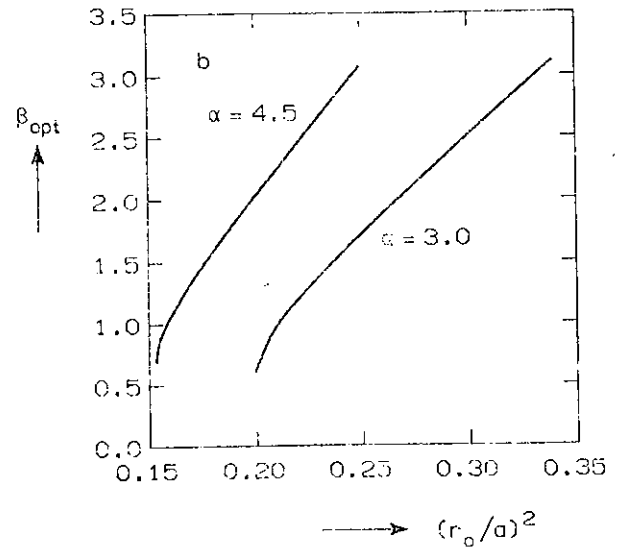

Fig. 1c:

Variation of I_R, I_F and $I_R + I_F$ along the line of optimum β-values. Case with $\alpha = 4.5$, $q(a) = 3.0$.
The left dotted line indicates where $\beta_{opt} + 1 = 2(\alpha+1)r_o^2/a^2$, i.e. the lower end of the curve in Fig. 1b.

$$j(r) = 0 \qquad \text{for } r_m - \Delta > r > r_m + \Delta,$$
$$j(r) = \left[1 - \left(\frac{r - r_m}{\Delta}\right)^2\right]^2 \qquad \text{for } r_m - \Delta \leq r \leq r_m + \Delta. \tag{6}$$

We have studied the possibility to modify the shear at the q=1 surface with such a non-inductive current distribution.

As a first example a pure forward current with $I_F/I_t = 0.2$ and a variable r_m and Δ was superimposed on a discharge with an Ohmic current distribution as given by Eq. (1), with $q(a) = 3$ and $\alpha = 4.5$. Figures 2a,b show examples of the resulting q-profiles. Obviously the profile parameters Δ and r_m must be chosen such that Δ is not too large and r_m is just inside the q=1 surface. For r_m too large or too small the only result is a shift of the q=1 surface to smaller or larger values of r. There is only a small window in r_m-values where the gradient at the q=1 surface is affected, with a sharp optimum. An enlargement of Δ relaxes the required precision in r_m, but reduces the overall effect.

Figure 3 shows some examples for a reverse current with $I_R/I_t = 0.2$. In this case the effect on the gradient can either be neglected or an enlarged shear is obtained. This enhancement is due to the increase of the Ohmic current.

A combination of reverse and forward current drive, with $I_F/I_t = I_R/I_t = 0.1$ does not change the ohmic current and thus only modifies the q-profile in the region where the non-inductive current flows. Figure 4 shows some examples for adjacent profiles, i.e., $(r_m + \Delta)_R = (r_m - \Delta)_F$. This combination of reverse and forward current drive again relaxes the requirement of precize localization with respect to the q=1 surface without reducing the overall effect.

From these calculations for peaked Ohmic current profiles it can be concluded that localized non-inductive current drive with approximately 20% of the total current can serve as a tool to modify the shear at the q=1 surface. A combination of reverse and forward current drive with its turning point just within the q=1 surface is best suited for this purpose.

EC current drive can produce the desired combination of reverse and forward currents. This could give the possibility to manipulate sawtooth phenomena and to test the various instability models.

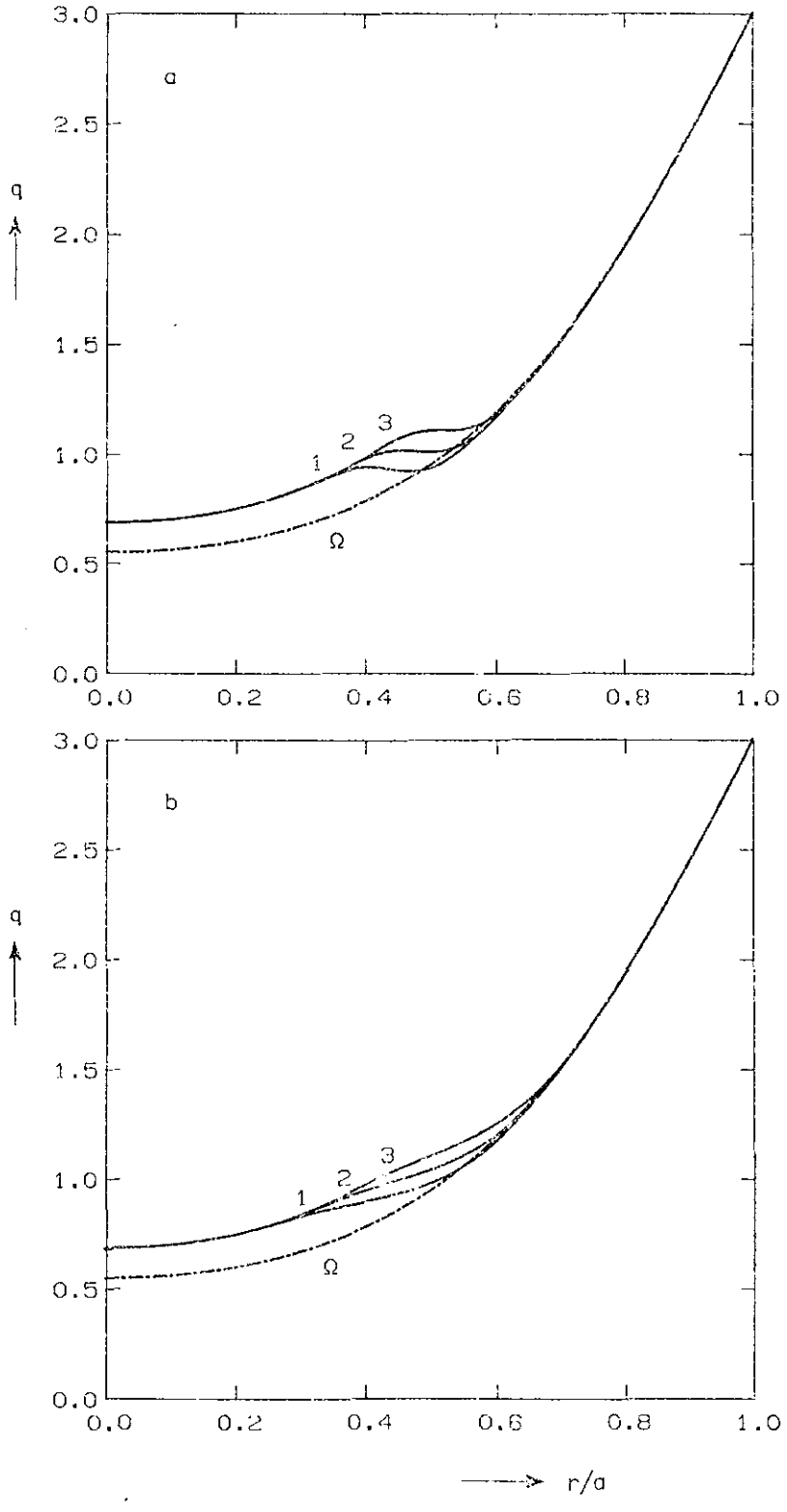

Fig. 2a,b: Modification of the q-profile around q = 1 surface. Case with q(a) = 3.0, α = 4.5, I_P/I_T = 0.2, Ω is Ohmic profile.
a) Δ = 0.1a, 1) r_m = 0.45a, 2) r_m = 0.49a, 3) r_m = 0.53a;
b) Δ = 0.2a, 1) r_m = 0.425a, 2) r_m = 0.475a, 3) r_m = 0.525a.

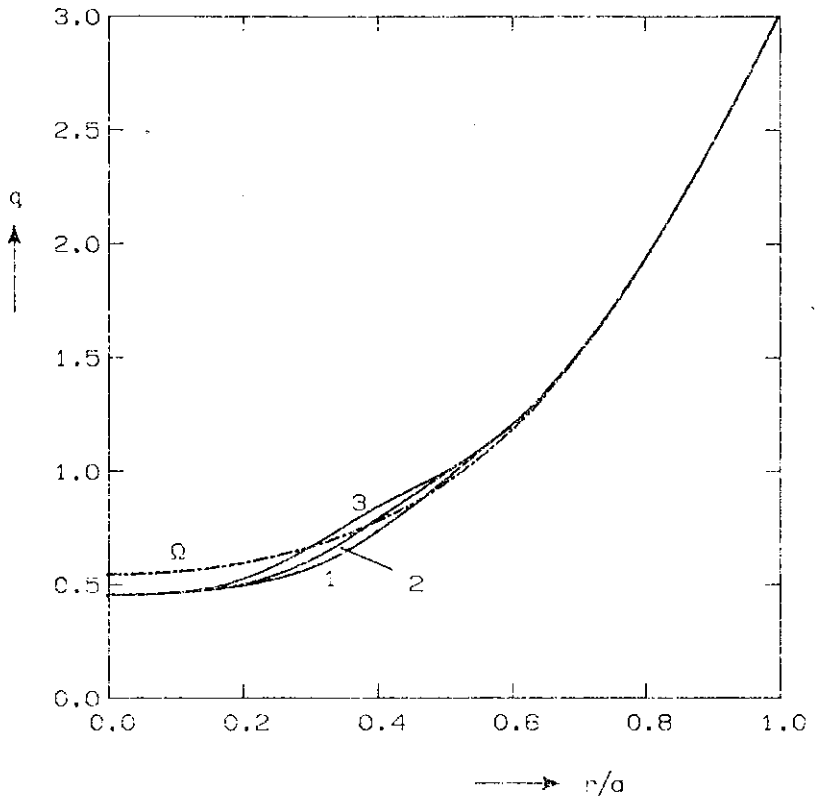

Fig. 3: Modification of the q-profile around the q = 1 surface. Case with q(a) = 3.0, α = 4.5, I_R/I_T = 0.2, Δ = 0.1a, Ω is Ohmic profile.

1) r_m = 0.5a,
2) r_m = 0.4a,
3) r_m = 0.3a.

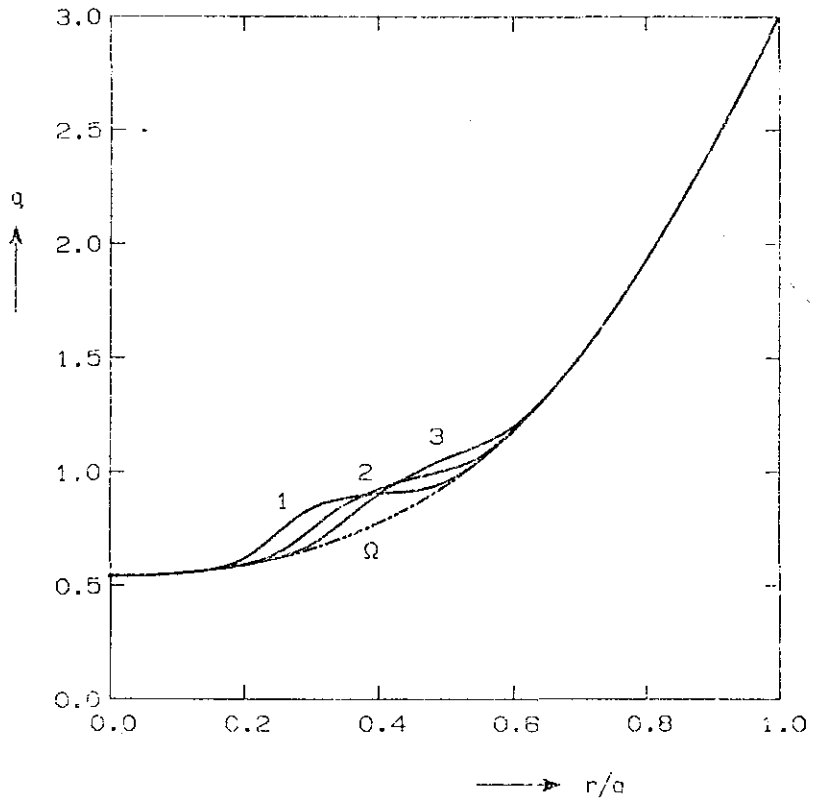

Fig. 4: Modification of the q-profile around the q = 1 surface. Case with q(a) = 3.0, α = 4.5, I_F/I_T = 0.1, I_R/I_T = 0.1, Δ = 0.1a, Ω is Ohmic profile.

1) $r_{m,R}$ = 0.25a, $r_{m,F}$ = 0.45a;
2) $r_{m,R}$ = 0.3a, $r_{m,F}$ = 0.5a,
3) $r_{m,R}$ = 0.35a, $r_{m,F}$ = 0.55a.

DISCUSSION

The results presented are all obtained for Ohmic current profiles with $q_\Omega(o)$ substantially below 1. Consequently, the non-inductive currents required for achieving a monotonous q-profile with $q(o) > 1$, are quite large. The amount of current needed to modify only the shear at the $q = 1$ surface is considerably less. Lower values of α, i.e. broader current profiles (1), will relax these requirements.

A modification of the profile shape by introducing a pedestal value at the plasma edge, introduces only slight changes in the previous results. However, such a pedestal could lead to widely different Δ'-stable current profiles [3]. In this context it should be noted that, in order to minimize anomalous losses, the non-inductive current should not tend to drive the current profile outside its latitude of Δ'-stability. The good localization of EC driven currents could be very useful, even with a modest level of EC power, in shaping a current profile which is consistent with stability against tearing modes. However, a study of these effects is beyond the simply straightforward calculations presented here.

Non-monotonous profiles with $q(o) > 1$ and with negligible shear at the off-axis $q = 1$ surface, profiles invoked in an ideal MHD model for sawtooth phenomena [4], can be modified with a modest amount of localized EC current near the $q = 1$ surface. This could provide a tool to test the sawtooth model of Ref. [4].

ACKNOWLEDGEMENTS

This work was performed under the Euratom-FOM association agreement with financial support from ZWO and Euratom.

REFERENCES

[1] H. Hammin, J. Wesson, JET International Report (1985).

[2] G. Briffod, EUR-CEA-F C1286 (1985).

[3] H.P. Furth, Plasma Phys. and Contr. Fusion 28 (1986) 1305.
N. Ohyabu, J.K. Lee, J.S. de Grassie, Nucl. Fusion 26 (1986) 593.

[4] J.A. Wesson, Plasma Phys. and Contr. Fusion 28 (1986) 243.

IV Transmission Line System and Antenna Structure for EC Power Injection into JET, I.R. 86/019.

TRANSMISSION LINE SYSTEM AND ANTENNA STRUCTURE FOR EC POWER INJECTION INTO JET

C.A.J. van der Geer, P. Manintveld, T.J. Schep
Association Euratom-FOM, FOM-Instituut voor Plasmafysica
Rijnhuizen, Nieuwegein, The Netherlands

L. Rebuffi
Association Euratom-CEA sur la Fusion
Département de Récherches sur la Fusion Contrôlée
Centre d'Etudes Nucleaires
CEA BP no 6, 92260 Fontenay-aux-Roses (France)

ABSTRACT

The transmission line system and antenna structure for the injection of electron cyclotron wave power through a vertical port into JET is considered.

The composition of a 70 GHz, 200 kW system and the microwave properties of the separate components are discussed.

Attention is paid to the antenna structure and solutions are suggested to the problems set by the required angles of injection and by the polarization of the radiated waves.

1. INTRODUCTION

The injection of electron cyclotron wave power through a vertical port into the JET device is under investigation. The injected waves have a frequency well below the local cyclotron frequency and have to be coupled to the extraordinary mode in the plasma. From the point of view of current drive and supra-thermal generation, this launching scheme has a number of favourable features. On the other hand, quite complicated requirements are imposed on the antenna pattern of the launching structure.

Ray tracing calculations [1] show that good absorption in the tail of the electron velocity distribution function occurs at a 70 GHz wave frequency. At lower frequencies the absorption decreases substantially, while at higher frequencies the power is absorbed at lower particle energies. For this reason, the transmission line and antenna structure for a wave frequency of 70 GHz will be discussed. A great advantage is the availability of 70 GHz gyrotrons.

Commercially available quasi-CW 200 kW, 70 GHz gyrotrons deliver their power mainly in the circular TE_{02} waveguide mode [2]. The oversized output port has a diameter of 63.5 mm.

Typically 5% of the power is in other TE_{on} modes. The phase relation between these modes is fixed and, in principle, the whole mode mixture could be converted into a single mode [3]. However, the power recovered this way might not be worth the cost of the extra mode converters and phase shifters that would be needed.

The transmission line should transport the power from the gyrotron to the launcher with high efficiency and mode purity. The mode at the input is set by the gyrotron, the required mode at the output is set by the launcher. Since the total length of a transmission line will be 50 to 55 m., the TE_{02} has to be converted to the TE_{01} mode which has low Ohmic losses in a circular waveguide.

Because the field patterns of the TE_{11} and HE_{11} modes resemble most the one of a plane wave, we will discuss several possibilities to construct the required antenna pattern from these basic modes. Hence, at least two mode converters are needed between the gyrotron and the antenna. The composition of a transmission line and the microwave properties of the constituting parts will be discussed in Section 2.

The waves radiated from the launcher have to be coupled to the extraordinary mode in the plasma. A good coupling requires that the launched wave is elliptically polarized. In addition, the wave has to be injected under a certain angle with respect to the toroidal field in order to obtain a well-defined localization of the power absorption. Several possibilities to achieve the required polarization and angles of injection are discussed in Section 3.

2. TRANSMISSION LINE

General

The HF power that can be transmitted through a transmission line is proportional to the square of the waveguide diameter, while the resistive loss in a line scales with the inverse cubic power of the diameter. In addition, in the oversized multimode system under consideration, the lengths of the mode selective directional couplers, mode converters, and bends are determined by the differences in phase velocities between the propagating modes and therefore scale with the square of the diameter. Hence, a compromise has to be found between the demand for low Ohmic losses, high power carrying capacity of the line and space requirements. The latter impose strong restrictions on the dimensions of the system, in particular because the layout as discussed by Verhoeven et al., [2] contains six bends. The power carrying capacity is largest for a pure mode. Generally, a mode mixture has voltage maxima along the line so that arcing occurs at lower power levels.

The transmission line should include diagnostic components like couplers and frequency meters to monitor the behaviour of the source. All electronic circuitry, sensitive to interference, should be placed in a screened cage.

A possible scheme of a suitable transmission line composition is shown in Fig. 1. In the following, the components of this transmission system are discussed starting from the gyrotron side.

Arc detector

Any arc should be detected and the gyrotron switched off within a few microseconds to protect the gyrotron, in particular its window.

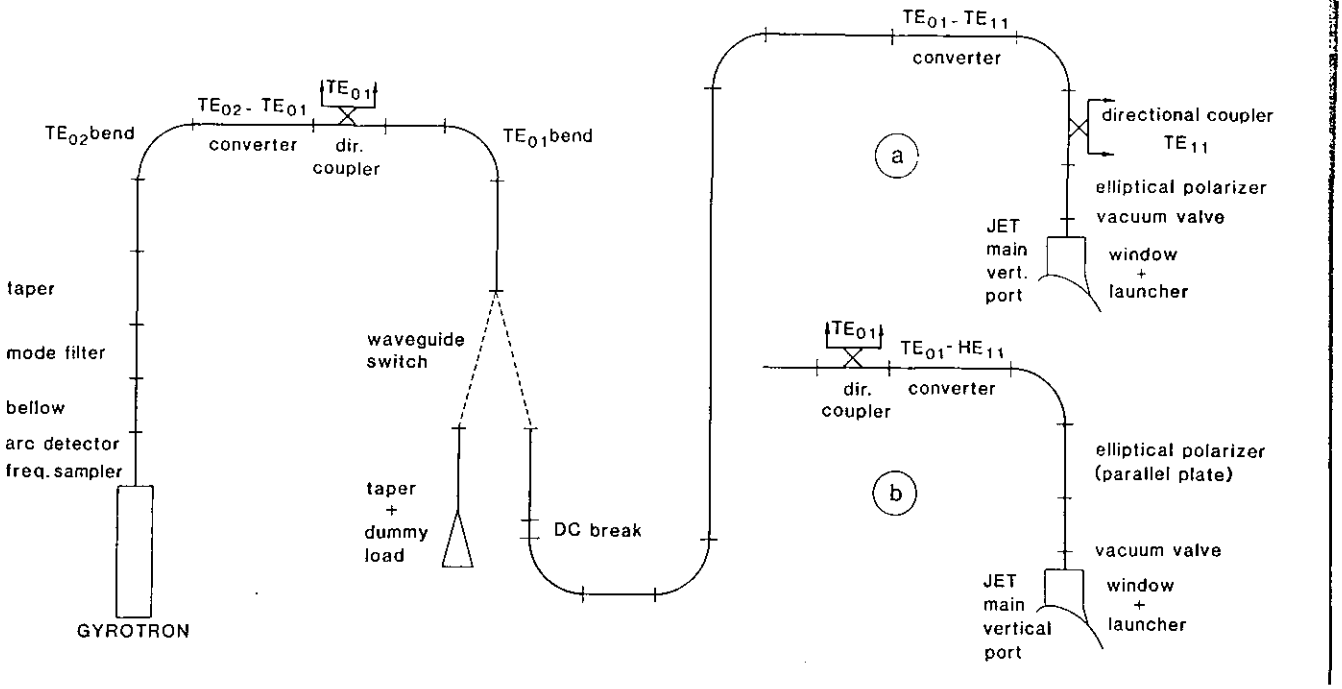

Fig. 1. Transmission line with A launching of TE_{11} mode,
B launching of HE_{11} mode.

Since an arc runs towards the generator, the arc detector is mounted on top of the gyrotron. The same protection is needed for the window at the torus side and for critical parts in the waveguide system, like bends. In order to reduce the damage caused by arcs, the inner surface of a bend is often goldplated. On TFR, arcs occurred in the 27.8 mm, TE_{01} bends when the power level was raised above 220 kW. The level depended on the mode purity. Arcing is further reduced by mode filters placed between bends absorbing the spurious modes that are generated.

An arc detector is a piece of waveguide with a small hole in the wall, behind which a photodiode is mounted. This diode detects the light radiated by an arc in the waveguide. The photodiode's signal is used to switch off the gyrotron. The design used in the ECRH experiment on TFR utilizes light guides to transport the light to a screened cage for detection. The system is checked by injection of a lightpulse into the arc detector via a second hole.

Frequency sampler

A small part of the microwave power is coupled into a standard fundamental waveguide via a third hole in the arc detector. This

signal is sent to a wavemeter and a radiometer [4] to measure the frequency spectrum, which is used for the tuning of the gyrotron.

Bellow

In order to avoid mechanical stress, a bellow is placed close to the gyrotron. Commercial available stainless steel bellows are applied. Since a bellow acts as a TE_{on} pass filter, it should be placed in a section where the power is mainly in an axisymmetric TE-mode. As observed in the ECRH experiment on TFR, a deformation of the bellow can be the cause of mode conversion and arcing.

Mode filters

To maximize the power level above which arcing occurs, all modes from the gyrotron other than TE_{02} have to be filtered out. The filter attenuates also reflected spurious modes, which improves the stability of the signal generated by the gyrotron.
A resistive wall filter can be built very compactly. However, the large temperature increase of the resistive material during the pulse can be the cause of arcing in the narrow parts of the transmission line, possibly as a result of outgassing. In the ECRH experiment on TFR a 0.6 m long carbon wall filter has been applied successfully. The temperature rise would be less in a mode filter consisting of a waveguide with a corrugated wall. Such a filter, which has still to be developed, dissipates the power in a larger volume and has a lower loss for the TE_{01} and the TE_{02} modes.
A filter has to be cooled when long pulses are applied.

Taper, first bend, mode converter, directional coupler

A transmission line diameter equal to that of the gyrotron output port, 63.5 mm, would result in large bend radii, long directional couplers and long mode converters. Therefore, it is necessary to taper down to a smaller diameter. This diameter is chosen as a compromise between reduced dimensions and higher Ohmic loss. With non-linear tapering from 63.5 to 30 mm, conversion losses in a taper of 1 m length can be kept below - 50 dB at 70 GHz.
A bend for an axisymmetric mode has a circular cross-section and a corrugated wall. The corrugation removes the degeneracy of the TE_{on} and TM_{1n} modes. The geometry of the bend and the corrugations have to be optimized with respect to mode conversion losses. This results in different designs for different modes. The TE_{02} and TE_{01} modes can be

very efficiently converted into each other by a periodic modulation of the waveguide diameter.

A directional coupler (TE_{02} or TE_{01}) should be included in the line, in order to obtain information about the level of the incident and reflected power. The gyrotron is switched off when the latter signal exceeds a preset value.

The specific order of these components depends dominantly on the available space.

K-spectrometer, gyro-radiometer

A K-spectrometer [5] and a spectrum analyser centred around 70 GHz [4] are desirable for initial set up and for optimal tuning of the gyrotron. These two devices will permit a complete calibration of the system (mode detection, power calibration, optimal working point, detection of a mismatch in the line). They have to be placed in the narrow part of the line. One set can be used for all lines.

Waveguide switch and dummy load

The subsequent part of the line consists of straight (smooth wall) circular waveguide sections and corrugated bends. Somewhere in this part (inside the gyrotron hall), a waveguide switch has to be installed which selects either the experiment or a dummy load as a target. This switch has to be developed.

The dummy loads used in the ECRH experiment on TFR (Varian type VLE 8006 A9) are particularly suited for axisymmetric modes. They require 4 l/s cooling water. The microwave power is dissipated in a very thin layer of water. At a lower flow the water will start boiling. This can destroy the load and gives rise to power reflection which could damage the gyrotron. This load is not suited for the TE_{11} mode at 0.1 sec pulses of full power.

Such a load can be improved by taking octanol as an absorber [6]. Then, due to the lower loss tangent of octanol, the power penetrates further into the fluid, warming up a larger volume so that boiling is less likely to occur. This load is suited also for non-axisymmetric modes.

A completely different design, essentially consisting of a long section of high loss waveguide coiled up to a helix, is under construction at the FOM-Institute for Plasmafysica at Nieuwegein and will be tested in 1987.

Straight section, total loss

In the straight sections, the power loss is due to the resistivity of the wall. Surface roughness and anomalous skin effect cause this loss to be a factor 1.5 to 2 larger than the theoretical value. Silverplating can reduce this factor to 1.2 to 1.5. The losses in other components (bends, converters etc.) consist mainly of Ohmic losses and of losses due to conversion to unwanted modes.

The total losses for the various components of the line are listed below. The minimum and maximum losses are given as a percentage of the input power for each component.

	min.	max.
Bellows	-	1%
2 tapers	-	- negligible
TE_{02} corrugated bend	1%	1.5%
TE_{02}-TE_{01} converter	0.3	2%
mode filter	-	2%
straight sections 30 m, 30 mm, TE_{01}	6	8%
5 TE_{01} bends	7.5	10%
TE_{01}-TE_{11} converter	2.5	4%
2 DC breaks	-	2%
window	-	2%
total max = 1 - 0.99 × 0.985 etc.		28.5%

This listing is a compilation of measured data for various systems (PDX, COMPASS, W-VIIA, W-VIIAS, TFR). An anomaly factor of 2 is taken for the resistive losses in the straight sections.

It can be seen that it will be difficult to obtain an efficiency of more than 75%. A direct approach to improve the efficiency is to minimize the length of the transmission line and to decrease the number of bends. For JET this would mean the routing of the transmission lines through thick concrete walls. Increasing the waveguide diameter from 30 mm to about 60 mm will decrease the Ohmic loss of the TE_{01} mode to less than 1% (third power scaling). Components like mode converters and directional couplers may become of unacceptable length. To reduce the losses caused by water vapour in the waveguide, the line should be cleaned regularly with a flow of dry nitrogen. In the ECRH experiment on TFR, there was no flow during the pulse.

DC breaks and grounding

JET requires an electrical isolation between torus and transmission line. This can be accomplished by a so-called "DC-break" or "-block". Hold-off voltage and maximum capacitance are to be specified by JET. Basically a break consists of a piece of dielectric waveguide or a sheet of dielectric material between two flanges. Breaks that are based on this principle are successfully applied in TE_{01} and TE_{02} as well as in HE_{11} waveguides. A small fraction of the power escapes from the waveguide via the break. This fraction has to be absorbed for personnel safety and to prevent interference. The break has to be cooled when long pulses are applied. When the gyrotron, or its power supply, and the transmission line have different grounding points, a second DC break should be installed.

Mode converter $TE_{01} \rightarrow TE_{11}$ or HE_{11}

Because of their simple wave patterns, which are rather close to that of a plane wave, the TE_{11} and HE_{11} modes seem to be most suitable for injection into the plasma. A periodically bend (wiggled) waveguide converts the TE_{01} mode into the TE_{11} mode [3]. The TM_{11} mode is obtained from the TE_{01} mode by a simple bend with a specific angle between input and output ports [7,8]. Both modes are converted into the HE_{11} mode by employing a waveguide with a gradually changing corrugation depth [8].

The radiation pattern of the TE_{11} mode has the following characteristics with respect to the pattern of the HE_{11} mode:

- The power density on axis is 0.8 dB higher.
- The beamwidth in the E-plane is narrower but sidelobes are 10 dB higher.

The E-field pattern of the TE_{11} mode far away from the waveguide aperture is shown in Fig. 2. The left-hand side shows the angular dependence of the power density in the E-plane and the right-hand side the one in the H-plane. Almost 100% of the power is transmitted through a surface determined by the first angle where the power density is zero [9].

In contrast to the TE_{11} mode, the HE_{11} mode is an eigenmode of a corrugated waveguide. It can be considered as a composition of about 85% TE_{11} and 15% TM_{11}. All line components carrying the HE_{11} mode have

to be corrugated. This is a disadvantage. Smooth wall components like windows and directional couplers will distort the mode. On the other hand, HE_{11} bends can be made with smaller bend radii than TE_{11} bends. Losses, production costs and ruggedness should also be compared, for the final choice between the TE_{11} and HE_{11} mode.

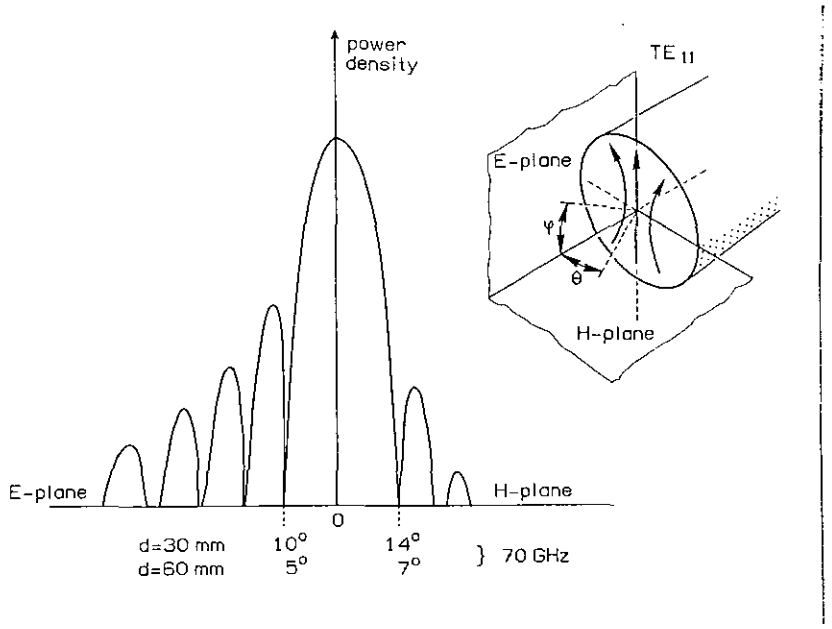

Fig. 2. Far field of TE_{11} mode radiated from circular waveguide.

Window

With regard to the power carrying capacity, the vacuum windows (at the vacuum vessel and at the gyrotron) appear to be the critical components. They consist of one or two discs of dielectric material (aluminium oxide, beryllium oxide, quartz). Quartz has the lowest dissipation for microwave signals but is the most difficult to braze to metals, while the higher loss materials require large diameter discs (3-4 inches) and liquid cooling to keep mechanical stress sufficiently low. A promising compact design will be installed in COMPASS and DITE (see Fig. 3). There, a quartz disc and gas cooling is applied.

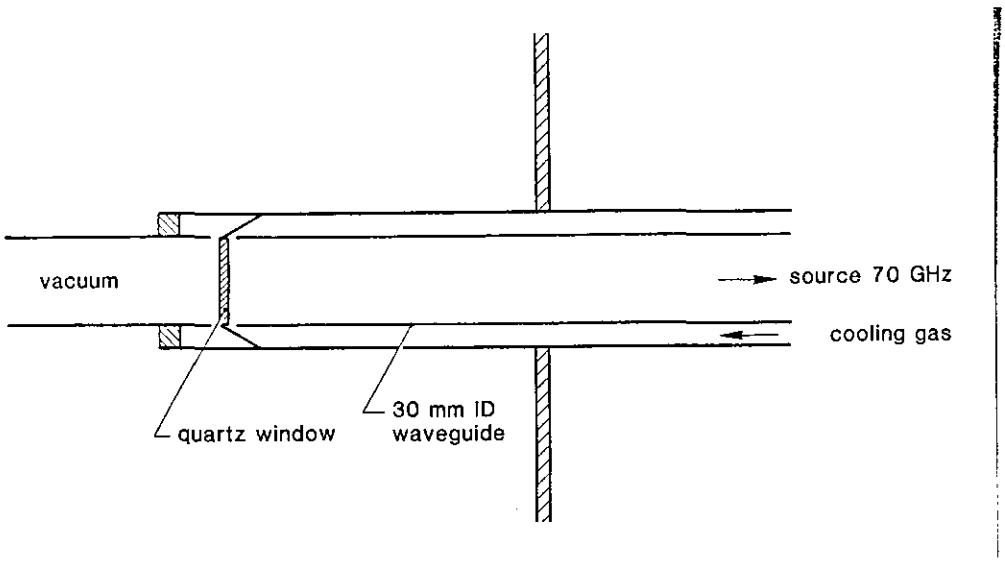

Fig. 3. Window design for COMPASS and DITE.

3. LAUNCHER

The direction of the injected waves is specified by the angles ϕ and θ, which are spherical coordinate angles with respect to a local Cartesian system (x, y, z) at the launching position. The z-axis of this system is parallel to the axis of symmetry of the torus, the x-axis is in the direction of the major radius and the y-axis is in the toroidal direction (see Fig. 4). Hence, θ is the angle between the ray and the vertical direction, and ϕ is the angle between the projection of the ray on the equatorial plane and the major radius.
These injection angles have to lie in a specific range. Numerical ray tracing calculations [1] indicate that good absorption in the far tail of the electron velocity distribution occurs for injection angles ϕ = -70° to -90° and θ = 145° to 175°. For the transmission line this means that the microwave beam from a vertical waveguide has to be deflected over 0° to 20° with respect to the toroidal direction and 15° to 35° with respect to the axis of the port.
In the table below, the values of the parallel index of refraction as obtained from ray tracing calculations are presented.

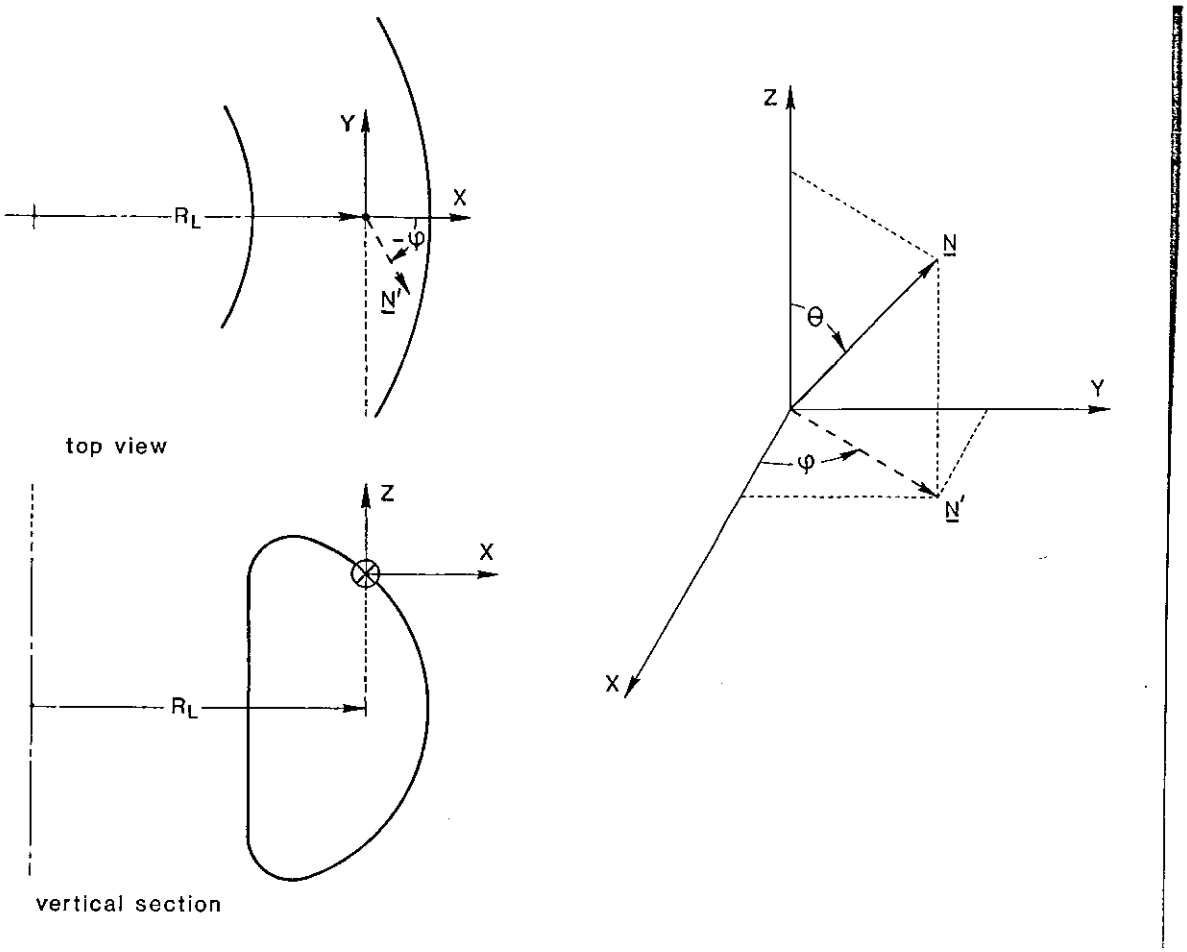

Fig. 4. Coordinate system for ray tracing.

θ \ ϕ	-70°	-80°	-90°
145°	0.60	0.60	0.60
155°	0.45	0.45	0.45
165°	0.30	0.30	0.30

Ray tracing calculations show that the power deposition depends less strongly on the angle ϕ than on the angle θ [1].

At the periphery of the plasma, the radiated field has to match the electromagnetic field of the X-mode in the plasma. Since the distance between the antenna and the plasma boundary is rather short,

this matching has to occur in the Fresnel zone of the antenna. In this regime, free space propagation occurs ($N \equiv k^2c^2/\omega^2 = 1$). The ratios of the components of the wave electric field as obtained from the cold dispersion equation are

$$\frac{iE_1}{E_2} = P \quad , \quad \frac{E_3}{iE_2} = \frac{P}{N_{\parallel}} (1-N_{\parallel}^2)^{1/2} \tag{1}$$

$$P = \frac{f_c}{2f} \left[1 - N_{\parallel}^2 - \{(1-N_{\parallel}^2)^2 + 4 N_{\parallel}^2 \frac{f^2}{f_c^2}\}^{1/2}\right] \quad , \tag{2}$$

where f is the wave frequency and f_c the local cyclotron frequency. The coordinate system is such, that the 3-direction is along the main magnetic field and the propagation vector lies in the 1-3 plane (see Fig. 5). The component $N_{\parallel}$ of the refractive index N along the equilibrium magnetic field B is:

$$N_{\parallel} = \underline{N} \cdot \frac{\underline{B}}{B} = \frac{B_T}{B} \underline{N} \cdot \underline{e}_y + \frac{B_P}{B} \underline{N} \cdot \underline{e}_P \quad ,$$

where B_T, B_P are the toroidal and poloidal components of the magnetic field, respectively, and $\underline{e}_P$ is the unit vector in the poloidal direction.

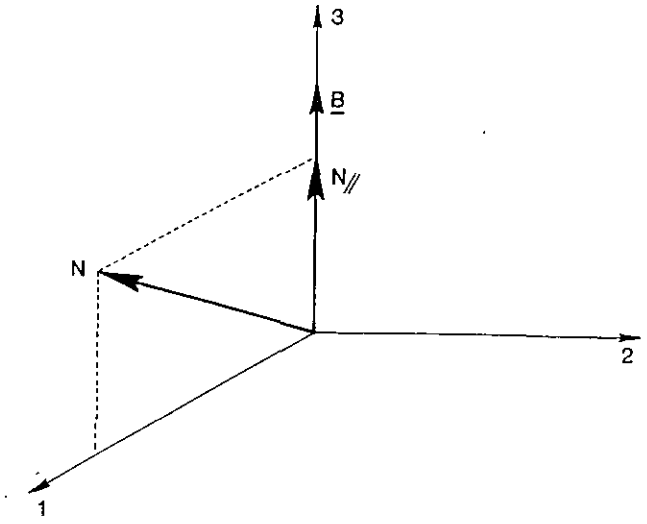

Fig. 5. Coordinate system used in (1) and (2).

The ratios (1) imply that, in order to couple all the wave power into the X-mode, the antenna should radiate an elliptically polarized wave pattern in its Fresnel zone. The importance of this requirement can be illustrated by a simple example.

Consider the situation where a plane wave with frequency $f = 70$ GHz is launched under angles $\theta = 150°$ and $\phi = -90°$. This corresponds to the case where the wave vector lies in the y-z plane (see Fig. 4) with $N_{\parallel} = 0.5$. The local cyclotron resonance frequency is assumed to be $f_c = 90$ GHz. Then, from (2) we find $P = 0.2$. When the electric field vector is along the x-axis, a simple calculation shows that about 85% of the wave power is coupled to the X-mode. The remaining power is coupled to the O-mode. These numbers become more favourable at lower values of $N_{\parallel}$. When the electric field vector lies in the y-z plane, only 15% of the radiated power is coupled to the X-mode.

In the following a number of practical solutions to these problems are discussed.

Elliptical polarization

Four possibilities to obtain the desired polarization are briefly discussed.

1. Generation from TE_{01} mode with two $TE_{01} \rightarrow TE_{11}$ mode converters in series.

   In the first converter only part of the input power is transformed into the TE_{11} mode. In the second, which is rotated over 90°, the remaining power is transformed to the TE_{11}^{r} mode. The superscript indicates that this mode is cross-polarized with respect to the TE_{11} mode from the first converter. The phase shift between the two modes is proportional to the length of the straight section between the two converters. The configuration is illustrated in Fig. 6.

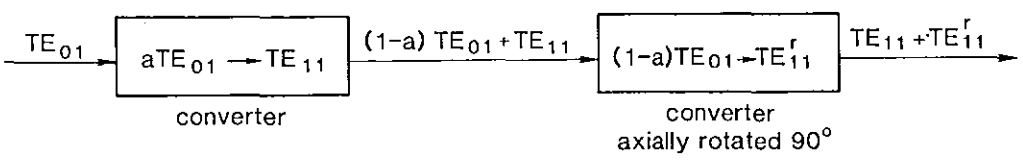

Fig. 6. Elliptical polarization obtained by two TE_{01} - TE_{11} converters.

The drawbacks of this solution are that the degree of ellipticity is fixed and that the total length of the converter system will be at least 3 m. However, the two converters can possibly be combined into a single one. This would reduce the total length.
Figure 7 shows the amplitudes of the modes TE_{11}, TE_{01}, TM_{11} and TE_{12} in a wiggling type mode converter with 30 mm diameter and maximum curvature of 0.27 m^{-1} [10]. The calculated efficiency is 95%. To design a converter with higher efficiency the modes TE_{21} and TM_{21} should be taken into account in the calculation and the phase relation between the modes adjusted by inserting short straight sections between the wiggles [3].

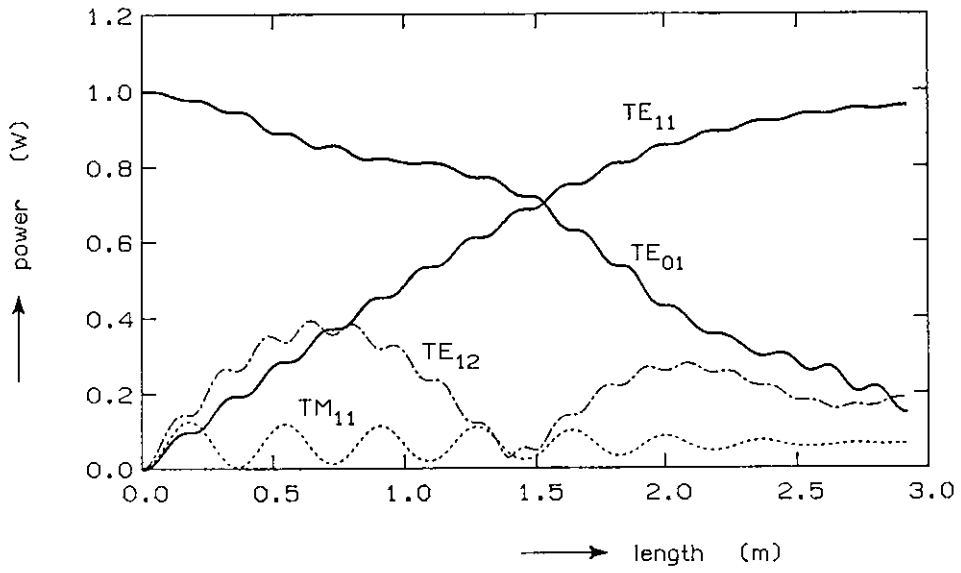

Fig. 7. $TE_{01} \rightarrow TE_{11}$ conversion as a function of converter length.

2. Generation from TE_{11} or TM_{11} modes by an elliptical deformation of the waveguide [11].

Any mode in a circular waveguide can be seen as the sum of two cross-polarized modes with the same phase velocity. An elliptical deformation removes the degeneracy of the two modes, and a phase difference is built up along the elliptical section (Fig. 8).
The small ellipticity should be applied gradually in order not to excite high amplitude m = 3 modes. For the TE_{11} mode, the length of the polarizer is about 0.75 m for a maximum diameter squeeze of 5 mm. For the TM_{11} mode, the squeeze in diameter may be 2.4 times smaller in order to obtain the same phase shift between the two cross-polarized components [12].

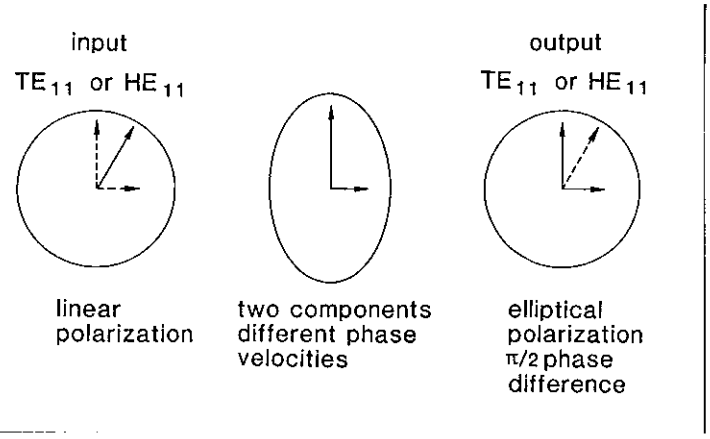

Fig. 8. Elliptical polarization by elliptical waveguide.

3. Elliptical polarization could possibly be obtained with the HE_{11} mode with a set of parallel plate phase shifters (a kind of lens) in front of the waveguide aperture. In this case the phase relation is fixed and the degree of polarization is variable. Expected problems for this system are temperature increase and mechanical construction.

4. Generation from TE_{11} or HE_{11} with a corrugated mirror in the torus.

   This system will be described under "Combined launcher and polarizer".

Angles of Injection

In the following a few possibilities to obtain the required angles of injection are briefly discussed.

Bent waveguide

A simple system consisting of a bent waveguide is depicted in Fig. 9. This system can be constructed very ruggedly, but can only be used in the wider part of a top-port. A bent waveguide with a diameter of 30 mm, a bend radius of 1 m and a bend angle of 25°, converts 6% of the TE_{11} mode to other modes. The converted power is not dissipated in the line, and, thus, changes the radiation pattern at the plasma boundary. When the bend is extended to an angle of 50°, the conver-

sion loss reaches the minimum value of 2%. However, in that case the construction of the support of the connecting waveguide is more complicated. When the HE_{11} mode is applied, smaller bend radii are allowed.

This type of launcher has one degree of freedom. When the angle of the bend is 25° as in the Fig. 9, the launcher can be rotated around the vertical axis so that the angle between the launched beam and the toroidal direction is variable. The angle with respect to the vertical axis is fixed.

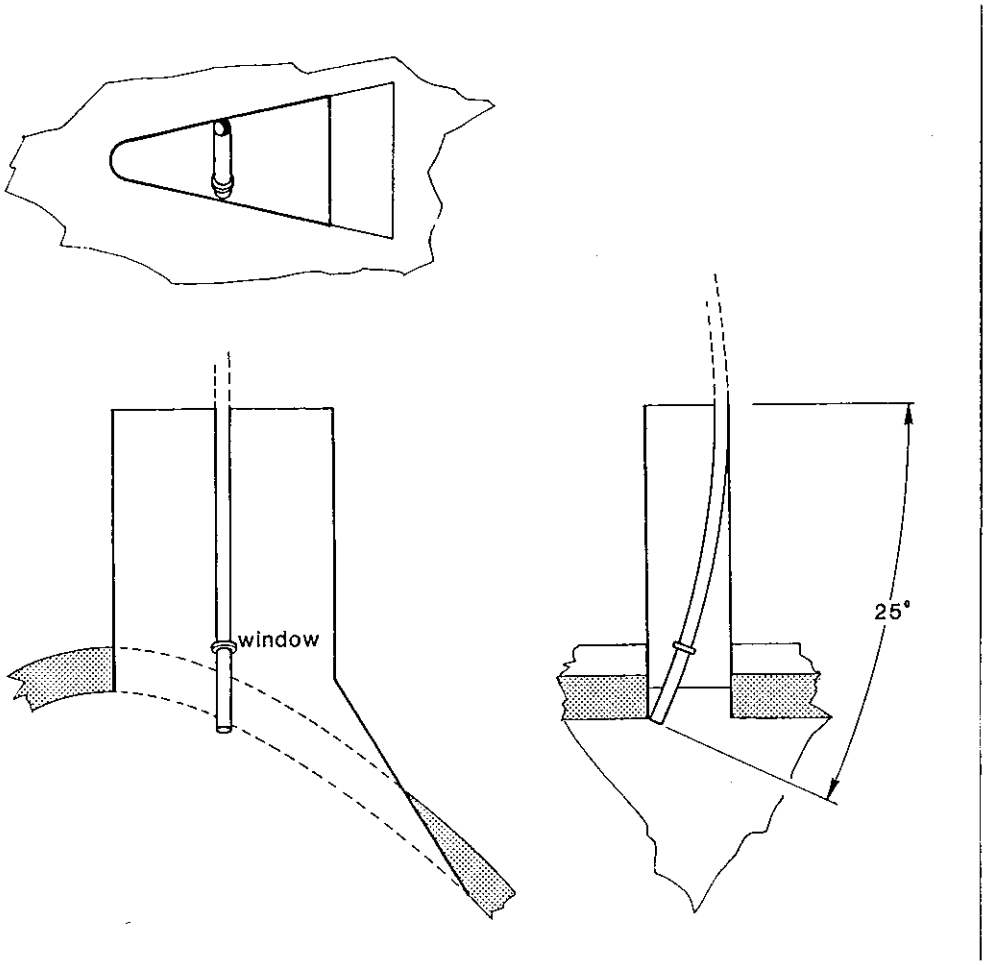

Fig. 9. Launcher with bent waveguide.

Mirror

The obvious way to produce a deflected beam is to put a mirror at the end of the waveguide. However, for the small angles of deflection (< 25°) under consideration, part of the beam will not fall upon the mirror due to the spread in the beam. This undeflected part will suffer diffraction at the reflector edge, and the elliptical polarization of the beam will be seriously distorted. In addition, the angle of incidence becomes so small at the end of the mirror, that depolarization of the signal occurs and power absorption in the mirror surface will be high.

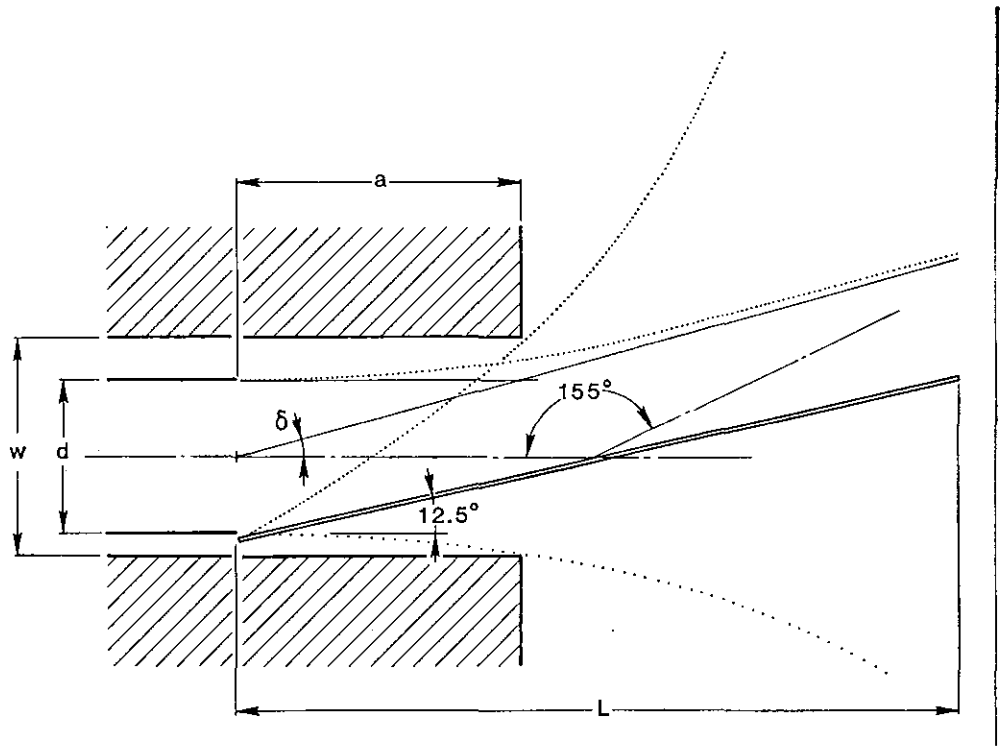

Fig. 10. Plain mirror at the end of a waveguide.

Because of a smaller beam spread, the situation is slightly improved by using a waveguide with a diameter of 60 mm.
A first estimate shows that the mirror should be larger than the normal projection of the waveguide aperture. This means, that L in Fig. 10 is more than 270 mm. Here again, the angle of incidence becomes small, so that depolarization and Ohmic losses can be appreciable.

Depending on dimensions w (60 - 200 mm) and d (minimum 30 mm inside), part of the mirror can be put inside the port. The distance a, has to be such that the deflected beam does not touch the vacuum vessel. First estimates show that only in the widest part of the port the mirror will penetrate less than 40 mm into the vacuum vessel.

An increase of the effective angle of incidence could possibly be obtained by combining a Vlasov antenna [13] with a mirror.

Prism

The required deflection of the beam can be obtained with a metallic plate prism in front of the waveguide aperture. The separation of the plates is between $\lambda/2$ and λ. The incident electric field has to be parallel to the plates. A lens with low reflection, based on this principle, has been successfully tested on TFR.

Combined launcher and polarizer

In the following a scheme is presented in which the elliptical polarization and the direction of injection of the microwave power are obtained with a set of two mirrors. This scheme is illustrated in Fig. 11, where linearly polarized beams emitted by waveguides carrying either the TE_{11} or the HE_{11} mode, are collected on an elliptical mirror. This mirror conserves the linear polarization. The foci of this mirror are placed at the center of the system of waveguide apertures and at the center of a polarizer. This polarizer is a grooved, flat plate. The orientation of the grooves with respect to the incident beam, and the depth of the grooves determines the polarization of the reflected beam. The width of the corrugation should be about $\lambda/3$ and the period $2\lambda/3$.

The angles θ and ϕ between the reflected beam and the vertical axis and the toroidal direction respectively, can be chosen by rotations of the grooved plate in the poloidal and equatorial planes. This scheme offers the advantage of a single polarizer/launcher for each port instead of one for each waveguide.

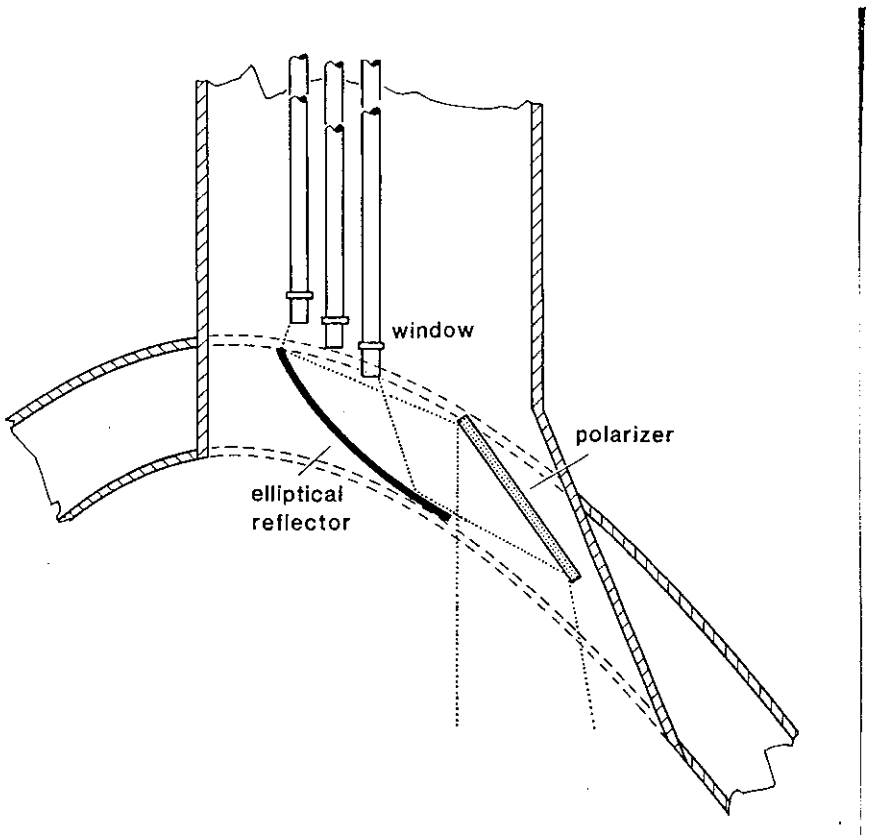

Fig. 11. Combined launcher-polarizer.

A simplified explanation of the working principle of this type of polarizer is the following. Consider a linearly polarized wave that reflects from the corrugated structure. The incident and reflected wave vectors lie in a plane perpendicular to the corrugations and the electric field of the incident wave makes an angle α with this plane, Fig. 12. Since the width w of the corrugations is smaller than $\lambda/2$, the component of the incident electric field parallel to the corrugations, $E_{||}$, is cut-off and reflected on the top of the structure. The perpendicular component, $E_{\perp}$, can propagate inside the corrugations, is reflected at the bottom, and, after travelling twice the corrugation depth d, leaves the structure with a relative phase $4\pi d/\lambda$. The polarization of the reflected wave, specified by the complex ratio $E_{\perp}/E_{||}$, is determined by the angle α and by the corrugation depth d.

In a more detailed analysis, the corrugations are approximated by a continuous, non-isotropic material having zero impedance parallel to the corrugations and imaginary impedance perpendicular to the corrugations [14]:

$$Z = \frac{-iw}{p} Z_o \operatorname{tg} k_o d \tag{3}$$

where w is the width, d the depth and p the period of the corrugations, and k_o and Z_o are the wave number and impedance in free space, respectively. In this model, the ratio $E_\perp / E_\parallel$ is found to be

$$\frac{E_\perp}{E_\parallel} = \frac{k_1 - k_o^2 Z}{k_1 + k_o^2 Z} \cos \alpha, \tag{4}$$

where k_1 is the component of the incident wave vector perpendicular to the corrugated mirror. Equation (4) specifies the polarization in terms of the angle α and the surface impedance Z. The phase shift between $E_\perp$ and $E_\parallel$ is determined by Z, and, hence, by the geometry of the corrugations. A phase shift of $\pi/2$ is obtained when w, p and d are chosen such that $Z = i\, k_1/k_o^2$.

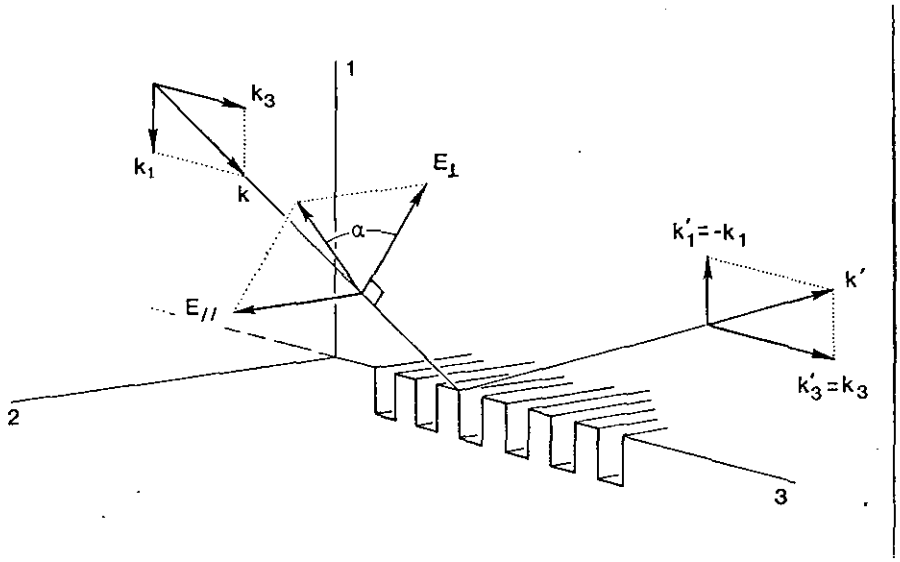

Fig. 12. Reflection on a corrugated mirror.

4. CONCLUSIONS

The transmission line system for transport of RF power from a 200 kW, 70 GHz gyrotron to a top-port of the JET device is discussed. A large part of this over-moded system, which contains a.o. six bends and at least two mode converters, can in principle be built from "conventional" designs. Further experimental and technical research is needed to improve the overall efficiency. In particular, attention should be focussed on the reduction of mode conversion in bends, on ohmic losses in the straight sections (silverplating), and on mode filtering.

More fundamental problems from the point of view of microwave engineering and of wave-plasma coupling, are related with the launching system at the end of the transmission line. This system should launch a narrow wave beam under a variable angle into the device. In addition, the beam has to be elliptical polarized in order to match the extraordinary plasma mode in the Fresnel zone of the antenna.

Possible solutions to elements of these problems are presented. More extensive experimental and numerical studies are required in order to achieve a system which establishes a satisfactory coupling of the RF power to the plasma.

Acknowledgement

This work was performed under JET Article 14 Contract no. JJ5/9007 and under Euratom-FOM Association agreement with financial support from ZWO and Euratom.

REFERENCES

[1] R.W. Polman, T.J. Schep, E. Westerhof, L. Klieb, "Electron cyclotron current drive and supra-thermal generation in JET", Internal Report 86-021 (1986).

[2] A.G.A. Verhoeven, P. Hellingman, O.G. Kruyt, B. Tournesac, "Technical aspects of electron cyclotron current drive on JET", Internal Report 86-018 (1986).

[3] M. Thumm, "High power millimeter-wave mode converters in overmoded circular waveguides using periodic wall perturbations", Int. J. Electron. (1984) 57 no. 6, p. 1225-1246.

[4] L. Rebuffi, "Detailed frequency measurements on gyrotrons using a gyro radiometer". To be published.

[5] W. Kasparek, G.A. Mueller, "A novel device for multimode analysis in oversized waveguides". Conf. Digest 10th Conf. Infrared and Millimeter Waves, Lake Buena Vista (1985) p. 238.

[6] P.G. Schueller, et al., "Matched loads for high-power gyrotron tests". Conf. Digest 10th Conf Infrared and Millimeter Waves, Lake Buena Vista (1985) p. 160.

[7] J.L. Doane, "Overmoded waveguide components for the ECH system on PDX", PPPL 2071, 1984.

[8] J.L. Doane, " Mode converters for generating the HE_{11} (Gaussian-like) mode from TE_{01} in a circular waveguide", Int. J. Electron. (1982) 53 no. 6, p. 573-585.

[9] S. Silver, "Microwave Antenna Theory and Design", MIT Rad. Lab. Series, 12 (1948).

[10] C.A.J. van der Geer, "Theory and design of TE_{01} - TE_{11} mode converter", Rijnhuizen Report 85-163 (1985).

[11] J.L. Doane, "Polarization converters in overmoded circular waveguide for electron cyclotron heating at 60 GHz", Conf. Digest 10th Conf. Infrared and Millimeter Waves, Lake Buena Vista (1985) p. 166.

[12] Lau Jen Chu, "Electromagnetic waves in elliptic hollow pipes of metal", J. Appl. Phys. **9** (1938) p. 583-591.

[13] S.N. Vlasov and I.M. Orlova, "Quasi-optical transformer which transforms the waves in a waveguide having a circular cross-section into a highly directional wave beam", Radiophys. & Quantum Electron. **17** (1974) p. 115-119.

[14] P.J.B. Clarricoats, A.D. Olver, S.L. Chong, Proc. IEEE **122** (1975) 1173.

V Optical Transmission Line for an ECRH Experiment on JET, I.R. 86/020.

FOM-Instituut voor
Plasmafysica
Rijnhuizen
Nieuwegein

I.R. 86/020
October 1986

OPTICAL TRANSMISSION LINE FOR AN ECRH EXPERIMENT ON JET

J.P. Crenn

Centre d'Études Nucléaires, Association Euratom-CEA
Fontenay-aux-Roses, France

I INTRODUCTION

Preliminary work on optical transmission lines for an ECRH experiment on the JET tokamak is presented. The aim is to investigate the possibility of using an optical device instead of the classical oversized waveguide devices, for transmission of the microwave power over long distances, i.e. some tenths of meters. The supposed advantages of an optical line as compared to a waveguide device, would be to give lower losses and to permit direct launching of a low-diverging, linearly polarized beam in the tokamak. Some papers have been published, dealing with the problem of an optical transmission line in the microwave range [1]-[4]. Here, we use mainly the calculations and results given by Degenford et al. in Ref. [3] as our basic material. The optical line is composed of a series of mirrors shown schematically in Fig. 2. In such a line, the most suitable beam is a quasi-Gaussian beam which is the lowest order mode in the line. The main advantage of a Gaussian beam is its low divergence. Moreover, its field is well linearly polarized and is circularly symmetric. The Gaussian beam is launched from a circular oversized waveguide where a HE_{11} mode is propagating. Thus, a mode converter is needed at the gyrotron exit, to convert the output mode of the gyrotron into the HE_{11} mode.

In this paper, the size of the line, the number of mirrors, the shape of these mirrors and the transmission losses are determined for some configurations. The considered microwave frequency in the calculations is 70 GHz (λ = 4.29 mm).

II GAUSSIAN BEAM RELATIONS

At any point the intensity of a Gaussian beam is given by:

$$I(\rho,\zeta) = I_o(0,\zeta) \exp\left(-\frac{\rho^2}{r^2}\right) , \qquad (1)$$

where ζ is the abscissa along the propagation axis, ρ the radial coordinate, and r is the beam radius at the $\frac{1}{e}$ point of the intensity profile (Fig. 1). The radius w of the field amplitude profile, often considered by physicists dealing with Gaussian beams, is related to r by

$$w = r\sqrt{2} , \qquad (2)$$

which means that w is the radius at the $\frac{1}{e}$ point of the field amplitude profile.

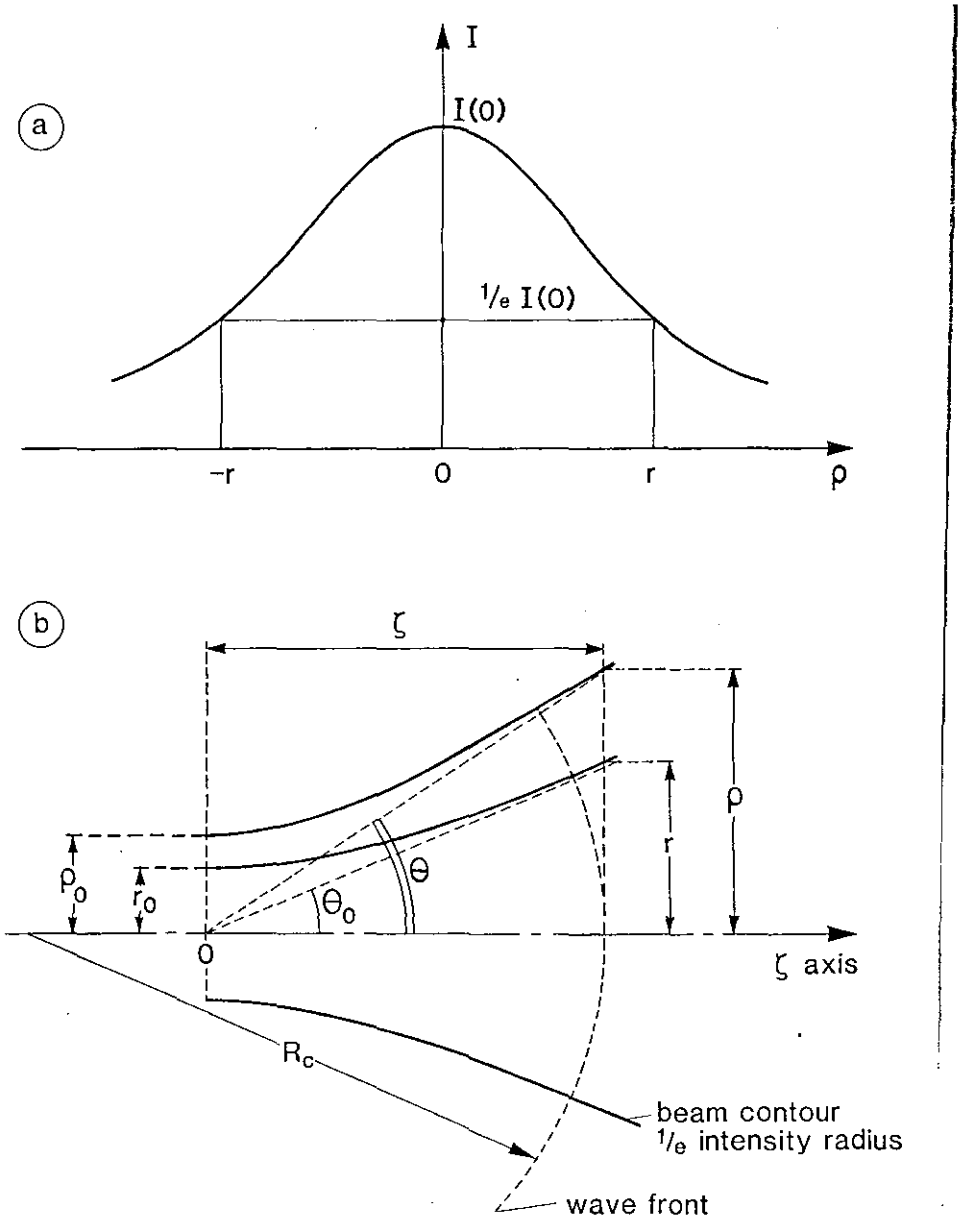

Fig. 1. Main parameters of a Gaussian beam.

Two basic relations, yielding the radius r and the angle of divergence Θ_o of the Gaussian beam are of interest:

$$r^2(\zeta) = r_o^2 \left[1 + \left(\frac{\zeta}{kr_o^2} \right)^2 \right] \tag{3}$$

$$\operatorname{tg} \Theta_o = \frac{r}{\zeta} = \frac{1}{kr_o} , \tag{4}$$

where $k = \frac{2\pi}{\lambda}$.

The beam contracts to a minimum radius r_o at the beam waist.

In order to launch a quasi-Gaussian beam into the optical line, a HE_{11} mode in an oversized circular guide is needed (Fig. 2). The HE_{11} far-field beam is well-fitted by a Gaussian beam with a waist radius at the guide exit given by [5]:

$$r_o = \frac{R}{u_{11}} \qquad \left(\text{or } w_o = \frac{R\sqrt{2}}{u_{11}} \right) , \tag{5}$$

where R is the guide radius and $u_{11} = 2.405$ is the first root of the Bessel functions $J_o(x)$.

Recent calculations [6] show, that the HE_{11} far-field pattern is better fitted by the Gaussian beam determined by Eq. (5) than by the Gaussian beam calculated by Abrams [7] which corresponds to the waist radius

$$r_o = 0.4550\ R \qquad (\text{or } w_o = 0.6435\ R) . \tag{6}$$

The value given by Eq. (6), often used by physicists, yield a somewhat wrong far-field pattern. Thus, Eq. (5) will be used here.

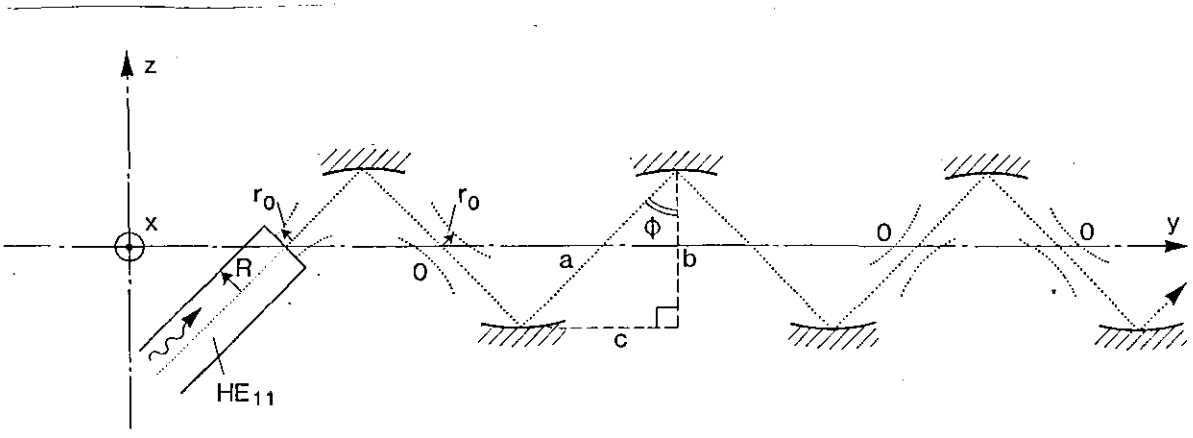

Fig. 2. Optical transmission line: main geometrical parameters.

III OPTICAL LINE DESCRIPTION

The main parameters of the optical line are defined in Fig. 2. From the paper by Degenford et al. [3], the mirrors have an elliptic paraboloïd shape described by the relation (Figs. 2 and 3)

$$z = \frac{x^2}{2b} + \frac{by^2}{2a^2} \tag{7}$$

The lengths a and b are indicated in Fig. 2. The width and the length of the mirror are:

$$\text{width} = 2s, \quad \text{length} = 2s\,\frac{a}{b}. \tag{8}$$

In this case, the lowest-order mode of the line is a quasi-Gaussian beam, where the waist is located at each point-O on the axis between two mirrors (Fig. 2). The waist radius is given by:

$$r_o = \sqrt{\frac{a}{2k}} \qquad (\text{or } w_o = \sqrt{\frac{a}{k}}) \ . \tag{9}$$

From Eq. (4), the angle of divergence is:

$$\operatorname{tg} \Theta_o = \sqrt{\frac{\lambda}{\pi a}} \ . \tag{10}$$

From Eqs. (5) and (9) the radius R of the wavequide launching the beam (Fig. 2) is derived as:

$$R = u_{11}\sqrt{\frac{a}{2k}} \ . \tag{11}$$

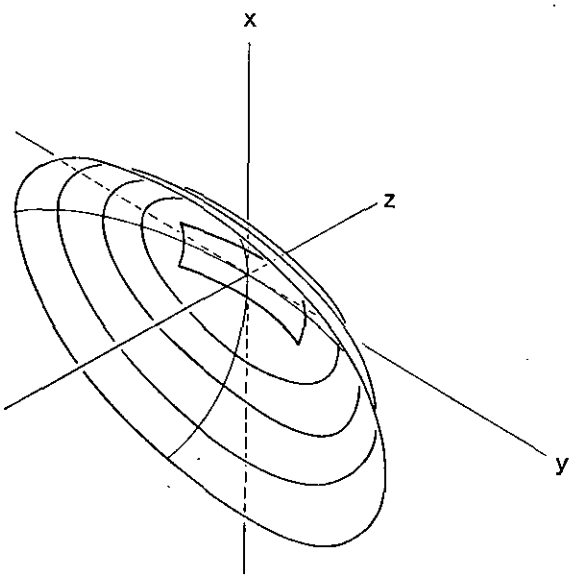

Fig. 3. Three-dimensional view of a mirror and the elliptic paraboloid of which it is a part (from [3]).

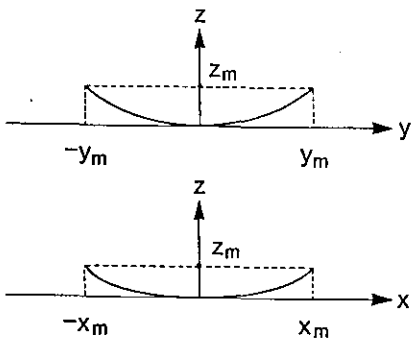

Fig. 4. Dimensions.

Two loss processes are taken into account:

- Diffraction losses P_D due to the finite size of the mirrors. These losses are plotted in Fig. 5 which is taken and adapted from Ref. [3].
- Ohmic losses P_Ω on the mirror. These losses are given by [3]:

$$P_\Omega \equiv 4 \frac{b}{a} \sqrt{\frac{\pi \varepsilon_o f}{\sigma}} \quad . \tag{12}$$

for an electric field perpendicular to the yz plane (Fig. 2), and by

$$P_\Omega = 4 \frac{a}{b} \sqrt{\frac{\pi \varepsilon_o f}{\sigma}} \quad , \tag{13}$$

for an electric field in the yz plane (Fig. 2). In Eqs. (12) and (13), f is the frequency, σ the conductivity and ε_o the free-space dielectric constant, $\varepsilon_o = \frac{1}{36\pi 10^9}$ F/m.

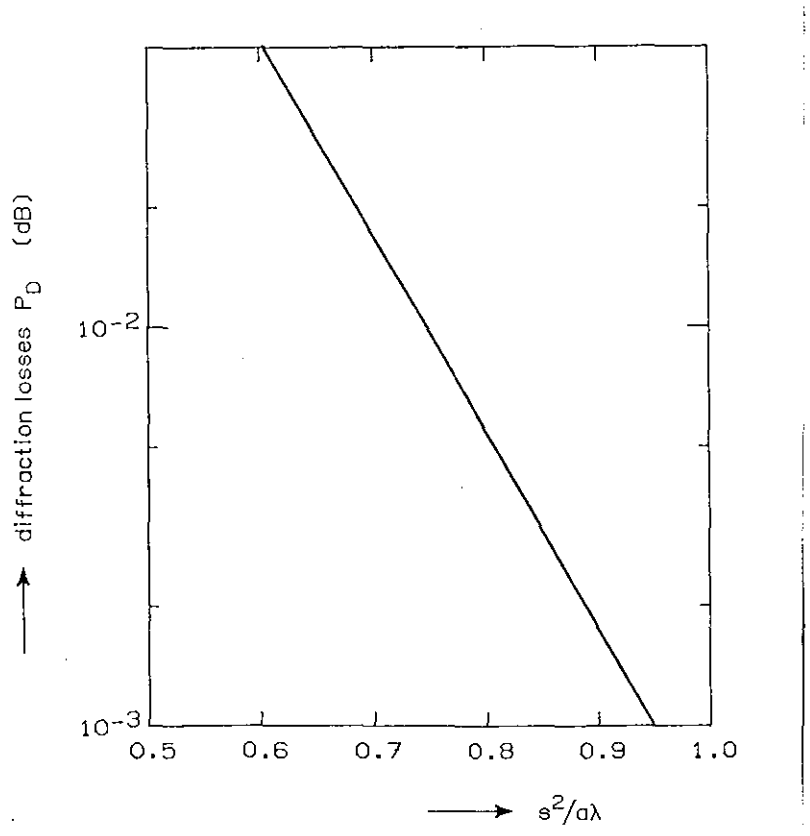

Fig. 5. Diffraction losses per reflection (from [3]).

IV APPLICATIONS

Applications are considered for several cases of transmission lines with lengths up to 50 m at f = 70 GHz (λ = 4.29 mm) which are typical values, applicable to JET.

Case 1 First, we consider a beam with the geometrical parameters (see Fig. 2):

$c = b = 200$ mm $\qquad \phi = 45°$

$a = 200\sqrt{2} = 283$ mm

The electric field vector $\vec{E}$ is perpendicular to the yz plane.
The mirror surface is given by Eq. (7):

$$z = \frac{x^2}{2b} + \frac{y^2}{4b} ,$$

and from Eq. (11) the waveguide radius is

$$R = 23.6 \text{ mm} .$$

From Fig. 5, the limitations of diffraction losses P_D to 10^{-3} dB per reflection, gives:

$$\frac{s^2}{a\lambda} = 0.95 \qquad \text{or} \quad s = 34 \text{ mm} .$$

The mirror size in the y direction (see Fig. 4) follows from Eq. (8):

$$\begin{cases} y_m = 48 \text{ mm} \\ z_m = 2.9 \text{ mm} \end{cases} \qquad x = 0$$

and in the x-direction

$$\begin{cases} x_m = 34 \text{ mm} \\ z_m = 2.9 \text{ mm} . \end{cases} \qquad y = 0$$

The ohmic losses are derived with the following typical value of metal conductivity in the mm-range [8]:

$$\sigma = 2.10^7 \text{ mho/m}.$$

From Eq. (12) we obtain the result

$$P_\Omega = 0.003832 \text{ dB}.$$

Hence, after one reflection on a mirror the total loss is:

$$P_L = P_D + P_\Omega = 0.004832 \text{ dB}.$$

The total power losses P_L as a function of the length of the line is calculated (one reflection for each 200 mm increase of y). The result is plotted in Fig. 6, where P_L is given as a percentage of the total incident power P_T.

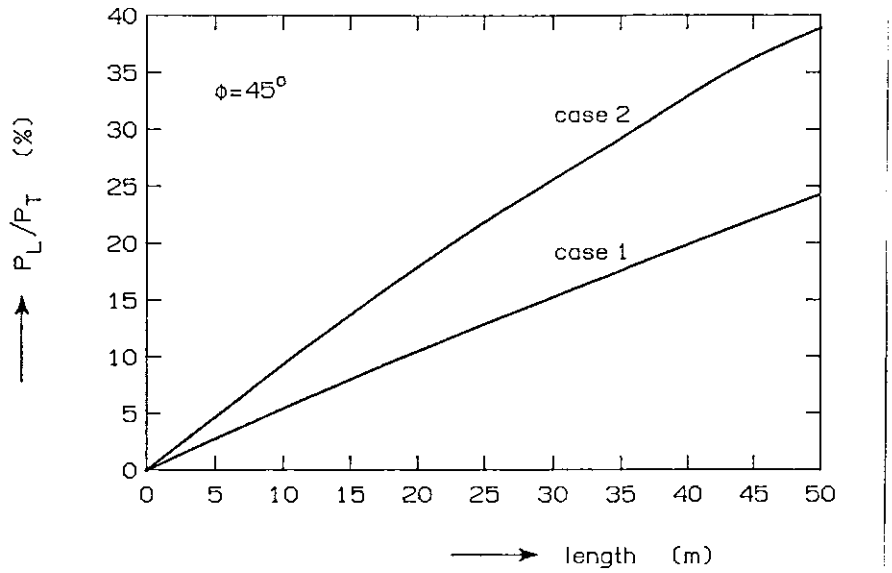

Fig. 6. Fractional power loss in cases 1 and 2.

Case 2 The line configuration is the same as in case 1, with the same geometrical parameters. The only difference with case 1 is that the electric field vector $\vec{E}$ is in the yz plane.

Ohmic losses are derived in the present case from Eq. (13):

$$P_\Omega = 0.007667 \text{ dB.}$$

The total loss after one reflection on a mirror is:

$$P_L = P_D + P_\Omega = 0.008667 \text{ dB.}$$

The total power loss P_L is plotted versus the length of the line in Fig. 6.

Case 3 In order to decrease the number of reflections and mirrors, and the losses, we consider a case with a larger value of ϕ than in cases 1 and 2:

$b = 200$ mm $\qquad \phi = 60°$

$c = b \text{ tg } 60° = 346$ mm

$$a = \frac{b}{\cos 60°} = 400 \text{ mm.}$$

The electric field vector is perpendicular to the yz plane. The mirror surface is derived from Eq. (7):

$$z = \frac{x^2}{2b} + \frac{y^2}{8b} ,$$

and from Eq. (11) the waveguide radius is:

$$R = 28.1 \text{ mm}.$$

Limiting the diffraction losses to 10^{-3} dB per reflection (see Fig. 5) we obtain

$$\frac{s^2}{a\lambda} = 0.95 \quad \text{i.e.} \quad s = 40.4 \text{ mm}.$$

The mirror size in the y direction is:

$$\begin{cases} y_m = 80.7 \text{ mm} & x = 0 \\ z_m = 4.1 \text{ mm} \end{cases}$$

and in the x-direction

$$\begin{cases} x_m = 40.4 \text{ mm} & y = 0 \\ z_m = 4.1 \text{ mm}. \end{cases}$$

The ohmic losses, with the same parameters as for case 1, are derived from Eq. (12)

$$P_\Omega = 0.002709 \text{ dB},$$

and the total losses after one reflection are:

$$P_L = P_L + P_\Omega = 0.003709 \text{ dB}.$$

The total power losses P_L are plotted versus the length of the line in Fig. 7.

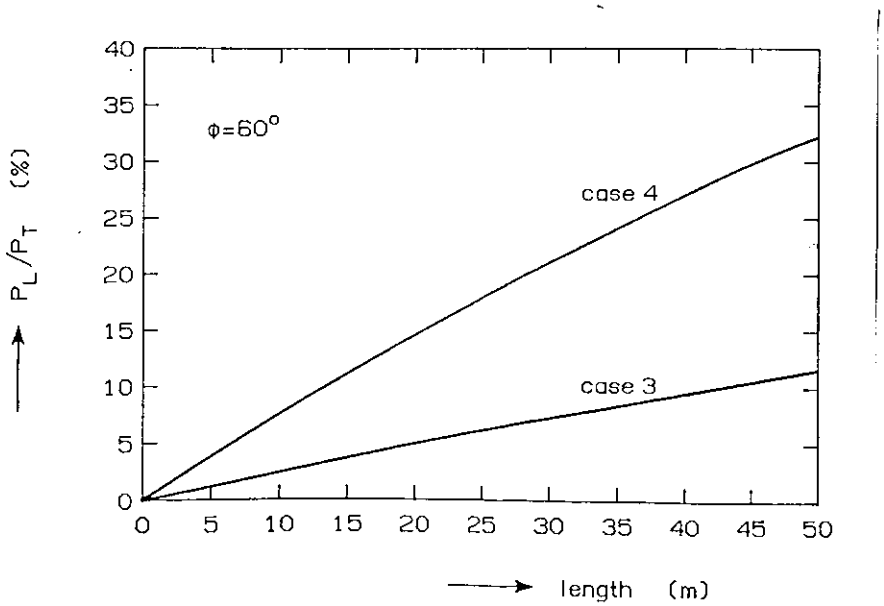

Fig. 7. Fractional power loss in cases 3 and 4.

Case 4 The line configuration is the same as for case 3, with the same geometrical parameters. The only difference with case 3 is that the electric field vector is in the yz plane.

Therefore, using the same parameters as for case 3, the ohmic losses derived from Eq. (13) are:

$$P_{\Omega} = 0.0010847 \text{ dB},$$

and the total losses, after one reflections on a mirror, are:

$$P_L = P_D + P_{\Omega} = 0.011847 \text{ dB}.$$

The total power losses P_L are plotted versus the length of the line in Fig. 7.

From these results, it is obvious that the electric field polarization is an important parameter, especially for increasing values of ϕ and that an electric field vector perpendicular to the yz plane may be needed.

V DISCUSSION AND CONCLUSION

The transmission line described in case 3 gives acceptable losses for lines up to 50 m length and even more. However, for applications to transmission lines for JET, some problems and difficulties are expected to be encountered:

- For instance, the diameter of the line is 200 mm, which is large compared to the usual waveguide diameter of 63.5 mm for ECRH. It would be necessary to reduce this diameter, because of space requirements on JET. A smaller diameter leads to a larger number of mirrors and reflections (increased losses). An alternative is to increase the angle ϕ. However, a large angle ϕ is only possible with an electric field which is well polarized perpendicularly to the plane of incidence on the mirrors. This is not entirely possible to do, due to the shape of the mirrors. Hence, by increasing ϕ, additional losses and depolarization effects are expected, due to the residual electric field component in the plane of incidence. This is shown clearly in Fig. 8, where for angles of incidence close to the Brewster angle region (i.e. for large values of ϕ) there is a large difference between the reflection coefficients for wave components perpendicular and parallel to the mirror. Working in the Brewster angle region should be avoided. An optimization of the value of ϕ has to be made in connection with the JET requirements.

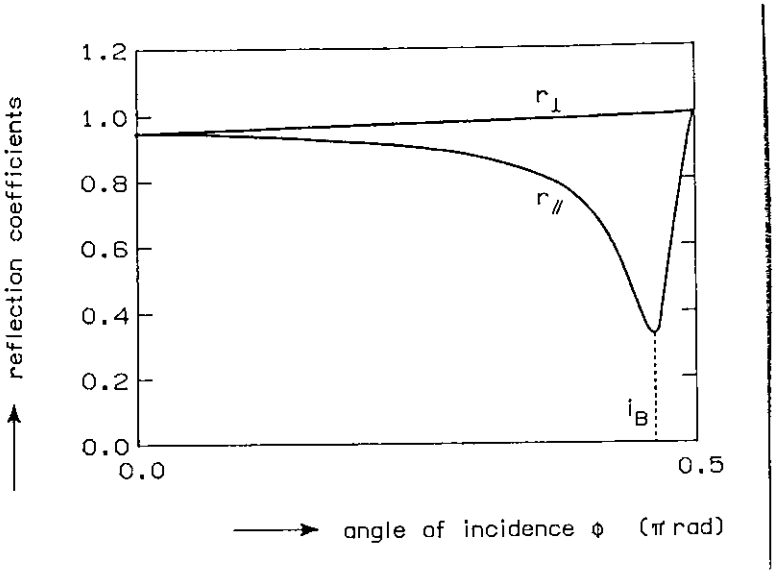

Fig. 8. Variations of the coefficients of reflection $r_{\parallel}$ and $r_{\perp}$ versus the angle of incidence for high conductivity material ($r_{\parallel}$: $\vec{E}$ in the yz plane; $r_{\perp}$: $\vec{E}$ perpendicular to the yz plane). The Brewster angle is i_B with $tg\ i_B \simeq (\sigma/\varepsilon_o\omega)^{1/2}$ for high conductivity material.

- The transmission efficiency may be decreased by spurious modes propagating in the lines as emphasized by Degenford et al. [3].
- Besides the losses, the reflected beam shape is very sensitive to diffraction as shown in Refs. [9]-[11], more sensitive than the diffraction losses considered in this paper. For instance, in Ref. [10] a Gaussian beam through a circular aperture of radius R with $\frac{R}{r_o} > 1.6$ is considered. The corresponding beam losses are:

$$\frac{\Delta P}{P} \simeq \exp\left(-\frac{R^2}{r_o^2}\right) ,$$

and the change in the beam divergence is:

$$\frac{\Delta\theta_o}{\theta_o} \simeq \exp\left(-\frac{R^2}{2r_o^2}\right) = \sqrt{\frac{\Delta P}{P}} .$$

As an example (see Fig. 9):

For $\frac{R}{r_o} = 2.2$ $\quad \frac{\Delta P}{P} = 0.8\ \%$ and $\frac{\Delta\theta_o}{\theta_o} = 8.9\%$

For $\frac{R}{r_o} = 3.1$ $\quad \frac{\Delta P}{P} = 0.01\%$ and $\frac{\Delta\theta_o}{\theta_o} = 0.8\%$.

This means that for diffraction losses below 1%, $R/r_o > 2.2$ is required and for changes in the angle of divergence below 1%, $R/r_o > 3.1$ is needed. Hence, the mirrors must be largely oversized to preserve the Gaussian beam shape.

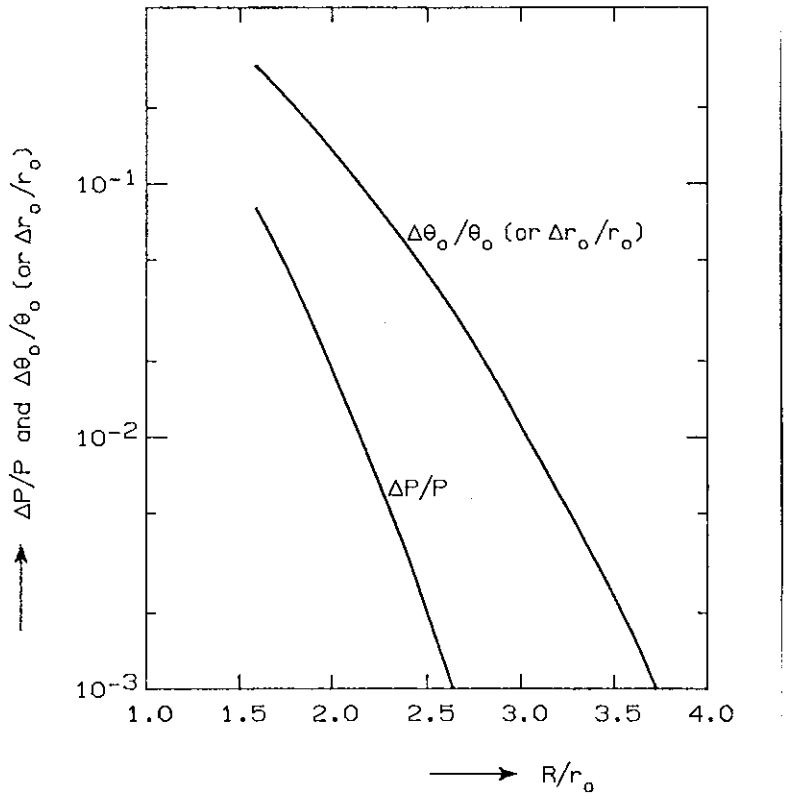

Fig. 9. Changes $\Delta P/p$ and $\Delta\theta_o/\theta_o$ (or $\Delta r_o/r_o$) of a Gaussian beam through a circular aperture of radius R_o located at the beam waist.

- The problem of alignment of the mirrors and the waveguide carrying the HE_{11} mode has also to be considered. The alignment could be done with a HeNe laser, but it is not easy to do. To be less sensitive to misalignment effects, it would be necessary to oversize the mirrors.
- It is possible to make bends in the optical line. In such a case the angle as well as the coefficients in Eq. (7), would be different for each mirror.

As a conclusion, although these preliminary calculations give possible solutions for optical transmission lines on JET, more thorough theoretical investigations are needed in connection with the JET requirements, in particular the space requirements, in order to establish the feasibility of such solutions, to optimize the line parameters, and to make a comparison with a classical waveguide transmission line. In addition, experimental work would be necessary in order to verify the theoretical solutions. Such a programme would need some months of work, in particular for the experimental work, since no experience with such long optical transmission lines exists.

REFERENCES

[1] G. Goubau and F. Schwering "On the guided propagation of electromagnetic wave beams" IRE Trans. on Antennas and Propagation, Vol. AP-9, pp. 248-256, May 1961.

[2] I.R. Christian and G. Goubau "Experimental studies on a beam waveguide for millimeter waves" IRE Trans. on Antennas and Propagation, Vol. AP-9, pp. 256-263, May 1961.

[3] J.E. Degenford, M.D. Sirkis, and W.H. Steier "Reflecting beam waveguide" IEEE Trans. Microwave Theory Tech., MTT-12, pp. 445-453, July 1964.

[4] G. Goubau and P. Coleman "Beam waveguides" in "Microwave Power Engineering" Chap. 3.4. pp. 229-240, Vol.1, Academic Press, 1968.

[5] J.P. Crenn "Optical study of the EH_{11} mode in a hollow circular oversized waveguide and Gaussian approximation of the far-field pattern" Applied Optics, Vol. 23, no. 19, pp. 3428-3433, October 1984.

[6] L. Rebuffi, J.P. Crenn "TE_{11} and HE_{11} mode: a study and comparison of polarization, attenuation and far-field pattern" to be published.

[7] R.L. Abrams "Coupling losses in hollow waveguide laser resonators" IEEE J. Quantum Electron. QE-8, 838 (1972).

[8] N. Marcuwitz, Waveguide Handbook, MIT, Radiation Laboratory Series, Tome 10, Mc. Graw. Hill Book Company, Inc. 1948.

[9] L.D. Dickson "Characteristics of a Propagating Gaussian Beam" Appl. Opt. Vol. 9 no. 8, August 1970, pp. 1854-1861.

[10] P. Belland and J.P. Crenn "Changes in the characteristics of a Gaussian beam weakly diffracted by a circular aperture" Appl. Opt. Vol. 21, no. 3, Febr. 1982. pp. 522-527.

[11] K. Tanaka, N. Saga, and H. Mizokami "Field spread of a diffracted Gaussian beam through a circular aperture" Appl. Opt. Vol. 24, no. 8, April 1985. pp. 1102-1106.

VI Technical Aspects of Electron Cyclotron Current Drive in JET, I.R. 86/018.

FOM-Instituut voor
Plasmafysica
Rijnhuizen
Nieuwegein

I.R. 86/018
October 1986

TECHNICAL ASPECTS OF ELECTRON-CYCLOTRON CURRENT DRIVE ON JET

A.G.A. Verhoeven, P. Hellingman, O.G. Kruyt, B. Tournesac*

Association Euratom-FOM, FOM-Instituut voor Plasmafysica
"Rijnhuizen" Nieuwegein, The Netherlands
*Association Euratom-CEA sur la Fusion, DRFC, CEN,
Boîte Postale No. 6, 92260 Fontenay-aux-Roses, France

SUMMARY

In this paper the layout and preliminary design is described of an installation for the injection of electron-cyclotron wave power into JET. The installation consists of 12 gyrotrons, each 70 GHz, 200 kW RF-output power and a pulse duration of 10 sec. A layout for the installation is given using the vertical ports of octant 3 at the top and the bottom of the vacuum vessel for launching the RF power into the JET plasma. The gyrotrons and most of the other equipment are located in the additional heating hall in the J1H wing. The electric power for the gyrotrons will be supplied by 2 high voltage transformer rectifiers with controlled output voltage. Each of the 2 modulators will use a series tube to regulate the required voltage of 80 kV for 6 gyrotrons. See Fig. 1.

The possibilities to modulate the RF power are discussed. Later on these specifications can be modified according to JET requirements. The entire system will be operated by means of the computerized COntrol and Data Acquisition System (CODAS). The protection system that ensures a safe and reliable operation of the gyrotrons is described. The cooling requirements are listed. The microwave considerations for the predesign of the transmission lines and launching systems are covered in separate reports for both conventional oversized waveguides [1] and optical alternatives [2].

A survey is given of the availability of the required components on the market. For the main components like gyrotrons, cryomagnets, high-voltage power supplies and modulator-regulators, European manufacturers can be regarded as being competitive. The cost of the total ECRH installation with 12 gyrotrons has been estimated to amount to 9 MUC. For design and installation 66 manyears are needed to complete the entire system within 4 years from the start of design.

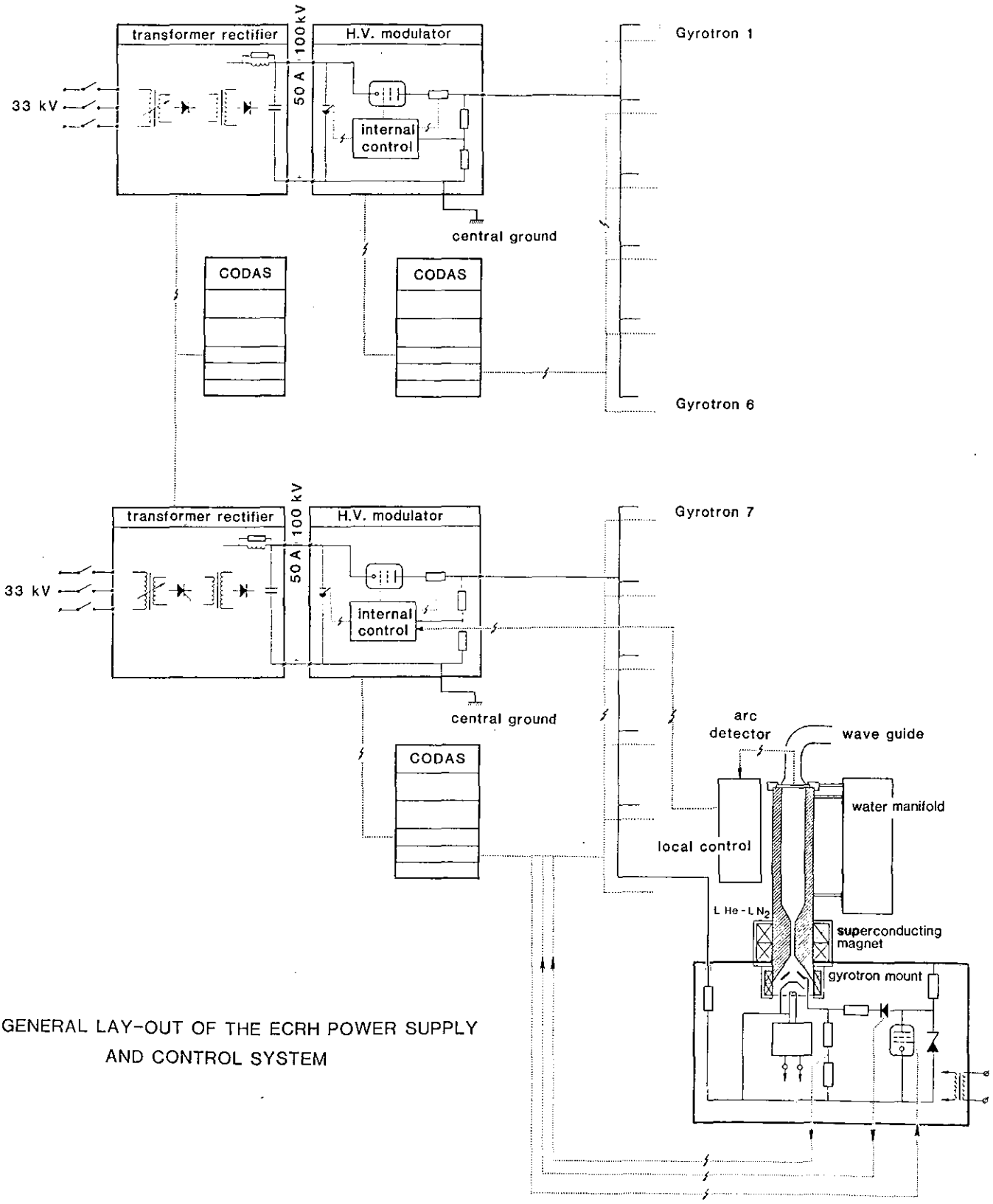

GENERAL LAY-OUT OF THE ECRH POWER SUPPLY AND CONTROL SYSTEM

Fig. 1

INTRODUCTION

Ray-tracing calculations show that a frequency of 70 GHz is most appropriate for current drive and suprathermal generation [3]. Gyrotrons for these frequencies are commercially available, but in unit power levels of only 200 kW. Therefore, the RF power required will be the main parameter for the lay-out of the EC system. The maximum number of gyrotrons with their supply and control systems that can be located in the available part of the J1H wing is 12. Therefore, this paper is written assuming an EC installation of 12 gyrotrons with a total RF power of 2.4 MW, a pulse duration of at least 10 s and a frequency of 70 GHz.

GYROTRONS AND CRYO-MAGNETS

Gyrotrons commercially available within the next few years will have unit powers of about 200 kW. Higher powers per unit, 500 kW or more, will need a longer development time, i.e. 4 to 5 years.

The 70 GHz tubes, cw, with a power of 200 kW will have a cylindrical waveguide cavity, complex or tapered, in a circular (TE_{on}) mode. Quasi-optical tubes with a mirror resonator are only in an early development phase.

At present, the potential suppliers are VARIAN and HUGHES in the USA, THOMSON-CSF and VALVO in Europe. The status of the development programs of the firms involved in gyrotrons is quite different and oriented towards different aims. VARIAN is supplying 70 GHz, 200 kW, cw tubes, in TE_{02} mode, for the stellarator WVIIAS. Also VALVO is developing a 70 GHz, 200 kW, cw tube in the TE_{02} mode for WVIIAS. THOMSON-CSF is developing a tube for 100 GHz ($\pm$ 10 GHz), 200 kW, 100 ms in TE_{04} mode, under EURATOM contract which ends December 31, 1986. When starting this action, EURATOM aimed at a tube for 100 GHz, 200 kW, cw, commercially available in 1988.

Assuming a unit power of about 200 kW and an efficiency of 30 to 40%, the electron beam parameters will be kept in the vicinity of the present tube parameters, i.e., -80 kV, 8 A. However, tuning to maximum power could lead to an RF output power up to 250 kW.

The gyrotrons need a magnetic field with a special profile. This is supplied by a cryo-magnetic device: super-conducting coils inside a cryostat using liquid helium at 4.2 K.

For many years the VARIAN gyrotrons were equiped with super-conducting magnets manufactured by Magnetic Corporation of America. However, MCA gave up this activity about two years ago. Oxford Instruments Inc. (UK) delivered already, in the past few years some super-conducting magnets to Culham Laboratory, and is going to take MCA's place on the market. VARIAN ordered the magnets from Oxford Instruments Inc. for the 140 GHz experimental gyrotron and the 70 GHz tubes for WVIIAS, VALVO bought one 70 GHz magnet and THOMSON-CSF two 100 GHz magnets. In Europe, other potential suppliers of such super-conducting magnets are CEA in France (two 100 GHz magnets for THOMSON-CSF), BBC (one 150 GHz for Karlsruhe) and SMIT, Holland (one 150 GHz for Lausanne).

HIGH-VOLTAGE POWER SUPPLY AND MODULATOR-REGULATOR

Introduction

The high-voltage power supply (HVPS) for an ECRH system is connected to the local 33(36) kV high-voltage grid and has an output voltage of approximately 100 kV. A modulator-regulator is used to stabilize this voltage between narrow limits ($\pm$ 0.5%). The output of the modulator-regulator will be connected to each of the gyrotrons. Special care has to be taken to avoid ground loops.

Modulator-Regulator (MR)

The gyrotrons require a current of 8 A each and a stabilized voltage of -80 kV between collector and cathode. This voltage is stabilized by means of a high-voltage series tube. The tube which is widely used at this moment (also at TFR) is the EIMAC X2062, which is rated for a maximum current of 50 A, a continuous dissipation of 1 MW and a hold-off voltage of 150 kV. This EIMAC tube is used by Universal Voltronics Co. (UVC, Mt Kisco, NY, USA) in a large number of MR's. The BBC tube (as used for the JET PINI MR's) can be regarded as an alternative in case the oscillation problems are solved.

European manufactures are potential suppliers for complete MR systems, e.g. Siemens, BBC and OCEM.

The maximum number of gyrotrons that can be connected to one Eimac series tube is limited to 6. Considering a total number of 12 gyrotrons, at least 2 tubes are required, whatever type of tube is used. Although it is possible to have 2 tubes in parallel in one MR (see GA [4]), 2 separate MR's are preferred. Two MR's make it possible to use one set of gyrotrons for launching RF power to JET and to use the second MR for conditioning or testing the other gyrotrons. In case of pulsing all 12 gyrotrons, a serious problem with one of the gyrotrons during a plasma shot will only lead to switching-off 6 gyrotrons while the other 6 gyrotrons can continue transmitting RF power to the JET plasma.

Each MR will be equipped with a crowbar at the high-voltage input side in order to short-circuit the HVPS in case the series tube does not switch off within the required time [5].
An all solid state MR system that would replace the series regulating tube is not considered to be a serious alternative at present.

High-Voltage Power Supply (HVPS)

Each gyrotron requires a voltage of -80 kV within very narrow limits during the 8 A current pulse. Therefore, each of the systems consisting of one MR and 6 gyrotrons requires a high-voltage power supply (HVPS) of at least -100 kV, 48 A.
This supply has to be stable within narrow limits because all the changes of its output voltage have to be filtered by dissipation in the modulator tube. Using a 1 MW cw series tube for 6 gyrotrons means that the voltage across the series tube has to be limited to 21 kV (1 MW divided by 6 times 8 A).
The voltage drop due to switching on the 6 gyrotrons depends on the short circuit impedance of the 33(36) kV network. For a conventional transformer rectifier this voltage drop is too high to leave a sufficient voltage regulation for coping with the fluctuations of the network itself and for the required 5 kV across the tube for tube stability. Therefore, the HVPS should be a transformer rectifier with a thyristor star point controller system or an equivalent system.

The HVPS system for the EC power can be very similar to the system already in use at JET for Neutral Beam Injection, the PINI HVPS. However, the polarity of the HVPS for EC (negative) is opposite to the

polarity for the PINI (positive). The PINI-HVPS consists of modules of each two units. Each unit can deliver up to +100 kV, 60 A for 20 seconds. For deuterium operation the units within one module, the slave and the master units, can be connected in series, via the protection systems. Then they provide up to +160 kV across the PINI's [6]. The slave HVPS unit is identical to the master HVPS unit except that the insulation level is different: 120 kV for the master unit and 240 kV for the slave unit in order to enable series operation. The negative output of the master unit is connected to ground potential and less insulation is required. Therefore the 2 HVPS for the 12-gyrotron EC system can be designed similar to the PINI master units by reversal of the polarity. Several European manufacturers are capable of coping with the HVPS specifications.

Existing Power Supplies

It is possible to use 2 of the existing PINI-HVPS for EC. In that case the present high-voltage sides of 2 HVPS slave units have to be grounded and the low voltage sides (+100 kV) will then be used as minus 100 kV. If it is not required to use simultaneously the full Neutral Beam Injection (NBI) power and the EC power, sharing of the HVPS can be considered. The major modification to the existing HVPS will be the connection of the output cables to a switch in order to choose between EC and NBI. Approximately 5% of the total EC costs can be saved in case of sharing the HVPS. Due to the reversed polarity the use of the existing MR's seems to be unatractive.

Control of HVPS and MR

During normal operation control of the HVPS and MR will be done via an interface with the JET control and data acquisition system (CODAS). During commissioning and testing the control is switched from CODAS to a local computer through the standard CODAS protocol with a hand-shake exchange of signals.

Site Testing

For commissioning and site testing of the HVPS and the MR a dummy load resistor is required. The dummy load used for the PINI HVPS is still at the JET-site and has the correct specifications. It consists of 10 directly water-cooled resistors (20 kV, 60 A, 20 s, duty cycle of 3%). Series connection up to 200 kV is possible.

To simulate crowbar operation or a gyrotron breakdown, a dummy load crowbar is available. A load variation test can also be executed to test the stability of the series tube control loop.

An existing dc power supply 150 kV/150 mA can be used as a high-voltage source for insulation tests.

POSSIBILITIES TO MODULATE THE RF POWER

Gyrotron Mounts

Each of the gyrotrons will be placed on a tank filled with oil. This tank will comprise the heater supply, measuring and safety circuits and the gun-anode modulator. The gun-anode modulator consists of a zener stabilizer with a pulse tetrode across part of the zener stack. This design enables to switch on the anode voltage within 100 μs. During the last 10 μs of these 100 μs the RF output power rises from 0 to 200 kW.

Power Modulation

The total power level can be chosen in steps of 200 kW. In case an additional power level for each gyrotron is desirable a second pulse tetrode can be added to the anode modulator. With a system of 12 gyrotrons or more there will not be to much need for an additional power step. However, switching from one power level to another with the same gyrotron can be done in a very short time. This enables to switch all gyrotrons simultaneously within 3 μs from a low power level to full power. This 3 μs is far within the sawtooth collapse time of 100 μs. By switching the two tetrodes in the anode voltage modulating system separately it is possible to make a small step in the anode voltage, and therefore in the beam current. In the upper plot of Fig. 2, the anode voltage is given for a gyrotron pulse of 6.5 ms. At the start of the pulse, the anode voltage is switched from 0 to 20 kV. By switching the second tetrode on and off, the anode voltage is stepping between 20 and 21 kV. The middle plot of Fig. 2 shows the result of the variation of the anode voltage: the RF power is modulated between 85 and 170 kW. The lower plot in Fig. 2 shows the beam current. During the first 200 μs, the beam current is charging the parasitic capacitances. In case of modulating the RF power by 50%, the beam current varies only 3%. This leads to a very low load change of the modulator and therefore to a negligible effect on the other gyrotrons.

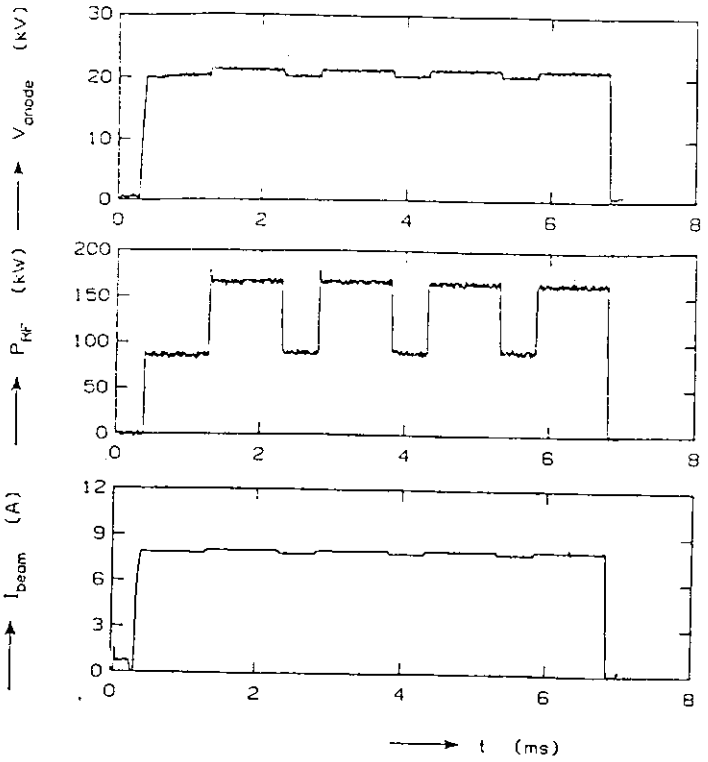

Fig. 2. Fast RF power control by means of anode voltage modulation.

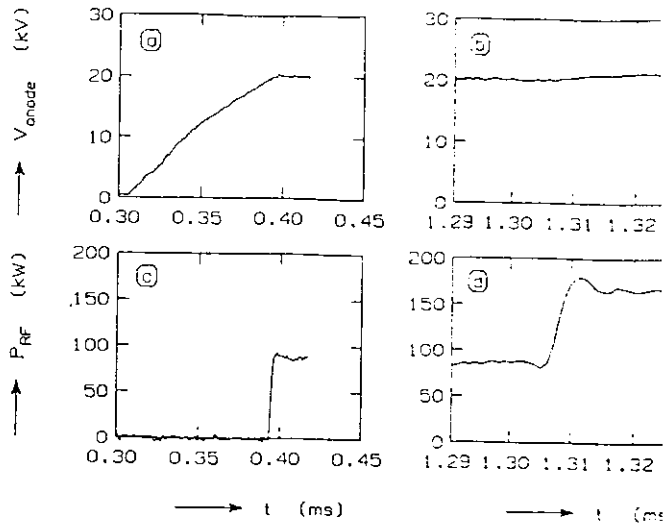

Fig. 3. The effect of increasing anode voltage on the RF power output.

The actual rise time of the anode voltage in case of a step from 0 to 20 kV is 90 μs (see Fig. 3a). The RF-output power has a delay time of almost 90 μs, but the rise time is not more than 3 μs (Fig. 3c). The anode voltage increases from 20 kV to 21 kV in ~5 μs (see Fig. 3b), immediately followed by an increase in RF output in ~3 μs (Fig. 3d). By selecting the step between the anode voltage levels, the RF output can be modulated from 0 to 100%.

To achieve a very high modulating frequency it is possible to switch on the anode voltage again before this voltage has dropped to zero. This enables a modulation of the RF power from 0 to 100% with a frequency up to 100 kHz. Even higher frequencies are possible when modulating less than 100% RF power [7].

The possibilities mentioned before to modulate the power can be used for example to react upon periodic plasma phenomena. This can be achieved by pulsing at 100% RF output in case the plasma activity is in the centre of the resonance area and by pulsing with a reduced gyrotron output at the moment the plasma activity is outside the resonance area. At present we have at TFR a phase-locking unit that can be used for frequencies up to 25 kHz with an accuracy of ~1 μs.

JET requirements will be the basis on which a power modulation system has to be specified.

Feedback Control

A feedback control unit is used for MHD-mode control experiments on TFR [8]. Gyrotrons are switched on by this unit in case of increasing plasma activity. A signal from the plasma is transferred into a signal with a frequency proportional to the degree of disturbance. At the first pulse the first gyrotron will start transmitting RF power into the plasma. When the mode is suppressed, the gyrotron will be switched off. If the mode activity remains higher than a certain threshold, the second gyrotron will be switched on automatically. A very high disturbance will switch on the third gyrotron as well. An anode feedback control is built in that can be used to switch over to another gyrotron in case a gyrotron is switched off because of an interrupting action. See "Protection System". Again JET requirements will be the basis on which a feedback control system has to be specified.

CONTROL AND DATA ACQUISITION

Control

To enable central control of the EC installation and in order to minimize manpower requirements, the control of the gyrotron installation has to be automatized as much as possible. For 12 gyrotrons the number of operators should be limited to 1 or 2. Most probably the gyrotrons will be located in an area where it is uncomfortable or even forbidden for people. This means that the complete gyrotron installation has to be remotely controlled.

At JET the computerized Control and Data Acquisition System (CODAS) is available for remote control. Since CODAS is designed for centralized control and monitoring of all actions to be performed during normal operation, this system should also be employed for the complete control of the EC installation during:

- the commissioning of the EC installation,
- the normal EC pulses on JET,
- the conditioning of the gyrotrons during a number of hours (pulsing with a short pulselength of approximately 1 ms),
- the conditioning of gyrotrons in between JET pulses,
- the tests on RF loads,
- the standby periods.

Changing from one task to another must be possible within a short time. The main parts of CODAS are the central control computer, the subsystem computers, the CODAS cubicles and the connecting network.

The system is controlled by the software packages in the computers.

The central control computer is coupled to the subsystem computer, a NORD 100. In normal situations the central computer is in command. The subsystem computer manipulates the main part of the software dedicated to the EC system and it operates as a stand alone system. In that case the commands are given from an auxiliary console. The subsystem computer is connected by a glassfiber ring line to the CODAS cubicles. EC modules, located close together and forming a logical unit, share a CODAS cubicle. A CODAS cubicle consists of CAMAC crates with data handling units, timers, memory and subracks with signal conditioning units. A general layout of the EC control and data-acquisition system is given in Fig. 4.

The control part of CODAS is functioning as follows:
A computer program, running in the subsystem computer generates a set of control signals, taking into account the commands from the console or auxiliary console and the status of the system. The computer is able to address these signals to the separate output channels in what is called the line surveyor and driver system, LSD. An output signal will be stored by that particular LSD channel until signals from EC modules are given to the LSD input channels. The computer scans these inputs and will take their status into account at the next command. An LSD in one cubicle can be used for interfacing up to 512 digital input and output single bit signals. The LSD system consists of the following elements: CAMAC module type CLS2; system bus; subrack type ULB1; input card type ULS1; output card type ULD1; connector card type ULC1 and power supply unit UPS1.

A ULD1 card passes 16 output bits from the LSD bus to the card's 16 outputs. Each bit can be used as a switch or combined to a 2, 4 or 8 bit value. Four bits, for example, will be used for the setting of magnet currents, 8 bits for the anode voltages of the gyrotrons. A ULS1 card passes 16 input signals to the LSD bus. The card will be used to indicate the status of the EC system. For example: waterflow on, filament currrent on, etc. The LSD will be connected to relay-based control systems or PLC's for modules like

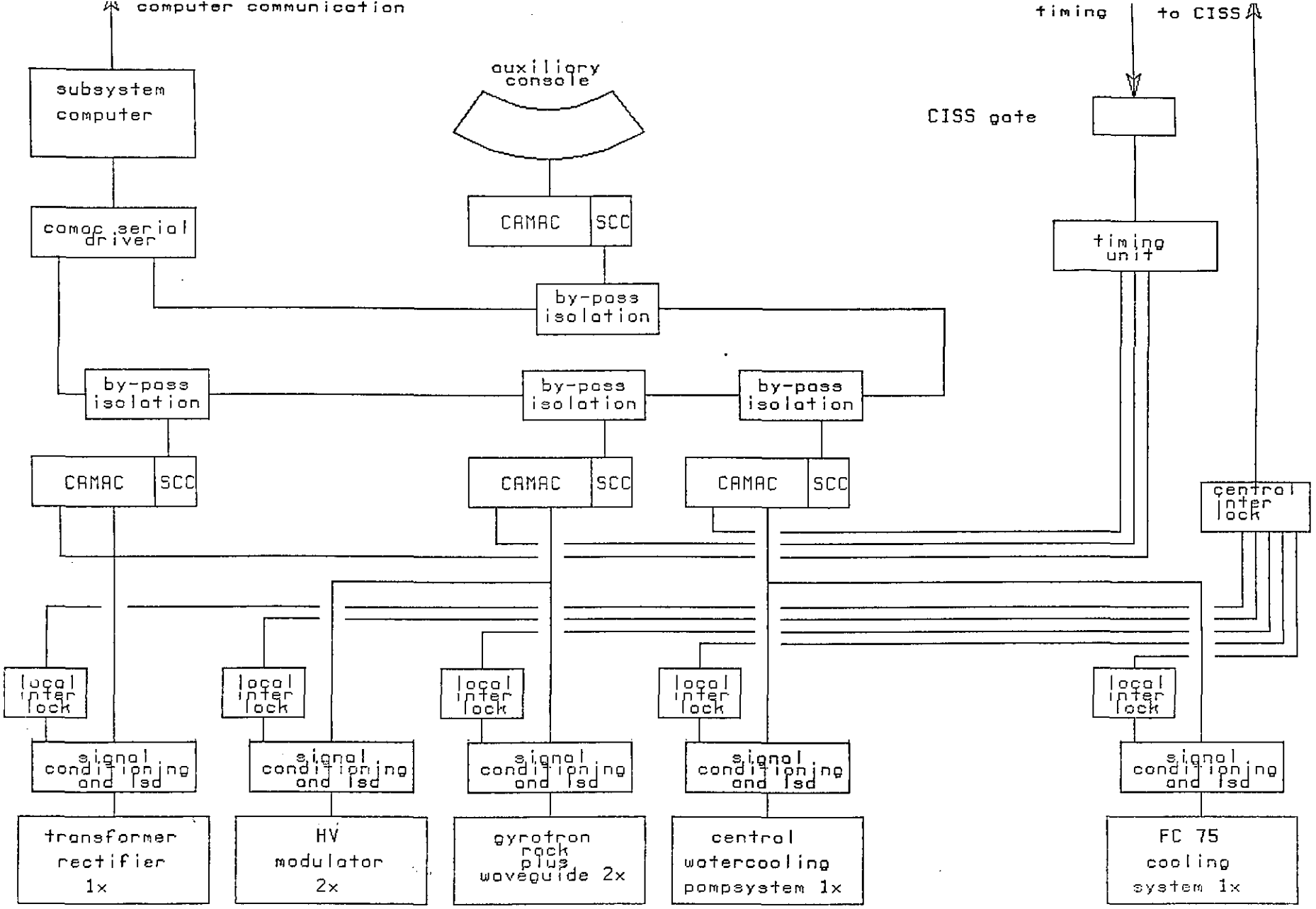

Fig. 4.

general layout of the JET ECRH CODAS system

transformer rectifier, HV modulator, gyrotron, water cooling etc.

Control of the complete gyrotron installation from an "operating unit", requires:

a) Remotely controlled switching on/off for each component of the system, e.g.:
   - HV power supply,
   - modulator,
   - water and FC75 cooling,
   - filament of the gyrotron,
   - magnet currents,
   - power supply for RF-power measurements,
   - crowbar test.

b) Automation of all routine jobs:
   - LHe filling up,
   - LN_2 filling up,
   - all main water valves have to be motor activated,
   - monitoring water quality.

c) Controlling of RF-power output and optimal mode purity, therefore:
   - setting of filament supply to adjust the beam current between 6 and 8 A in order to select the RF-power range,
   - setting of cryomagnet current 1 for the required RF-power output of the gyrotron,
   - setting of cryomagnet currents 2 and 5 to tune to optimal mode purity,
   - setting of anode voltage for control of RF-output power level, (2 voltage settings if two power levels per gyrotron are preferred),
   - setting of high-voltage output of HVPS and MR.

d) Monitoring the status of the entire system:
   - the units that are ready, not ready or bypassed,
   - in case it is not ready: an indication of the cause.

Data acquisition

Most of the EC data will be generated by the 24 crystal detectors in the bi-directional couplers of the 12 waveguides. They measure the forward and reflected RF power. The outputs are transmitted through glassfibers to the CODAS cubicles. The signals are divided over 2 cubicles. Each cubicle serves 6 waveguides. One 16 channel analog-to-digital converter (ADC) is measuring the 6 forward

and 6 reflected powers of 6 waveguides at a rate of approximately 1 ms. The start of the measurements are triggered by the JET timing system. Another ADC can be triggered independently, for instance after a breakdown in a waveguide. This ADC will measure at a faster rate: approximately 100 microseconds. Each ADC has its own memory that can be read by the computer after a JET pulse. See Fig. 5.

Signals like the pressure in the gyrotrons and currents in the cryomagnets are scanned with a sample frequency up to a few Hz. They will be transferred continuously to the computer and is displayed on the monitors. Triplevels can be built in and adjusted by using the terminal. The information is not only recorded but will also be used by the control system and invoke actions if necessary.

Requirements for the data acquisition of the complete gyrotron installation are:

a) Continuous monitoring of the important parameters:
   - h.v. power-supply output voltage,
   - vacuum pressure of the gyrotrons (vac-ion current),
   - gyrotron-filament voltage and current,
   - waterflow and temperature difference (when using an RF-water-load).

b) A display of the important pulse parameters after each shot:
   - beam current of each gyrotron,
   - RF-output power as a function of time and its calculated mean value,
   - reflected power as a function of time and its calculated mean value,
   - modulator-regulator output voltage.

c) A display of the triplevels and protection values:
   - maximum number of arcs,
   - level of reflected power,
   - maximum of idling time (the time during which the gyrotron carries a beamcurrent but no RF-output power is generated),
   - duty cycle,
   - level of : beam overcurrent,
     : modulator input overvoltage,
     : modulator output overvoltage,
     : cryomagnet overcurrents (4×),
     : LHe and LN_2,
   - modulator maximum on-time.

CODAS cubicle for HV modulator and 6 gyrotrons

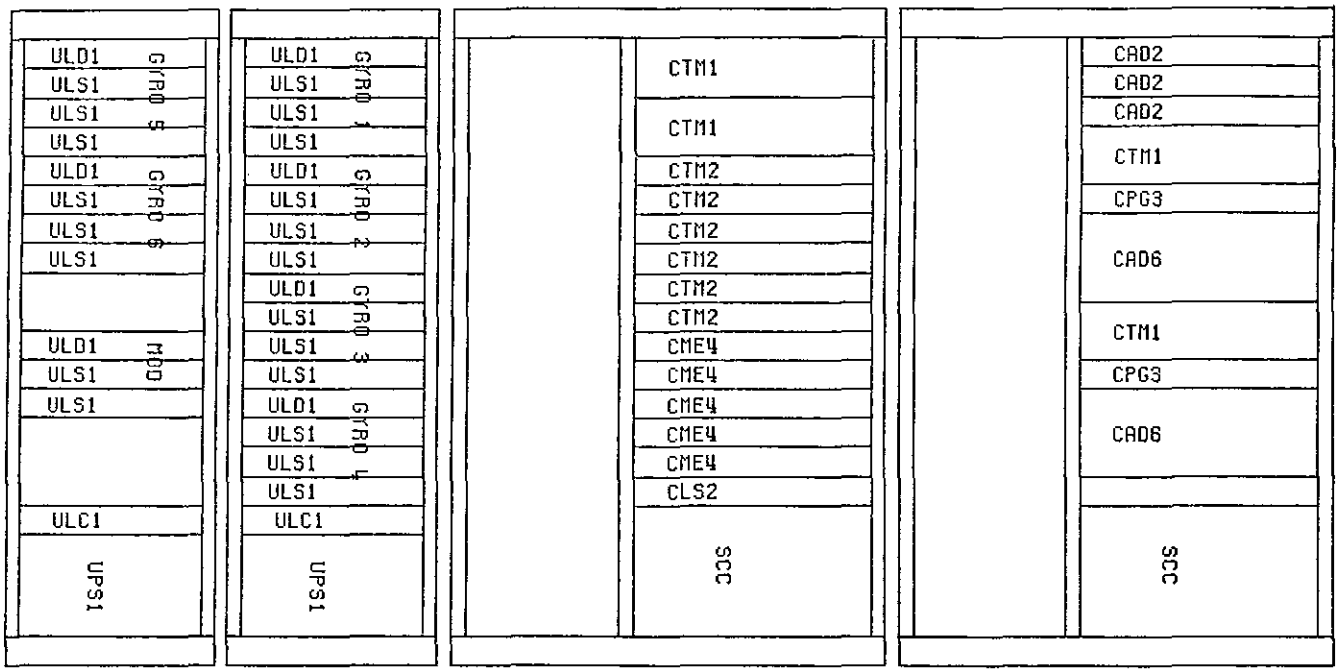

CAD2	CAMAC 32-channel ADC
CAD6	CAMAC 32-channel scanning ADC
CME4	CAMAC memory module
CLS2	CAMAC Line Surveyor and Driver module
CPG3	CAMAC Time Sequence Generator
CTM1	CAMAC Timer System 4-channel module
CTM2	CAMAC Stop-watch
SCC	Serial Crate Controller
ULC1	LSD connector card
ULD1	LSD output card
ULS1	LSD input card
UPS1	power supply unit

Fig. 5.

PROTECTION SYSTEM

A wide variety of control units and protective devices has to be installed to assure a safe and reliable operation of the gyrotrons. The protection system will have several protection levels. In case the output power of a gyrotron is causing problems, the RF output will be suppressed. At the moment a gyrotron is not working properly, it will be switched off. If the fault is not limited to a gyrotron, switching of the gyrotron is not enough and the modulator supplying this gyrotron has to be interrupted. Short circuiting the HV-power supply is the next protection measure. CODAS will monitor the status of main parts of the installation [7].

RF-Output Suppression

At least 4 arc-detectors will be placed in each transmission line. These arc detectors will look at different angles through the transmission line. The arc detectors will be coupled to an Arc-detector Interrupt Module (AIM). Other input signals for this module will be the reflected RF-power signals from the bidirectional couplers. As soon as an arc or reflected power is detected, the gyrotron output will be suppressed. After a short clearing time, the gyrotron will be switched on again. In case of a new fault, the gyrotron will be switched off once more.

Gyrotron Switch-Off

A gyrotron is switched off for the remaining time of the pulse in the following cases:

- the number of faults reported to the AIM is higher than a preset value,
- the idling time is too long.

Modulator Switch-Off

The series tube of the MR will switch off all 6 gyrotrons in the cases:

- a gyrotron does not switch off when required,
- the maximum duty factor is reached,
- beam overcurrent,
- anode overvoltage,
- anode or body overcurrent,
- overdissipation in the series tube (1 MW, cw),
- insufficient cooling.

HV-Power Supply Short-Circuiting

The crowbar located at the input of each modulator will short-circuit the high-voltage power supply under the following circumstances:

- the modulator interrupt does not switch off the modulator fast enough,
- modulator output overvoltage (~ 90 kV),
- modulator-regulator fault,
- modulator input overvoltage (~ 130 kV).

Preventing of Pulsing

A slow system based on relays will prevent firing of the next pulse when the interlock chain is broken. Parallel to this, CODAS will check the status of the security systems and control units, and will compare several voltages with preset values.
In case of a fault the timing system will stop the supply of start pulses. The fault will be displayed to the operator on a monitor. The protection system for each unit of 6 gyrotrons will be completely independent.

The JET central interlock and safety system (CISS) is a hard wired back up for the CODAS system. Since the protection system for the EC installation is completely independent from JET, it is not necessary to have a coupling to CISS. However, in case the start of a discharge has to be prevented or a started discharge has to be interrupted due to problems with the EC system, a link between the local protection system and CISS is easily installed.
A CISS gate will be incorporated in the timing system to prevent the start of an EC pulse or to stop a started EC pulse in case of a problem with JET itself or one of the auxiliary systems.

COOLING

Cooling of the EC installation consists of the following items:

- water cooling of the gyrotrons, modulator-regulators and dummy loads for RF testing and high voltage testing,
- FC-75 cooling of the gyrotron double disc windows,
- cryo cooling of the superconducting magnets,
- cooling of components of the transmission line [1],
- cooling of the window at the end of the transmission line [1].

Water Cooling

The exact requirements for the cooling water supply are difficult to describe since these depend very much on the manufacturer of the gyrotrons. The following figures are related to VARIAN gyrotrons, because VARIAN gyrotrons have the highest water demand.

Each gyrotron needs the following cooling water supply:

at 18 Bar: 570 ltr/min and

at 8 Bar: 60 ltr/min.

Each MR requires 600 ltr/min at 8 Bar.This water has to be of a very high quality: a resistivity of at least 1 MΩcm, deionized, deoxidized and free of dirt and bigger particles.

A system consisting of 12 gyrotrons, 2 modulator-regulators and 1 RF dummy load requires the following cooling water flows:

at 18 Bar: 7000 ltr/min and

at 8 Bar: 2500 ltr/min.

During an RF pulse with 12 gyrotrons, about 7 MW has to be removed while the maximum water inlet temperature has to be kept below 40° C.

If the above mentioned supply is not availble on site, a pumping plant has to be installed (consuming 300-400 KW electric power). A typical plant for this purpose would consist of:

- a central reservoir used as a surge tank, (e.g., 10 m^3 for 30 sec pulses) with a heat-exchange loop, a deionization and deoxidation loop, removal of particles, etc.
- a pump unit for the 18 Bar flows,
- a pump unit for the 8 Bar flows,
- a control system.

This plant (area 100 - 150 m^2) should be situated at a short distance from the gyrotrons. Pipe diameters of the coupling between the cooling water source and the gyrotrons have to be 150 mm (8 Bar), 250 mm (18 Bar), and 300 mm (common return flow). A primary cooling circuit cools the reservoir between the pulses. A primary flow of about 250 ltr/min (25°C) is sufficient for a duty factor of 1%.

FC-75 Cooling

The double disc RF-output windows for the gyrotrons need to be cooled by the fluoro-carbon FC-75 between the ceramic discs. This fluid which has a low microwave loss and a low viscosity provides the cooling path for the heat deposited in the ceramic by microwave losses. The

ceramic discs, most likely made of alumina, are very weak, therefore the pressure has to be carefully controlled to avoid damage to the window.

A closed circuit will be used to supply 30 ltr/min to each of the gyrotrons at a maximum pressure of 4.5 Bar and an outlet temperature not exceeding 20° C. [9]. Refrigeration capacity of the FC-75 liquid depends on the window absorption (± 2%) and the duty cycle. Since FC-75 is very toxic at high temperatures an adequate leak protection system has to be installed.

Cryo Cooling

The magnetic fields for the gyrotrons are generated by superconducting magnets inside cryostats (4.2 K liquid Helium) mounted on top of the gyrotron mounts. The average Liquid Helium (LHe) consumption per gyrotron is about 25 ltr per day. Twenty ltr of LN_2 per day is used for cooling the internal shield of the cryostat. In addition to this, LN_2 is used for pre-cooling the cryostats when the LHe supply has been shut off for a long period (± 70 ltr LN_2).

With an installation of 12 cryostats the use of an automatic filling system is a necessity. This could be fed by the already existing JET cryoplant, using the flexible transfer lines similar to those in use at JET. The distance between the cryoplant and the EC installation is approximately 80 m. A manifold system, similar to the system presently in use at the neutral beam installation could be very well applicable.

The cryostats to be ordered must have the facility to be operated in a closed loop system with the (flexible) transfer lines. The LN_2 supply will give no problems with the application of the standard technology.

LAYOUT

We intend to use the J1H wing for the gyrotrons and the modulators. The gyrotrons will be placed on the floor. In this way, the waveguides can be as short as possible. The waveguides will go through a large penetration to the basement of the torus hall and then up through a small penetration in the floor of this hall. An average cross-section of ½ square meter is needed for the 12 parallel waveguides. A straight line through the 3 m thick concrete wall of the torus hall would be shorter with less bends, but in first instance JET did not like this solution. Further discussion has to make clear whether this is really impossible.

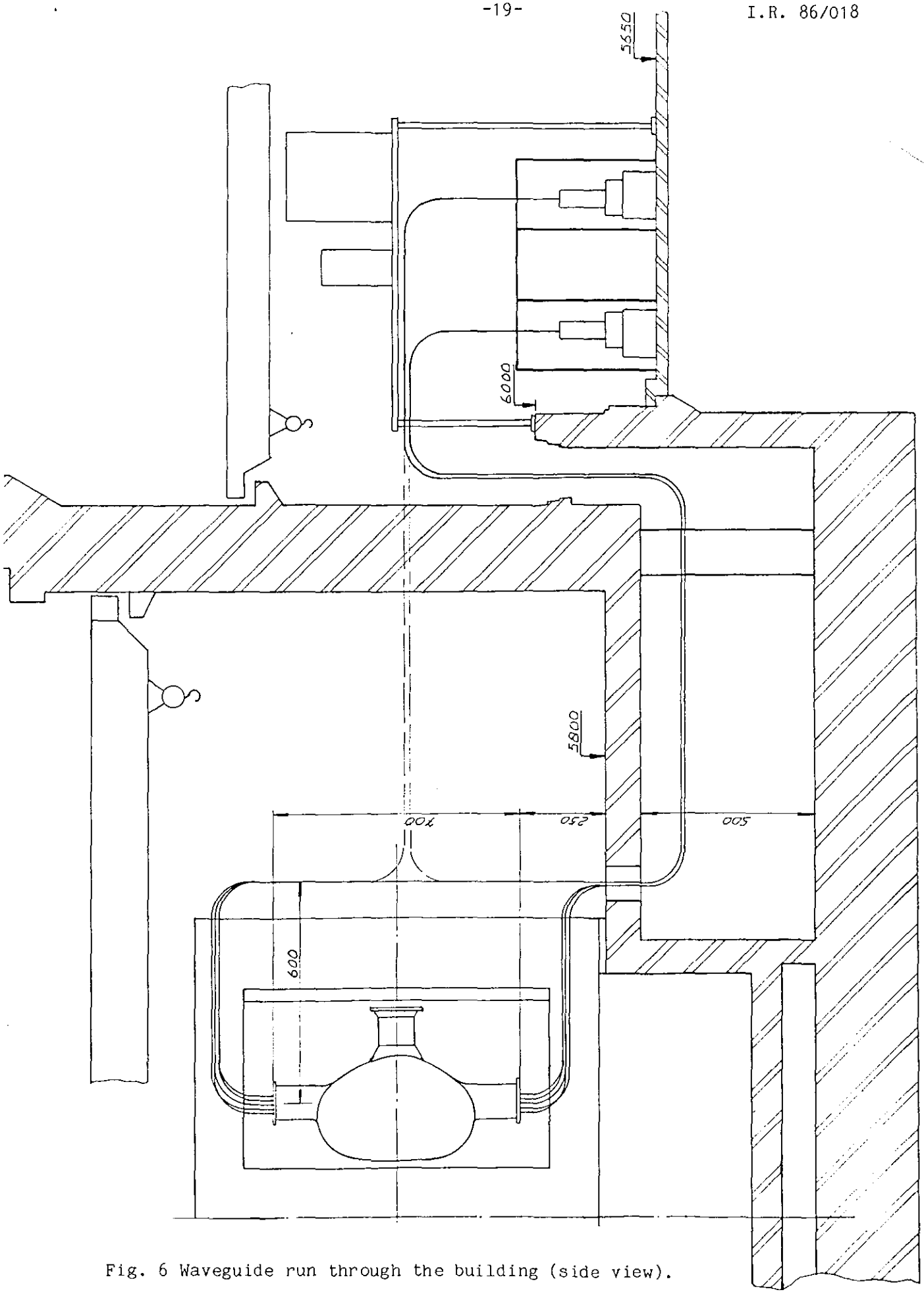

Fig. 6 Waveguide run through the building (side view).

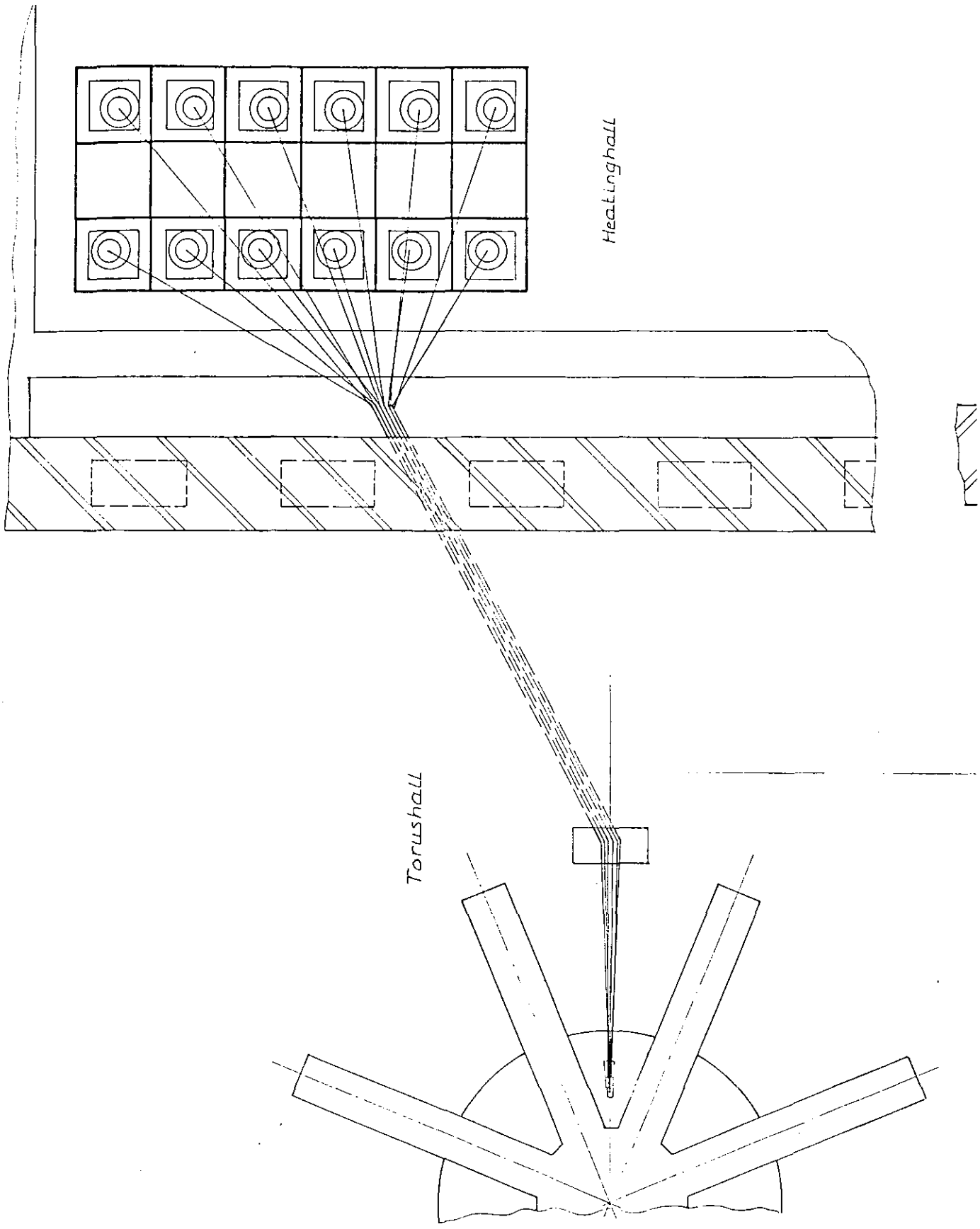

Fig. 7. Gyrotrons, waveguide run and torus hall (top view).

The system proposed in Figs. 6 and 7 will have only "standard" 90 degrees bends and will be flexible enough in its shape to adjust to the different locations of the gyrotrons and the JET ports. The gyrotrons and the modulators must be close together in order to enable fast rise and turn-off times. Therefore the modulators will be placed above the gyrotrons in shielded rooms.

A support structure surrounds the gyrotron mounts, cryomagnets, gyrotrons and the local electronics. It consists of 12 identical units. The ground area of one unit is 2 by 2 meter. The units will be placed in two rows of 6. Between the 2 rows of gyrotrons a space of 2 meter is reserved for the supply pipes for cooling water, LHe and LN_2 and FC-75 and for H.V. cable trunks. The use of dewars will be avoided. The structure must take the mechanical stresses of the waveguides from the gyrotrons, because gyrotrons are rather fragile.

X-ray shielding and RF protection will not surround the gyrotrons in case personnel access during an EC pulse is prohibited. The support structure will be assembled at the JET site. It will have working platforms for easy access to the main parts of the installation. In each unit a built-in little crane will be used to lift the gyrotron into and out of the magnet. The High-Voltage Power Supplies will be placed outside the J1H building. A pumping plant has to be installed if the necessary amount of cooling water is not available on the site. The primary water can probably be provided by the site cooling system in the J1H building. The pumping plant should be located close to the gyrotrons, because of the huge amount of water circulating in the secondary loop.

The subsystem computer will be in the JET computer area. During normal operation the console in the control room will be used. An auxiliary console, located in J1H, will be used mainly during commissioning.

Acknowledgement

This work was performed under JET Article 14, Contract no. JJ5/9007 and under the Euratom-FOM Association with financial support from ZWO and Euratom.

REFERENCES

[1] C.A.J. van der Geer, P. Manintveld, L. Rebuffi, T.J. Schep, "Antenna Structure and Transmission Line System for EC Power Injection into JET", I.R. 86/019, part of this study contract.

[2] J.P. Crenn, "Optical Transmission for an ECRH Experiment on the JET Tokamak", I.R. 86/020, part of this study contract.

[3] R.W. Polman, T.J. Schep, E. Westerhof, L. Klieb, "Electron Cyclotron Current Drive and Supra-Thermal Generation in JET", I.R. 86/021, part of this study contract.

[4] D.B. Remsen Jr, "Power Systems for the Doublet III 2 MW ECH System", GA-A1560 (1979).

[5] A.M. van Ingen, A.B. Sterk, A.G.A. Verhoeven, B. Tournesac, C. Viniane, "High-Voltage Supply and Control System for Three 60 GHz 200 kW Gyrotrons", Proc. 13th Symp. on Fusion Technology, Varese (1984) Vol. 2, p. 805.

[6] R. Claesen et al., "Commissioning and Early Operation of the Power Supply and Protection System for the Extraction Grid of the JET Neutral Injectors", Proc. 13th Symp. on Fusion Technology, Varese (1984) Vol. 2, p. 829.

[7] A.G.A. Verhoeven et al., "Power Supply and Operating System for Three 60 GHz Gyrotrons at TFR", 11th Symp. on Fusion Engineering, Austin, Texas, 18-22 November 1985.

[8] A.G.A. Verhoeven et al., "Technical Aspects of the Joint FOM/CEA ECH Experiment on TFR", EC-5, 5th Int. Workshop on ECE and ECH, San Diego, CA, 9-12 November 1985.

[9] M.W. Alcock, A.C. Riviere et al., The ECRH System, Gyrotron Supply and Control, Phase II "MW Level ECRH Heating for DITE and COMPASS".

BUDGETARY AND TIME SCHEDULE ESTIMATES

(A.G.A. Verhoeven, A.M. van Ingen)

The Manpower

The technical manpower (professional engineers and technicians) provided by FOM during the project realization of the EC experiment at Fontenay is about 25 man years. Another 13½ man years have been spent by CEA on transmission lines, local installations and support. In total ≈ 38.5 man years were spent.

It is difficult to give some proportionality factor but roughly 3 technician-years are necessary for installation tasks per gyrotron (including transmission line, cooling and power supplies). For a system as installed in Fontenay 20 professional manyears were necessary for testing design studies, coordination and control of production. For a project of 12 gyrotron and possibly different manufacturers for the same system elements (to spread risks) the last figure will have to be multiplied by a factor of 1½. In this way we reach to about 66 manyears for the 12 gyrotrons project, 36 technician manyears and 30 professional engineer manyears.

The Time Schedule

For new types of transmissionline elements (e.g. mirror systems, remotely maintenance parts, other dimensions), high power tests are necessary (thermal effects, sparks etc.) They can only be carried out after gyrotrons are available. In order not to delay the construction time too much it seems necessary to have a prototype gyrotron and prototype transmission-line parts available in an early stage of the project. See Fig. 1. Alternatively, tests could be executed by using existing gyrotrons at one of the laboratories of the EURATOM associates.

TIME SCHEDULE FOR 12 GYROTRONS ON JET

EC on JET (years)	1	2	3	4
	design start ↓	budget approval ↓		
Project specification coordination				
H.V. Supply		1	2	
Modulators		1	2	
Gyrotrons		0 1	6	12
Magnets		0 1	6	12
Mounts-module		1	6	12
Cooling		1	6	12
Transmission lines		0 1	6	12
Control electronics		1	6	12
Site preparation		•		

0 prototype

1, 2, 6, 12 number of sequence

Fig. 1.

Budget Estimate

It is very difficult to estimate the prices of the EC components. For most of the components the extended pulse length will increase the cost. More competition and larger production series will, on the other hand, have a decreasing effect on the prices. Therefore, we assume these components will be priced similar to those in use at FaR.The prices of the gyrotrons are the most important, but they are quite uncertain. In 1984 VARIAN has given a budgetary price of 250 k$ for a long pulse 60 GHz gyrotron. We assume that 70 GHz tubes will cost approximately the same as 60 GHz tubes and that the prices are not higher than in 1984. Superconducting magnets will be at approximately

the same price as in 1983, although a higher frequency means a higher magnetic field.

The total price for a 12-gyrotron installation is estimated at 9 MUC, this means approximately 4 MUC per MW RF power. See Fig. 2. In case more than 12 gyrotrons are required for the final installation, the price per MW will decrease because of larger series and because some of the costs (e.g. design costs) have to be made only once. The price depends very much on the ratio between the US dollar and ECU: at this moment 1 US $ = 1.1 ECU

PRICE of 12 GYROTRONS ON JET

Components	number	estimated price/piece MUC	total price MUC
Gyrotron	12	0.28	3.36
Magnet	12	0.09	1.08
High voltage power supply	2	0.3	0.6
Modulator-Regulator	2	0.36	0.72
Anode modulator	12	0.05	0.6
Local protection, control and data acquisition	12	0.02	0.24
Central control and data acquisition (CODAS)	1	p.m.	
Cooling			0.7
Test equipment			0.15
Transmission line	12	0.13	1.56
			9.01 MUC

Fig. 2.